



## DOCTORAL THESIS

Deposition and characterization of functional cobalt – polymer  
nanocomposites prepared by a hybrid plasma process

Zur Erlangung des akademischen Grades  
Doktor der Ingenieurwissenschaften (Dr.-Ing.)

Submitted by

Karthika Lakshmi Kolipaka

Supervised by

Prof. Dr. Franz Faupel

Multicomponent Materials,  
Technical Faculty of the Christian-Albrechts-University of Kiel

August 2012

1. Gutachter: Prof. Dr. Franz Faupel

2. Gutachter: Prof. Dr. Juergen Roepcke

Datum der mündlichen Prüfung: March 5, 2013

# Abstract

In this study novel type of cobalt – polymer nanocomposites were developed. The goal of this work was to develop new type of functional cobalt oxide – dielectric matrix nanocomposites which are applicable as optoelectrochromic phosphate ion sensors. Cobalt – plasma polymerized hexamethyldisilazane (Co – ppHMDSN) nanocomposites were prepared using a simple method of hybrid physical vapor deposition/plasma enhanced chemical vapor deposition. The nanocomposites consisted of nanoparticles embedded in a polymer matrix. The metal filling factor was varied from 4% to 34%. Structural and compositional investigations were performed using various analytical techniques such as TEM, XRD, XPS, XAS, EDX/SEM, FTIR. Detailed XAS analysis suggested the presence of both metallic cobalt and cobalt oxides. The prepared Co – ppHMDSN nanocomposites are suitable as precursors for the next step of calcination. In addition to the nanocomposite preparation, the plasma process in the reaction chamber was studied using an active thermal probe. The energy influx in the chamber was measured in a pure argon and an argon + HMDSN plasma using a thermal probe. More energy was consumed by the argon + HMDSN plasma which can be accounted to the energy required for the monomer decomposition process.

In order to obtain the required spinel type cobalt oxide ( $\text{Co}_3\text{O}_4$ ) phase, the Co – ppHMDSN nanocomposite precursors were calcinated. Consequently, nanocomposites consisting of crystalline  $\text{Co}_3\text{O}_4$  nanoparticles embedded in a dielectric matrix (i.e.  $\text{Co}_3\text{O}_4$  – dielectric matrix nanocomposites) were obtained. These nanocomposite thin films were tested for the applicability as optoelectrochromic phosphate ion sensors. They displayed electrochromism. The films were stable and the electrochromic property was reproducible.  $\text{Co}_3\text{O}_4$  – dielectric matrix nanocomposites exhibited sensitivity towards phosphate ions. A linear dependence of change in transmittance on the logarithm of phosphate concentration was found. A novel type of  $\text{Co}_3\text{O}_4$  – dielectric matrix nanocomposite thin film which is suggested as optoelectrochromic phosphate ion sensor was proposed. The sensitivity is sufficient to detect environmental standard phosphate concentration ( $10^{-6}$  M).





# Contents

<b>1</b>	<b>Introduction</b>	<b>9</b>
<b>2</b>	<b>Basics</b>	<b>13</b>
2.1	Metal–polymer nanocomposites . . . . .	13
2.2	Vapor phase deposition . . . . .	14
2.2.1	Sputtering . . . . .	15
2.2.2	Hybrid PVD/PECVD process . . . . .	18
2.3	X-ray absorption spectroscopy (XAS) . . . . .	21
2.3.1	Theoretical background . . . . .	21
2.3.1.1	Physical principle - absorption and scattering of X-rays .	21
2.3.1.2	Absorption edge structure . . . . .	22
2.3.1.3	Regions in X-ray absorption spectrum . . . . .	23
2.3.1.4	XANES . . . . .	23
2.3.1.5	EXAFS . . . . .	24
2.3.2	Experimental methods of EXAFS measurements . . . . .	25
2.3.2.1	Synchrotron radiation as a source of tunable energies . .	25
2.3.2.2	Photoelectric effect . . . . .	27
2.3.2.3	XAS experimental modes . . . . .	29
<b>3</b>	<b>Experimental and characterization techniques</b>	<b>33</b>
3.1	Experimental . . . . .	33
3.1.1	Cobalt–plasma polymerized HMDSN nanocomposite thin film de- position . . . . .	33
3.1.2	Co <sub>3</sub> O <sub>4</sub> –dielectric matrix nanocomposite thin film synthesis . . . .	36
3.1.3	Energy influx measurements using active thermal probe . . . . .	37
3.1.3.1	Principle of operation . . . . .	38
3.1.4	Optoelectrochemical measurements . . . . .	40

3.2	Characterization . . . . .	42
3.2.1	X-ray diffractometry (XRD) . . . . .	43
3.2.2	X-ray photoelectron spectroscopy (XPS) . . . . .	45
3.2.3	Fourier transform infrared spectroscopy (FTIR) . . . . .	47
3.2.4	UV-Vis spectroscopy . . . . .	50
3.2.5	Electron microscopy . . . . .	50
3.2.5.1	Scanning electron microscopy (SEM)/Energy dispersive X-ray spectroscopy (EDX) . . . . .	51
3.2.5.2	Transmission electron microscopy (TEM) . . . . .	54
3.2.6	Atomic force microscopy (AFM) . . . . .	55
3.2.6.1	Conductive atomic force microscopy (CAFM) . . . . .	57
3.2.7	Three electrode electrochemical cell . . . . .	57
3.2.8	X-ray absorption spectroscopy . . . . .	59
3.2.8.1	Analysis software . . . . .	60
<b>4</b>	<b>Cobalt – plasma polymerized HMDSN nanocomposites</b>	<b>61</b>
4.1	Structural investigations . . . . .	61
4.1.1	Estimation of metal filling factor from EDX and profilometry . . .	61
4.1.2	Structure and microstructure analysis using TEM and XRD . . .	62
4.1.3	Compositional analysis using XPS and EDX . . . . .	65
4.1.4	ATR-FTIR investigations . . . . .	70
4.1.5	Surface conductivity map using CAFM . . . . .	73
4.2	X-ray absorption spectroscopy analysis . . . . .	75
4.2.1	Steps and parameters in analysing an XAS spectrum . . . . .	75
4.2.2	XAS investigations of cobalt standards . . . . .	77
4.2.3	XAS investigations of Co–ppHMDSN nanocomposites with dif- ferent metal filling factors . . . . .	81
4.2.4	Influence of the variation of plasma parameters - XAS investiga- tions of Co–ppHMDSN nanocomposites prepared with varying plasma parameters . . . . .	85
4.2.5	Influence of the variation of flow of Ar - XAS investigations of Co– ppHMDSN nanocomposites prepared with varying flow of Argon	90
4.2.6	Summary of XAS analysis . . . . .	94
4.3	Energy influx measurements using active thermal probe . . . . .	95
4.3.1	Argon plasma . . . . .	95

---

4.3.2	Argon + HMDSN plasma . . . . .	96
4.4	Conclusion . . . . .	101
<b>5</b>	<b>Co<sub>3</sub>O<sub>4</sub> – dielectric matrix nanocomposites</b>	<b>103</b>
5.1	Structural investigations . . . . .	104
5.1.1	Structural analysis using XRD . . . . .	104
5.1.2	Optical investigations using UV-Vis absorption spectroscopy . . .	105
5.1.3	ATR-FTIR investigations . . . . .	106
5.1.4	Elemental analysis using EDX . . . . .	108
5.1.5	Surface analysis using SEM . . . . .	108
5.1.6	Characterization summary . . . . .	109
5.2	Optoelectrochemical properties - phosphate ion sensor . . . . .	110
5.3	Conclusion . . . . .	115
<b>6</b>	<b>Summary</b>	<b>117</b>
<b>7</b>	<b>Outlook</b>	<b>123</b>
	<b>List of Figures</b>	<b>129</b>
	<b>List of Tables</b>	<b>131</b>
	<b>Bibliography</b>	<b>150</b>
	<b>Acknowledgments</b>	<b>152</b>



# 1 Introduction

Metal–polymer nanocomposites consisting of metal nanoparticles embedded in a polymer matrix have attracted a great deal of interest in the recent years [1]. Such nanocomposites offer a wide range of new functional properties, thus having potential uses in many areas. Notably these nanocomposites are suggested for electrical, magnetic, catalysis, optical, anti-corrosive, and biomedical applications [1]. Cobalt–polymer nanocomposites are especially interesting both for fundamental research and potential functional properties. They have been proposed for various catalytic [2, 3], optical [4], magnetic [5, 6] and gas-sensing applications [7]. A good control over the metallic properties and the oxidation state of cobalt is crucial for magnetic applications. Cobalt–polymer nanocomposites are also useful as catalysts which requires very good conductivity between the metal nanoparticles. Usually conductive polymers such as polyaniline and polypyrrole are used for this purpose. Calcinated cobalt–polymer nanocomposites have been suggested for optical gas sensor [8–10], catalytic [3], magnetic [11] and chemoresistive gas sensor [7] applications. When they are investigated as gas sensors the porous matrix provides the path through which gaseous molecules reach the functional  $\text{Co}_3\text{O}_4$  nanoparticles [12]. The gas sensing mechanism is achieved when the resistance/optical transmittance of the nanocomposites exhibit a reversible change when exposed to gases such as  $\text{H}_2$  and  $\text{CO}$  [7, 13, 14]. The gas sensitivity of these nanocomposites depend on the properties of the precursors and the amount of cobalt content in the precursors for calcination. Moreover, the temperature of calcination plays a crucial role in determining the gas sensing properties of nanocomposites. The polymer matrix helps in preventing the agglomeration of cobalt oxide nanoparticles after calcination. Suppression of agglomeration of nanoparticles is important to exploit the unique nanoscale features of the calcinated cobalt–polymer nanocomposites.

The study of the physical and chemical structure, and the applications of calcinated cobalt–polymer nanocomposites have been performed by various groups [7, 8, 11, 13, 14]. The importance of a detailed study of well-dispersed cobalt–polymer nanocomposites with various cobalt concentrations as precursors for the next step of calcination is

emphasized. The variation of size, shape, crystallinity, and the distribution of the cobalt nanoparticles in the insulating matrix is crucial to obtain cobalt–polymer nanocomposite precursors with varying properties. The concentration of cobalt in cobalt–polymer nanocomposite precursors has an impact on the properties of the final calcinated sample [8]. In addition to the cobalt content, the dispersion of cobalt nanoparticles in the matrix, the preparation method and the synthesis of precursors have an influence on the functional applications of calcinated cobalt–polymer nanocomposites. Therefore, a detailed study of cobalt–polymer nanocomposite precursors for calcination is important [13].

Several methods such as chemical synthesis [11], sol-gel techniques [8] and ion implantation [14] have been used to prepare cobalt–polymer nanocomposites. Hybrid PVD/PECVD technique is a combination of physical vapor deposition (PVD) and plasma enhanced chemical vapor deposition (PECVD) techniques to prepare metal–polymer nanocomposites with good dispersive ability. In this work the use of a hybrid PVD/PECVD technique as a simple and easy method to prepare a system of homogeneous, well-dispersed cobalt–plasma polymerized hexamethyldisilazane (Co–ppHMDSN) nanocomposites with a wide range of metal filling factors is demonstrated. The hybrid PVD/PECVD method has the advantage compared to other techniques that only one magnetron is used in this process. Plasma polymerization and magnetron sputtering take place simultaneously and there is no requirement of complex equipment to control both processes. The chamber design is simple and there is no need of high vacuum conditions. It is a dry process and does not involve multiple steps like the complex chemical synthesis processes. By changing the plasma parameters like magnetron power, gas pressure, and distance between substrate and target the metal filling factor can be varied.

In this study Co–ppHMDSN nanocomposites with metal filling factors ranging from 4% to 34% were prepared using the hybrid PVD/PECVD technique. The structure, microstructure, composition, and nanostructural surface conductivity properties of the Co–ppHMDSN nanocomposites were analyzed using various techniques. The fundamental study of the Co–ppHMDSN nanocomposites as precursors for the next step of calcination is emphasized. The use of a hybrid PVD/PECVD technique as a simple, easy and generalized method to embed metal nanoparticles in a polymer matrix is introduced. Plasma technology was employed as it offers many advantages because is a dry process and produces no waste chemicals. It allows coating of complex geometry and has low energy impact and low thermal stress on the substrate.

---

The motivation for this thesis is to prepare novel cobalt/cobalt oxide–polymer nanocomposites using plasma techniques and to study their application as optoelectrochemical phosphate ion sensors. Phosphate ions are the major cause of eutrophication (or water pollution). Moreover, the environmental concentration of phosphate ions is usually very small and changes constantly [15, 16]. Therefore, it is essential to develop cheap, sensitive devices to detect phosphate ions. Different types of inorganic phosphate ion sensors were developed by several groups. They include bio sensors [17–19], potentiometric sensors [20, 21], ion-selective electrodes [22]. A review of phosphate sensors is given by Engblom [15] and Midgley [23]. The effort to develop new type of phosphate ion sensors is always increasing. Indeed, this dissertation makes an attempt to demonstrate a new type of phosphate ion sensor. A detailed analysis and investigation of cobalt–polymer nanocomposites is presented in this dissertation. The prepared cobalt–polymer nanocomposites are later used as precursors for calcination. The calcinated sample contains  $\text{Co}_3\text{O}_4$  nanoparticles embedded in a dielectric matrix.  $\text{Co}_3\text{O}_4$  thin films were previously reported as optoelectrochemical phosphate ions sensors [24]. In this work  $\text{Co}_3\text{O}_4$ –dielectric matrix nanocomposite thin films were tested for application as optoelectrochemical phosphate ion sensors. Embedding cobalt oxide nanoparticles in a matrix increases the surface area of the nanoparticles [25–27], thus increasing the chemical reaction between phosphate ions and  $\text{Co}_3\text{O}_4$  nanoparticles. Consequently, an increased sensitivity is expected.

The work reported in this dissertation is described as follows:

1. Using a simple PVD/PECVD method Co–pp HMDSN nanocomposites with varying metal filling factors were prepared. Cobalt sputtering and simultaneous plasma polymerization was carried out in an RF sputtering reactor to prepare metal–polymer nanocomposites. Preparation of Co–pp HMDSN nanocomposites using simultaneous plasma polymerization and metal sputtering is a new effort and has not been described so far. Furthermore, hybrid PVD/PECVD is introduced as a simple and easy method to prepare metal–polymer nanocomposites in general. The nanocomposites prepared are suitable as precursors for the next step of calcination. Calcinated nanocomposites contained  $\text{Co}_3\text{O}_4$  nanoparticles embedded in a dielectric matrix.

2. Co–ppHMDSN nanocomposites were investigated using various techniques. As both PVD and PECVD processes take place simultaneously, plasma polymerization and cobalt sputtering are inter-dependent and affect each other. The variation of properties of nanocomposites with varying metal filling factor and plasma parameters was studied in detail.
3. Powerful X-ray absorption spectroscopy (XAS) technique was employed to characterize the bulk of the nanocomposites. The local structure around cobalt was thoroughly investigated using XAS. As most of the nanocomposites obtained had amorphous nanoparticles, XAS was employed to acquire the local structure and electronic information around cobalt.
4. The energy influx and power density on the substrate surface during the deposition process was measured using an active thermal probe. In pure argon plasma, with the increase in magnetron power the energy influx and power density on the substrate increased. However, in argon + HMDSN plasma sharp peaks were observed in the energy influx measurements which makes it complex to investigate the energy influx in argon + HMDSN plasma. Nevertheless, it was noticed that more energy was consumed by argon + HMDSN plasma when compared to pure argon plasma.
5.  $\text{Co}_3\text{O}_4$ –dielectric matrix nanocomposites were synthesized by the calcination of Co–ppHMDSN nanocomposite precursors. Detailed structural investigation of the calcinated samples was performed.  $\text{Co}_3\text{O}_4$ –dielectric matrix nanocomposite thin films were tested as optoelectrochromic phosphate sensors. A linear dependence of the change in transmittance on the logarithm of phosphate concentration was found. Moreover, the absolute transmittance signal ( $\Delta T$ ) of the  $\text{Co}_3\text{O}_4$ –dielectric matrix nanocomposites at a particular phosphate concentration was found to be higher than that of the standard  $\text{Co}_3\text{O}_4$  thin films. A new type of  $\text{Co}_3\text{O}_4$ –dielectric matrix nanocomposite thin film which can be applicable as an optoelectrochromic phosphate ion sensor is proposed. The sensitivity of the thin films is sufficient enough to detect environmental standard phosphate concentration ( $10^{-6}$  M).



## 2 Basics

### 2.1 Metal – polymer nanocomposites

The use of metal – polymer nanocomposites is suggested for various applications such as protection against bacteria [28], sensors [29], catalysts and fuel cells [30], optical [31], capacitor [32], anti-corrosion and passivation applications [33]. Faupel et al. [1] presented a review of various metal – polymer nanocomposites and their functional applications. Biswas et al. [34] studied the nanocomposites of teflon and various metals and also demonstrated their excellent optical properties. The magnetic properties of teflon/magnetic multilayers studied by Greve et al. [35] displayed high frequency applications. Metal – polymer nanocomposites have been prepared using various methods such as sol-gel technique [36], RF magnetron co-sputtering [37], tandem sputtering [38], electro co-deposition [33] and ion-implantation techniques [39].

Nanocomposites with cobalt nanoparticles embedded in an insulating polymer matrix are especially interesting due to their various applications in magnetic, electric, gas sensing and catalytic applications. Various methods have been used to prepare cobalt – polymer nanocomposites. Laurent and Kay [40] deposited cobalt – plasma polymerized propane nanocomposites in an RF sputtering reactor by sputtering of cobalt and plasma polymerization of propane. Nanocomposites with Ni, Fe, Co nanoparticles embedded in an SiO<sub>2</sub> matrix were prepared using RF sputter deposition technique [41]. Co – SiO<sub>2</sub> nanocomposites were also prepared by co-sputtering [42, 43], sol gel method [4], metallic salt reduction [44] and mechanical milling technique [45]. Nanocomposites of cobalt nanoparticles embedded in an organic polymer were synthesized using chemical vapor deposition [46]. In this work cobalt – plasma polymerized HMDSN nanocomposites were prepared using simultaneous cobalt sputtering and plasma polymerization technique in an RF sputtering reactor.

## 2.2 Vapor phase deposition

Vapor phase deposition is an atomistic process in which thin film deposition takes place by transporting atoms or molecules (of a source material) in the form of a vapor through vacuum or plasma to the substrate. Atomistic process means that the thin film is deposited atom-by-atom. Vapor phase deposition techniques can be broadly classified into two types:

- Chemical Vapor Deposition (CVD)
- Physical Vapor Deposition (PVD)

CVD involves the chemical reaction of the gaseous reactants on the surface of a heated substrate. The thin solid films are synthesized from the chemical reaction of the gaseous mixture. There are different types of CVD such as plasma-enhanced CVD (PECVD), metal organic CVD (MOCVD), atmospheric pressure CVD (APCVD) etc. CVD has the advantage of producing very dense, uniform and pure films. However, the use of potentially harmful chemicals can be hazardous and there is limited precursor availability.

PVD involves the physical removal of material from a source by using different processes such as evaporation or sputtering. The material is then transported through a vacuum chamber by the energy of the vapor particles and gets condensed as thin film on the substrate. In evaporation the source of the material to be deposited and the substrate both are placed in a vacuum chamber. The source material is heated to its boiling point so that it evaporates and subsequently condenses on the substrate. During sputtering the source material (target) and the substrate are placed in a vacuum chamber into which an inert or reactive gas is entered. A plasma is generated in front of the target using a power source which ionizes the gas. The ions hit the target and remove the source material which gets condensed as thin film on the substrate. PVD process produces uniform films with good quality. It is environmentally friendly and highly energy efficient. However, it is relatively expensive and has lower deposition rates when compared to CVD.

During a PVD process the vacuum in the chamber, pressure of the gases, and the chamber geometry play an important role in determining the properties of the deposited thin film. In this work a combination of PVD, i.e. sputtering, and CVD, i.e. PECVD was employed to prepare cobalt–ppHMDSN nanocomposites. Plasma enhanced chemical vapor deposition (PECVD) is a type of plasma based CVD which can be used to

deposit polymer film using plasma polymerization. It has the advantage of producing thin films with good quality and also operating at much lower temperatures when compared to conventional CVD. During plasma polymerization using PECVD, a monomer is entered into the reaction chamber. When the plasma is switched on, the monomer gets dissociated into ions and radicals which hit the substrate with high energy and thus a polymer film is deposited.

### 2.2.1 Sputtering

During a sputter deposition process ions in the plasma are accelerated towards the target which then strike it with energy and physically knock off the target atoms. The removed target material gets deposited on the substrate as thin film. In a sputtering reactor ion bombardment takes place usually with an inert gas. Ionization of the particles is done with the help of plasma which is generated by applying power to the target.

Sputtering is dependent on the transfer of physical momentum and kinetic energy from the incident particle to the target surface atoms. The angular emission distribution of the sputtered ions is dependent on the angle of incidence of the ionized particles on the target [47]. When a substrate immersed in plasma is exposed to ion bombardment several interactions take place which are schematically depicted in Figure 2.1. These ion surface interactions play an important role in the processing and properties of thin films.

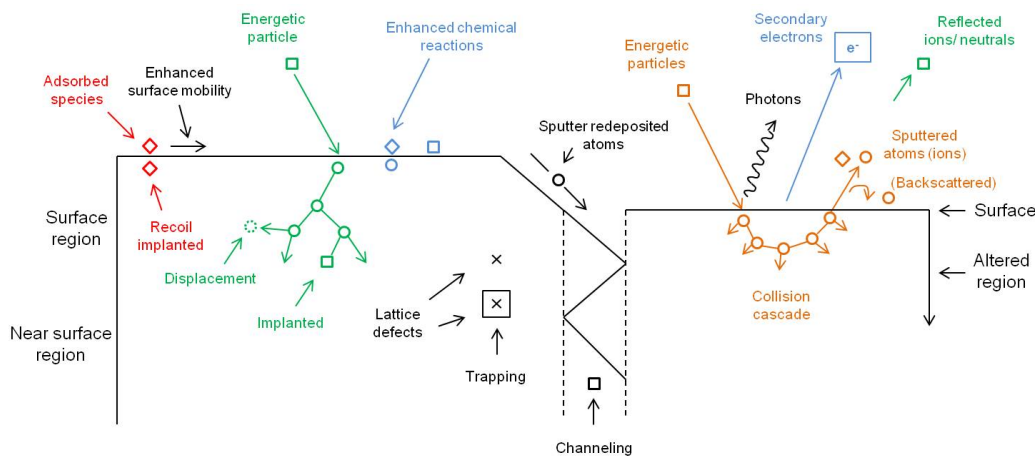


**Figure 2.1:** Schematic illustrating the energetic particle bombardment effects on surfaces and growing films [48].

A negative bias is applied to the target to attract positive ions in the plasma. Therefore, the target in sputtering is referred to as cathode. There are different types of sputtering techniques such as DC, RF, magnetron, ion-beam and reactive. Usually the common configuration of all these processes consists of a planar diode with facing anode and cathode electrodes as shown in Figure 2.2.

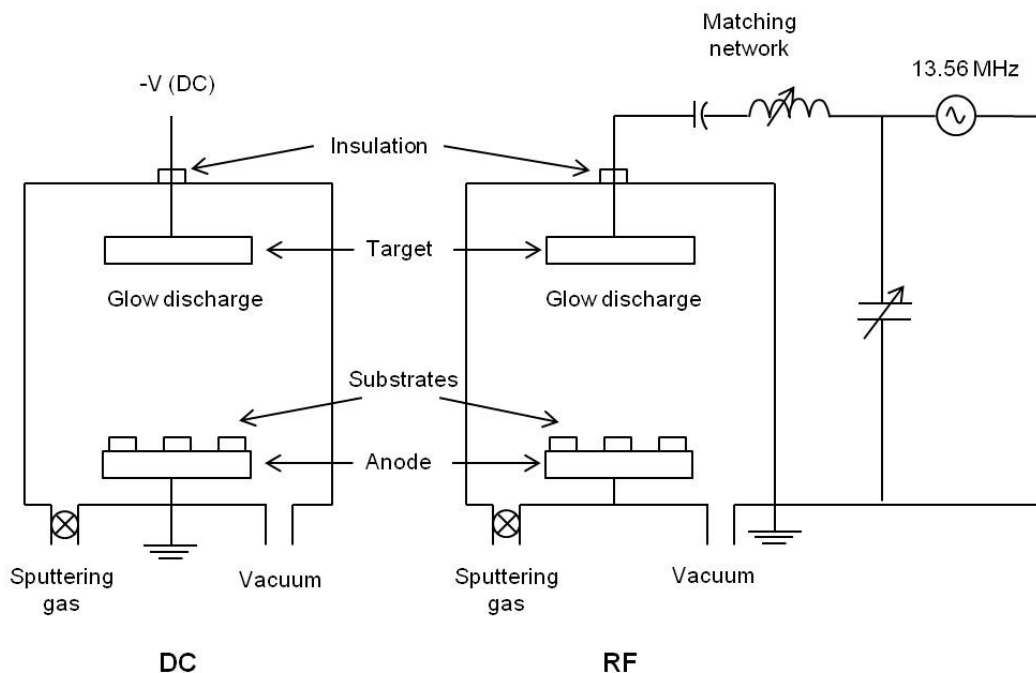


*Figure 2.2: Simplified schematic description of DC and RF sputtering systems [48].*

**DC Sputtering:** In DC sputtering a high DC voltage is applied to the target i.e. to the cathode. The plasma is generated and the positive ions are accelerated towards the target sputtering off the target atoms. DC sputtering requires an electrically conductive target otherwise the target surface gets charged up with positive ions and repels other positive ions. This would eventually stop the sputtering process.

**RF Sputtering:** In order to overcome the charge accumulation on the cathode target an AC (RF) voltage is applied to it. The power supply is operated at a high frequency, mostly 13.56 MHz. During RF sputtering the cathode and anode are electrically reversed for each RF cycle. This eliminates charge accumulation on the cathode by partially neutralising the charge built up during one half cycle with the opposite charge being accumulated during the other half cycle. This allows the sputtering of insulators and metals in a reactive environment. Also the oscillation of fields in an RF plasma causes an enhanced electron movement which increases the probability of ionization. This in

turn results in an increase in plasma density compared to DC sputtering. Thus more ions are impinged on the cathode, and the speed of sputtering process increases. The RF sputtering system requires an impedance matching network to optimise the transfer of power from the power supply to the reaction chamber.

**Magnetron Sputtering:** The sputtering rate can be increased by using magnets under the target material. The magnets cause the ions and electrons to concentrate at certain regions near the surface of the target which increases the sputtering rate. The magnetic field extends into the chamber beyond the target, and the electrons in this field are trapped and circulate over it in helical loops. These electrons in the helical loop near the target cause more ionization of neutral gases which increases the plasma density and sputter rate. This also means that magnetron sputtering can be operated at low pressures. A schematic depicting the magnetron sputtering process is shown in Figure 2.3.

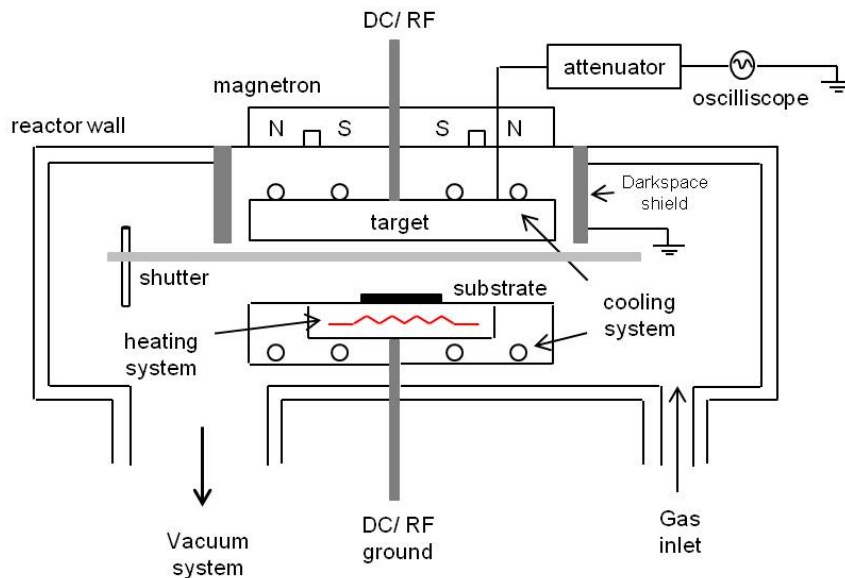


*Figure 2.3: Simplified schematic description of a magnetron sputtering system [49].*

**Sputtering targets:** The target purity, metallurgy i.e. grain size, crystallographic orientation and the design of the target for the reaction chamber crucially influence the final properties of the deposited thin film. Different kinds of PVD target shapes such as planar, conical and ring-shaped are used for sputtering. During magnetron sputtering the magnetron consumes energy and gets heated up. This in turn heats up the target and thus affects the PVD process. Target heating can cause thermal stress, cracking, undesirable outgassing of impurities, and damage to magnetron parts. Therefore, water

cooling is employed to control the target temperature.

**Advantages of sputtering [50] :**

1. Sputtering can be used to deposit any material, element, alloy and compound.
2. Using RF magnetron sputtering reactive sputtering can easily be accomplished using reactive gaseous species activated in plasma.
3. Sputtering produces films with good adhesion.
4. Sputter targets are stable and have a long life time.
5. Sputtering conditions are easily reproducible for every run.

**Disadvantages of sputtering [50] :**

1. Deposition rate in sputtering is low when compared to other techniques like evaporation.
2. Sputtering is not energy efficient as most of the energy enters the target as heat. Consequently, the targets require cooling.
3. During RF magnetron sputtering local sputtering takes place which in turn causes inefficient usage of the target.
4. Sputter targets are normally expensive.

### 2.2.2 Hybrid PVD/PECVD process

A hybrid process involves the simultaneous or sequential use of two or more surface modification techniques to obtain better functional properties when compared to the single process [51, 52]. There are various vacuum and non-vacuum [53–57] hybrid fabrication methods to prepare metal–polymer nanocomposites. Among the vacuum technologies, hybrid processes such as sputtering and PECVD, evaporation and PECVD, co-sputtering, plasma polymerization of metal organic compounds are commonly used. Hybrid PVD/PECVD is a process in which both metal sputtering (PVD) and plasma polymerization (PECVD) occur simultaneously. In this method competitive deposition of both polymer and metal takes place, i.e. both materials deposit at the same time and the growth and deposition of one material is affected by the second material [58].

Hybrid PVD/PECVD technique was first developed by Kay [59]. Since then it has been used extensively for various research and industrial purposes. It has been used to prepare nanocomposites, multilayers, doped diamond like carbon (DLC) or amorphous carbon (a:C–H) films [60]. Hybrid PVD/PECVD has the advantage of both PVD and PECVD processes occurring simultaneously. Combining PVD and PECVD is a simple, easy, cheap and efficient technique to produce nanocomposite films. Because of the hybridization of two techniques new physical phenomena may occur which strongly influence the growth, structure and properties of the resulting thin films. During the deposition the target is also affected and can get poisoned because of the presence of PECVD precursor. Thus the sputtering process (PVD) is strongly influenced by PECVD and vice versa [51].

A hybrid PVD/PECVD process usually consists of introducing a polymer precursor together with a carrier inert gas into a sputtering chamber equipped with a metallic target. It can be used to produce nanocomposites with metal nanoparticles embedded in a polymer matrix. The deposition rate of the thin film is dependent both on the sputtering rate of the metal and the rate of PECVD. The ratio of carrier gas to monomer can be adjusted to obtain a varying metal content in the polymer film. With the increase of monomer proportion, the sputtering rate of metal decreases. Simultaneously, the deposition rate of the polymer increases. It is important to control the carrier gas to monomer ratio so that the target does not get completely poisoned by the monomer. If the target is completely poisoned sputtering of the metal does not take place, and a pure plasma polymer film is formed. Nanocomposite films with homogeneous vertical and horizontal particle size distributions can be obtained using simultaneous plasma polymerization and metal sputtering [58].

Mostly fluorocarbons or hydrocarbons are used as monomers for the plasma polymerization process. Different types of metals such as Au, Ag, Cu, Mo, Co, Al are used for sputtering. In this work HMDSN was employed as monomer for plasma polymerization, and cobalt was sputtered.

### **Experimental technique: General description of the used experimental technique**

The method of simultaneous plasma polymerization and metal sputtering was developed by Kay [59]. The reactor design for this hybrid PVD/PECVD process is depicted in Figure 2.4. The reactor is made up of two horizontal parallel plate electrodes (RF diode system) which are used for plasma polymerization. Both the electrodes are water

cooled and thermally controlled. The sputter target is fixed to the lower electrode. Substrates are placed on the upper electrode. The radio frequency (13.56 MHz) power from the RF generator is coupled to the cathode target with the help of a capacitive matching network. The anode and all other metal components are grounded. The power of the RF generator can be varied. The matching network is used to minimize the reflected power. The vacuum chamber is initially evacuated to high vacuum. Argon and monomer are then entered into the chamber. Plasma polymerization takes place in the glow discharge in between the two electrodes. Simultaneous sputtering of the metal takes place resulting in the deposition of metal–polymer nanocomposite films. Depending on the ratio of argon to monomer, films with 0 to 100% metal filling factor can be deposited. When a magnetron is used in addition, the rate of sputtering and plasma polymerization increases even at the same operating power levels.

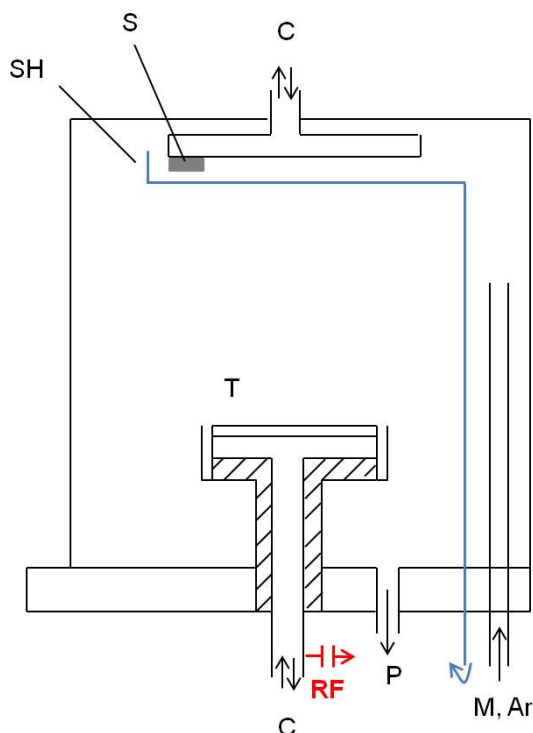


**Figure 2.4:** Schematic of parallel plate electrode (RF diode) system used for simultaneous plasma polymerization and metal sputtering [61]. *M* - monomer, *Ar* - argon, *S* - substrate, *SH* - shutter, *RF* - to RF power supply, *P* - to pumps, *C* - to cooling, *T* - metal target.



## 2.3 X-ray absorption spectroscopy (XAS)

X-ray absorption spectroscopy (XAS) is a unique tool to study the physical and chemical structure around a specific element of a material at an atomic scale. XAS is a technique which has gained popularity in the last few decades with the increase in the number of synchrotron radiation sources. It can be applied not only to crystals but also to materials which have low or no range of crystallinity. It is based on the principle of photoelectric effect. The basic quantity that is measured is the X-ray absorption coefficient  $\mu(E)$ . It describes how strongly the X-rays are absorbed as a function of X-ray energy 'E' [62, 63].

The electronic and structural properties around a specific element in a material can be studied using XAS. X-ray diffractometry (XRD) is also similar to XAS in this regard but requires long range order crystals [64]. Electronic information can also be obtained from X-ray photoelectron spectroscopy (XPS) but requires high vacuum conditions. XAS is a technique which can be used to characterize the material geometrically and electronically even for a short or no range of crystallinity.

### 2.3.1 Theoretical background

#### 2.3.1.1 Physical principle - absorption and scattering of X-rays

When an X-ray beam of intensity ' $I_0$ ' is passed through a material of thickness 'x' a part of the beam is absorbed by the material and the intensity gets reduced to 'I' which can be expressed as

$$I = I_0 \exp(-\mu(E)x) \quad (2.1)$$

where  $\mu(E)$  is the linear absorption coefficient as a function of X-ray photon energy, ' $I_0$ ' is the intensity of incident X-rays, and 'I' is the intensity of transmitted X-rays. The oscillating electric field of the incident X-rays interacts with the electrons bound in the atom. When the incident X-ray energy is large enough to excite a core electron to a vacant state in continuum a sharp, sudden increase in the absorption intensity occurs. This sharp rise in absorption intensity is called 'absorption edge' and the energy at which it occurs is called the threshold energy. Figure 2.5 shows the plot of linear absorption coefficient  $\mu(E)$  of a foil of cobalt metal as a function of X-ray energy 'E'.

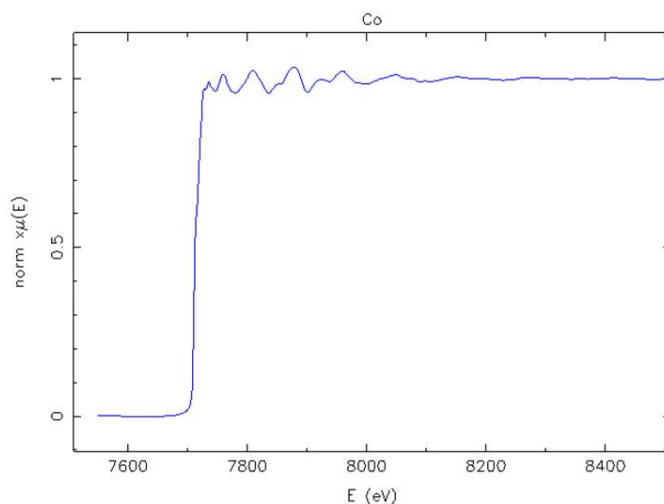


**Figure 2.5:** Normalized X-ray absorption spectrum of cobalt metal as a function of X-ray energy.

### 2.3.1.2 Absorption edge structure

When an X-ray of energy ‘E’ is incident on an atom with a core electron binding energy of ‘ $E_0$ ’ the following possibilities can happen:

1. If  $E < E_0$  the atom will not absorb the X-ray and the core electron will not be ejected. Only electronic transitions within the atom can take place which result in sharp pre-edge peaks before the absorption edge. This is the pre-edge region in the absorption spectrum.
2. If  $E \sim E_0$  photoelectrons are ejected to continuum. This is the absorption edge. The sharp absorption edges in the spectrum of absorption coefficient correspond to the characteristic core level energies of the atom.
3. If  $E > E_0$  the photoelectron is ejected to continuum with a kinetic energy of  $E_k = E - E_0$ . This is the post-edge region in the spectrum.

The ejected photoelectron can be viewed as a scattered wave which is scattered off from the neighboring atoms. The outgoing and backscattered waves interfere either constructively or destructively. The distance between the neighboring atoms affect the process of interference. The measured absorption coefficient of the absorbing atom is dependent on these interference effects between the outgoing and backscattered electronic waves. These interference effects cause an energy-dependent variation in the X-ray ab-

sorption probability which in turn is proportional to  $\mu(E)$ . These variations are observed as oscillations in the absorption spectrum  $\mu(E)$ .

### 2.3.1.3 Regions in X-ray absorption spectrum

Traditionally the X-ray absorption spectrum has been divided into two regions:

1. XANES - X-ray Absorption Near Edge Structure
2. EXAFS - Extended X-ray Absorption Fine Structure.

Illustratively, the two regions of the X-ray absorption spectrum of powdered  $\text{Co}_3\text{O}_4$  sample are shown in Figure 2.6.

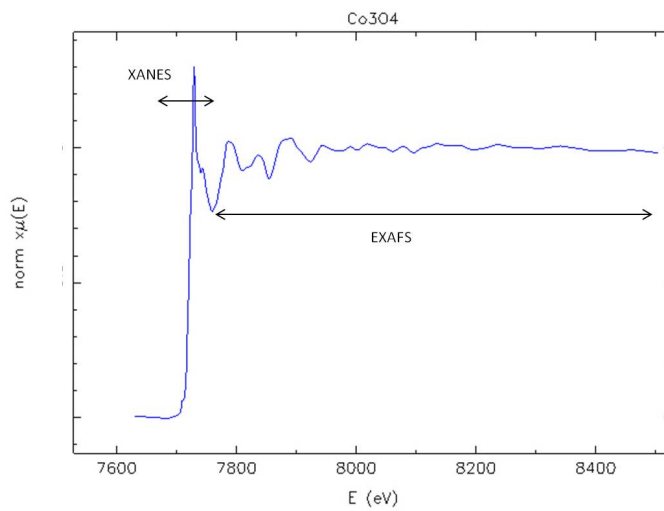


**Figure 2.6:** Normalized X-ray absorption spectrum of  $\text{Co}_3\text{O}_4$  powder sample as a function of X-ray energy. The different regions in the X-ray absorption spectrum are depicted.

### 2.3.1.4 XANES

XANES is the region which is  $\sim 50$  eV around the absorption edge in the absorption spectrum. This also includes the absorption edge. Sometimes there is a sharp peak or a high increase of intensity at the absorption edge. This is called the ‘white line’. It is due to the transition of core electrons to unoccupied energy levels near the continuum [62]. The peaks in the pre-edge region and the position of the absorption edge give information about the local structure around the element of interest.

XANES gives information about

- Oxidation state of the absorber
- Coordination number of the absorber, i.e. the local coordination environment around the absorber
- Covalency of the absorber
- Site symmetry around the absorber

The edge position and the peaks in pre-edge give information about the valency of the absorber atom. The intensity of the pre-edge peak gives information about site symmetry. The absorption edge shifts with the change in the oxidation state of the absorbing atom. The absorption edge shifts to higher energies with increase in oxidation state. XANES is sensitive to the formal oxidation state and geometry of the absorber atom.

#### 2.3.1.5 EXAFS

EXAFS is the oscillating part of the X-ray absorption spectrum which lies at  $\sim 50$ – $1000$  eV above the absorption edge. The EXAFS phenomenon is because of the interference between the wave functions of the ejected photoelectron and the backscattered electron.

The EXAFS region in the spectrum gives the following information about the absorber atom:

- the number of neighbors
- the nature of neighbors
- the distance between absorbing and neighboring atoms

#### EXAFS function $\chi(E)$

The EXAFS modulation function  $\chi(E)$  represents the modulation in the absorption coefficient of the central absorbing atom. The EXAFS function  $\chi(E)$  is defined as

$$\chi(E) = [\mu(E) - \mu_0(E)]/\Delta\mu_0(E_0) \quad (2.2)$$

where  $\mu(E)$  is the measured absorption coefficient,  $\mu_0(E)$  is the atomic background absorbance or calculated absorption coefficient of atom without the contribution from neighboring atoms,  $\Delta\mu(E_0)$  is the edge step measured at threshold energy  $E_0$ , and  $E_0$  is the threshold energy of the absorption edge, i.e. energy where the photoelectron is released.

The steps required in analyzing the XAS spectrum and extracting the EXAFS function  $\chi(k)$  are:

1. Pre-edge background removal by subtracting a smooth polynomial function. This removes the effects of instrumental background and absorption from other edges.
2. Normalization of the absorption spectrum  $\mu(E)$ .
3. Edge position determination and identification of the threshold energy  $E_0$ .  $E_0$  is evaluated as the energy at the value of first derivative of  $\chi(E)$ .
4. Atomic background removal or post-edge background removal using a spline function  $\mu_0(E)$ . Transformation of EXAFS spectrum to k-space to extract k-weighted EXAFS function  $\chi(k)$ .
5. Fourier transform of  $\chi(k)$  from k to R space resulting in pseudo radial distribution function (PRDF). The two major peaks correspond to the first and second coordination shells around the absorber atom.
6. Isolation of coordination shell and back transformation to k-space (Fourier back transform). The contribution of individual peaks in  $\chi(k)$  can be seen by back Fourier transform of peaks from R-space to k-space.

A detailed description of the above steps using a cobalt standard analysed at the BESSY synchrotron radiation center is presented in Chapter 4, Section 4.2.

## 2.3.2 Experimental methods of EXAFS measurements

### 2.3.2.1 Synchrotron radiation as a source of tunable energies

Synchrotrons are large, expensive national/international facilities. The growth of synchrotron radiation facilities in the recent years has led to the extensive development of XAS technique. A synchrotron is a particle (electron, proton, and neutron) accelerator. Sayers, Stern, and Lytle [65] developed the first useful X-ray facilities using synchrotron.

Synchrotron radiation can be used to produce X-rays with desirable characteristics. It is produced by accelerating charged particles having a speed close to that of light in a storage ring of tens to hundreds meters of diameter under high vacuum. When the electron is travelling at nearly the speed of light in a circular orbit, electromagnetic synchrotron radiation is emitted tangential to the orbit. Synchrotrons produce intense, tunable and highly-focused X-ray beams.

The electrons are forced to follow the curvature of the ring using external magnetic fields from strong magnets around the ring. The wavelength of the X-rays can be tuned by changing the magnetic field using wigglers and undulators. A schematic description of synchrotron is shown in Figure 2.7.

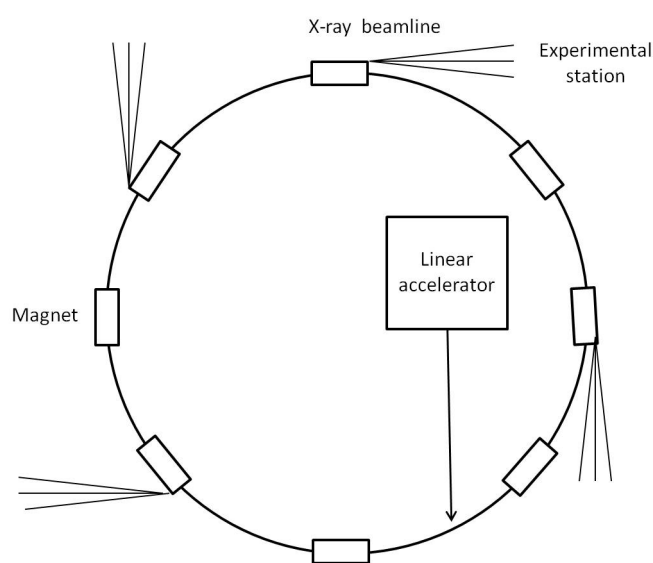


*Figure 2.7: Schematic of a synchrotron radiation source*

Synchrotron radiation is a source of stable, tunable X-ray beam. As an X-ray source it possesses the following advantages:

- **Tunability:** The energy of the X-rays can be tuned from infrared to hard X-rays. This gives the flexibility to perform X-ray absorption spectroscopic studies specifically on almost every element in the periodic table. Also the tunable energies help in obtaining the absorption coefficient over a range of energies which is important for the analysis of XAS spectrum.
- **Intensity:** Good Signal-to-Noise ratio (SNR) is required for EXAFS and XANES analysis. For this an intense X-ray beam is required for a reasonable amount of

time (a few minutes to hours). Such requirements are satisfied by a synchrotron radiation source [63].

- **Brilliance:** A high brilliance of the X-rays (photons/volume) can be obtained using a synchrotron.
- **High energy:** The high energy beam of synchrotron radiation is used to penetrate deep into the matter.
- **Collimated:** The X-ray beam is highly collimated which results in less wastage of the radiation.
- **Speed:** The X-ray beam from a synchrotron is of high intensity resulting in much faster data collection with high resolution.
- **Resolution:** The resolution range of the X-rays can be varied using various monochromators.

The major disadvantage of the synchrotron facility is that it is very expensive and rarely available at national/international labs.

### **Beamline for EXAFS spectroscopy**

When electrons move in the storage ring and encounter a trajectory or bend, the electrons are accelerated. These accelerated electrons emit electromagnetic radiation. This emitted electromagnetic radiation is selected for a wavelength at a beamline. Experiments are performed at the end of beamlines where shielded user stations called ‘hutch’ are present. Beamlines are complex instruments which safely convey the X-rays produced by the synchrotron to the users. They employ appropriate shielding to synchrotron radiation to prevent accidental radiation. Beamlines also prepare the incoming beam for the experiment by performing various functions such as filtering, monochromatising and focussing using X-ray optics [63].

#### **2.3.2.2 Photoelectric effect**

XAS is based on the principle of photoelectric effect. When an X-ray is incident on an atom it is being absorbed when the energy is transferred to a core level electron and eventually the core level electron is ejected from the atom. This ejected electron is called the photoelectron. The photoelectric effect is described schematically in Figure 2.8.

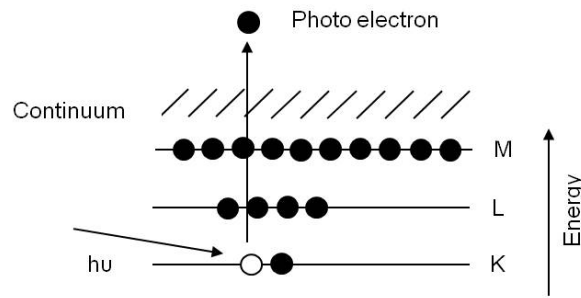


*Figure 2.8: Schematic illustration of the photoelectric effect.*

The empty level of the core electron is called ‘hole’. To fill in this empty hole an electron from higher level drops into the core hole resulting in the emission of Fluorescent X-ray or Auger electron. X-ray fluorescence occurs when electron from higher level falls into the core hole and fluorescence radiation is emitted with an energy equal to the difference of the two levels. Auger electron emission takes place when an electron from higher level falls into the core hole, but the energy gets transferred to another electron of a higher level which leaves the atom with a characteristic kinetic energy (energy difference between higher level and core level minus binding energy of the leaving electron minus work function of the material). Thus, an Auger electron is emitted when an electron is promoted to the continuum from the core level. The X-ray fluorescence and Auger effects are schematically illustrated in Figure 2.9 and Figure 2.10 respectively. The X-ray fluorescence and Auger emission occur at discrete energies characteristic of the absorbing atom.

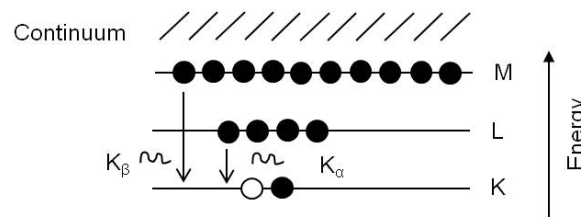


*Figure 2.9: Schematic illustration of the X-ray fluorescence effect [66].*



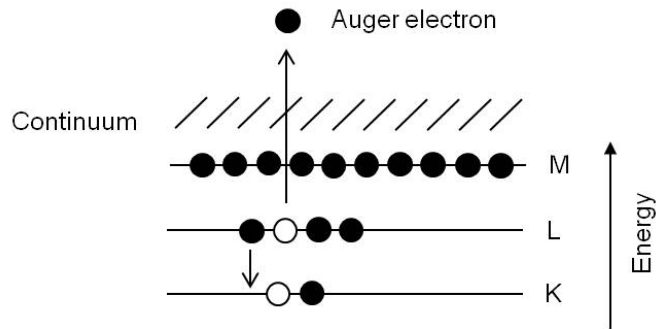


*Figure 2.10: Schematic illustration of Auger effect [66].*

### 2.3.2.3 XAS experimental modes

When an X-ray beam of intensity  $I_0$  is incident on a sample a part of the incident energy is absorbed by the sample. The intensity of the transmitted beam 'I' is related to the incident flux as

$$I = I_0 \exp(-\mu t) \quad (2.3)$$

where  $\mu$  is the absorption coefficient and 't' is the thickness of the sample.

#### Transmission mode

During a transmission mode the X-ray beam intensity is measured before and after the beam is passed through the sample. In this mode the sample is placed perpendicular to the X-ray beam and the X-ray intensity is measured before and after the sample. The ion chambers are mostly filled with gases or gas mixtures which absorb the X-ray beam and serve the purpose of detectors. The measured absorption coefficient in transmission mode is denoted as

$$\mu = \ln(I_0/I_t) \quad (2.4)$$

where  $I_0$  is the intensity of the incident X-rays and  $I_t$  is the intensity of transmitted X-rays.

## Fluorescence mode

In this mode the incident intensity  $I_0$  and the intensity of the fluorescence X-rays emitted after the X-ray absorption are measured. The fluorescence detector is placed at  $90^\circ$  to the incident beam and the sample is placed at  $45^\circ$  to the incident beam. The fluorescence X-rays are detected by the PIN diode detector. The measured absorption coefficient in fluorescence mode is denoted as

$$\mu = I_f/I_0 \quad (2.5)$$

where  $I_0$  is the intensity of the incident X-rays and  $I_f$  is the intensity of fluorescence X-rays

The schematic description of transmission and fluorescence modes of operation is illustrated in Figure 2.11. Transmission method is typically used for samples with high concentration ( $> 2$  weight %) of the absorber, whereas the fluorescence measurement is used for low concentration ( $< 2$  weight %) of the absorber.

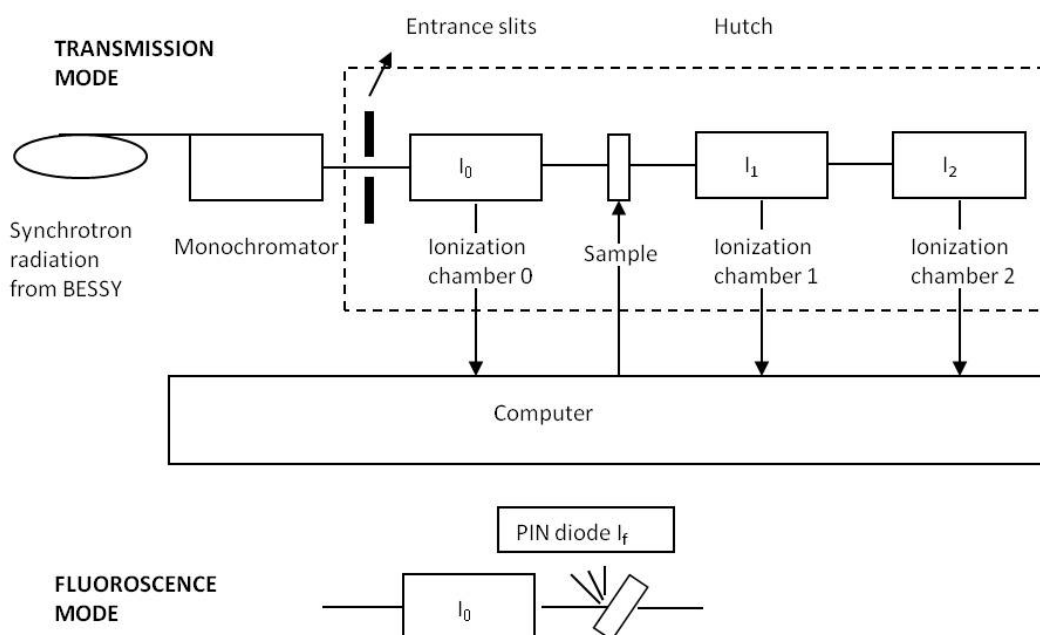


*Figure 2.11: Schematic illustration of transmission and fluorescence modes of XAS [63].*

## Monochromator

For XAS measurements an X-ray beam of approximately 1 eV bandwidth is required so that the fine features of XANES and EXAFS could be resolved. The beam produced by synchrotron is generally tens to thousands of eV in bandwidth. Monochromators are used to reduce the bandwidth to about  $\sim 1$  eV. Usually a double crystal monochromator is used in which the crystals are parallel to each other. The first crystal is used to make the incident beam monochromatic and the second one to keep the outgoing beam parallel to the incident beam.



# 3 Experimental and characterization techniques

The experimental and characterization techniques used for the synthesis and analysis of nanocomposites are described in this chapter.

## 3.1 Experimental

The experimental work performed in this work is as follows:

1. Deposition of Co–ppHMDSN nanocomposites in an RF magnetron sputtering reactor.
2. Calcination of Co–ppHMDSN nanocomposites to prepare  $\text{Co}_3\text{O}_4$ –dielectric matrix nanocomposites.
3. Structural analysis and optoelectrochemical investigations of  $\text{Co}_3\text{O}_4$ –dielectric matrix nanocomposites in  $\text{Na}_2\text{HPO}_4$  solutions of various concentrations.
4. Measurement of energy influx and power density of the plasma process in the reaction chamber using an active thermal probe.

The experimental work is described in detail in the following sections.

### 3.1.1 Cobalt – plasma polymerized HMDSN nanocomposite thin film deposition

Co–ppHMDSN nanocomposites were prepared using a hybrid PVD/PECVD technique. Cobalt was sputtered from an RF magnetron source which corresponds to the physical vapor deposition (PVD) process. HMDSN monomer was polymerized using plasma

polymerization. The polymerization process of HMDSN monomer corresponds to a plasma enhanced chemical vapor deposition (PECVD) process.

Nanocomposite deposition was carried out in a cylindrical stainless steel chamber equipped with two radio-frequency (RF) sources operated at 13.56 MHz. A schematic of the sputtering reactor is shown in Figure 3.1. The internal radius of the cylindrical chamber is 30 cm and the height is 20 cm. The chamber was evacuated using a rotary pump (Trivac, Leybold) to a base pressure of about 0.1 Pa. The power supplied to the magnetron can be varied from 0 W to 300 W by controlling a Cesar 136 generator. Cobalt (Advanced Energy, 103.9 mm target, 99.9%) was sputtered from the RF magnetron source. The monomer used was hexamethyldisilazane HMDSN ( $\text{Si}(\text{CH}_3)_3\text{-NH-Si}(\text{CH}_3)_3$ ) without further purification (supplied by Merck). Argon was employed as a feed gas for the ignition of plasma. The flow of Argon and HMDSN was controlled by MKS flow meters. For the preparation of pure plasma polymerized HMDSN film only the RF electrode (diameter 128 mm) was operated. Only the magnetron electrode was used to prepare the Co-ppHMDSN nanocomposites. The upper RF electrode was covered with an aluminum foil for all Co-ppHMDSN nanocomposites. The magnetron was cooled by water. The flow of Ar and the magnetron power were varied to obtain nanocomposites with different metal filling factors. The flow of HMDSN was kept constant at 0.06 sccm whereas that of Argon was varied from 1 sccm to 8 sccm leading to operating pressures of 3.8–18 Pa. The magnetron power was varied from 100 to 300 W. The substrate was placed on a specially designed substrate holder facing the magnetron so that the yield of the sputter deposition process is maximized. The distance between the substrate and the target was 6 cm.

Initially the deposition rate of the cobalt metal was high. But with increase in time some of the polymer gets deposited onto the surface of the cobalt target which decreases the deposition rate of cobalt onto the substrate. After a certain amount of time the deposition rate which was initially high would come to a constant. The nanocomposites were prepared under such stationary deposition conditions. A shutter was used for this purpose during the deposition process. The substrate was shielded from the RF magnetron using the shutter. The shutter was kept closed until stationary deposition conditions were formed in the chamber. Once these conditions were obtained the shutter was opened, and the sample/substrate was exposed to the RF magnetron target. The schematic of the reaction chamber depicting the different valves, rotary pump and butterfly valve is shown in Figure 3.2. The position of the butterfly valve can be varied. During the deposition process the the butterfly valve was kept completely

open. The cobalt target was cleaned with sand paper and iso propanol after every deposition process. A photograph depicting the sputtering reactor used is shown in Figure 3.3.

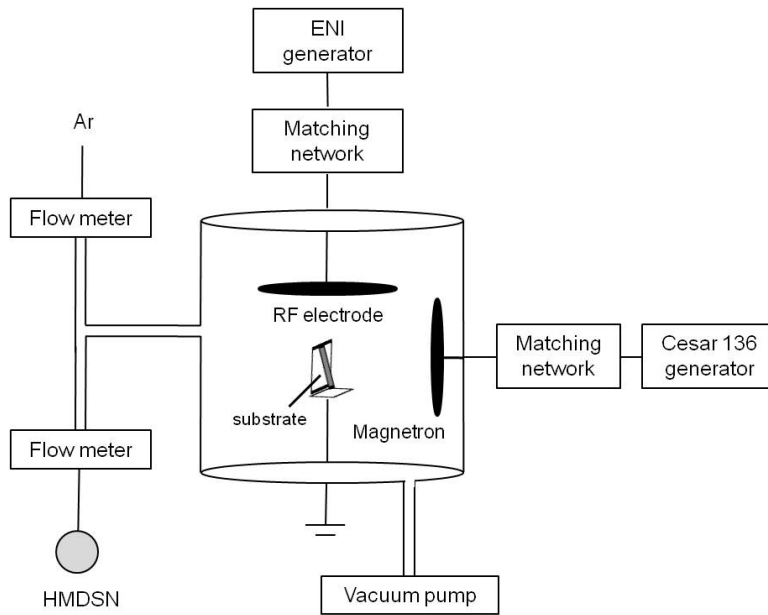


**Figure 3.1:** Schematic of sputtering reactor used to prepare cobalt–plasma polymerized HMDSN nanocomposites.

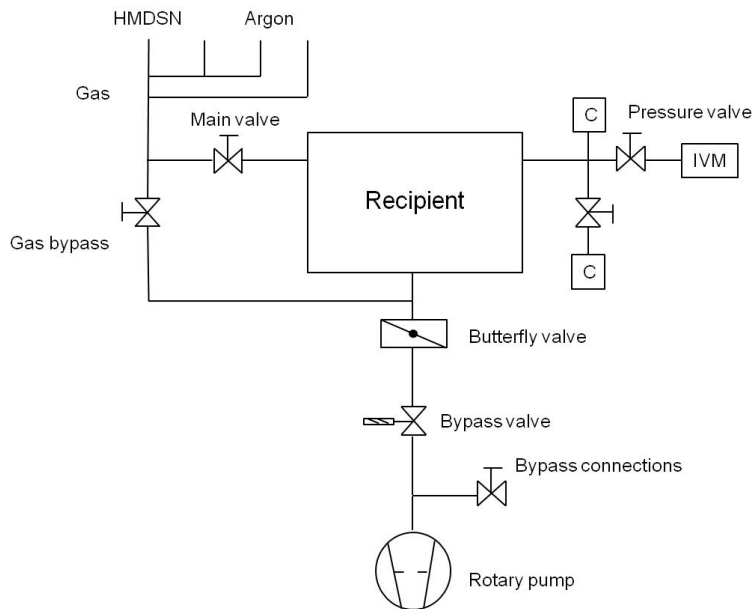


**Figure 3.2:** Schematic of sputtering reactor used to prepare cobalt–plasma polymerized HMDSN nanocomposites. Various valves are also depicted.



*Figure 3.3: Photograph of sputtering reactor used to prepare cobalt–plasma polymerized HMDSN nanocomposites.*

### 3.1.2 $\text{Co}_3\text{O}_4$ – dielectric matrix nanocomposite thin film synthesis

Initially Co–ppHMDSN nanocomposites were prepared by the sputtering of cobalt (PVD) and simultaneous plasma polymerization of hexamethyldisilazane (HMDSN) (PECVD) (See Chapter4). The process was carried out in an RF magnetron sputtering system operating at 13.56 MHz frequency. These Co–ppHMDSN nanocomposites were used as precursors for the next step of calcination. They were calcinated in air in a quartz tube furnace at 500° C. Calcination proceeded at the rate of 10° C/min until a temperature of 500° C was reached. From a temperature of 500° C the samples were calcinated for about 1 hour. After 2 hours the temperature was allowed to come down naturally. The samples were removed from the furnace after the furnace reached the room temperature. The process of calcination yielded in the formation of nanosized spinel type cobalt oxide ( $\text{Co}_3\text{O}_4$ ) particles embedded in a dielectric matrix.



### 3.1.3 Energy influx measurements using active thermal probe

Plasma wall interactions have a large influence on the plasma process. The interaction of the plasma on the surface of the substrate plays an important role in the plasma deposition process. The thermal and energetic conditions on the surface of the substrate significantly contribute to affecting the structural and morphological characteristics of the nanocomposites [67]. In low temperature plasma process the interaction of the plasma on the substrate surface is influenced by the energy per incoming particle and the particle flux density on the substrate surface. During the plasma process the temperature of the substrate surface varies. This in turn affects the various surface processes like adsorption, desorption, diffusion and chemical reactions [68–71].

To quote according to Kersten et al. [72], “the total power input  $\dot{Q}_{in}$  at the substrate surface is the surface integral over the sum of different contributions  $J_\nu$  (energy flux per time and area)

$$\dot{Q}_{in} = \int (J_{rad,1} + J_{ch} + J_n + J_{ads} + J_{react,1} + J_{ext,1}) dA \quad (3.1)$$

where  $J_{rad,1}$  is the heat radiation towards the surface,  $J_{ch}$  is the power transferred by charge carriers (electrons and ions), and  $J_n$  is the contribution of neutral species of the background gas and the neutral particles contributing to the film growth.  $J_{ads}$  is energy released by absorption or condensation,  $J_{react,1}$  is the reaction energy of exothermic processes including molecular surface recombination.  $J_{ext,1}$  is the power input by the external sources which influences the thermal balance of the substrate”.

The active probe can be placed at the position of the substrate in the reaction chamber and the energy influx can be measured. It is possible to study and correlate the effect of the plasma parameters on the energy influx on the substrate surface. The thermal probe is sensitive to the process parameters and can be used as a tool to control the thin film growth. A continuously working active thermal probe is used to measure the total energy influx on the surface of the substrate during the sputtering process. The energy influx was measured in two kinds of plasma environments: pure argon plasma and argon + HMDSN plasma. In pure argon plasma no HMDSN was entered into the chamber. Sputtering of cobalt target takes place under these conditions. Only argon plasma in the reaction chamber indicates the physical vapor deposition (PVD) process. Instead, when both argon and HMDSN are entered into the reaction chamber a hybrid PVD/PECVD process will take place in the reaction chamber.

The energy influx on the substrate is measured using an active thermal probe. The power density on the surface of the substrate and the energy influx are determined. With the help of a controlled electrical heating the probe is set to a given working temperature and then the energy supply supporting the given working temperature is measured. The energy influx by external sources (plasma) is compensated by decreasing the heating power, and thus the energy influx is measured. A photograph of active thermal probe is shown in Figure 3.4.



*Figure 3.4: Photograph of the active thermal probe used to measure the energy influx in the sputtering chamber [73].*

#### 3.1.3.1 Principle of operation

An active thermal probe works on the principle of ‘measurement based on the incoming energy influx’[73]. Using external controllable electrical heating the thermal probe is set to a given working temperature. When the plasma is switched ON the energy influx on the probe changes. Thus, the temperature on the surface of the probe also changes. The temperature is kept constant at the set value by varying the energy supplied. The energy supplied to keep the set temperature constant is measured. The energy influx by external sources is compensated by decreasing the heating power and is directly displayed in mW.

The operation and working of the thermal probe is depicted in Figure 3.5. Initially the probe is set to work at a fixed working temperature. When the plasma is switched ON the temperature of the probe increases and the external control unit reacts by decreasing the heating power. After some time the temperature balance level is reached again. The energy influx by plasma is obtained by determining the change in the heating power. The power density of the plasma on the substrate surface is calculated by dividing the heating power with the area of the active probe. The area of the active probe of the thermal probe used in this study is  $0.42 \text{ cm}^2$ . The working temperature of the active thermal probe was set at  $340^\circ \text{ C}$ . The active thermal probe was placed in the

reaction chamber at the same position as the substrate. Thus the energy influx on the surface of the substrate was measured by placing the active thermal probe on the site of the substrate. Figure 3.6 depicts the front and back view positioning of the thermal probe in the reaction chamber.

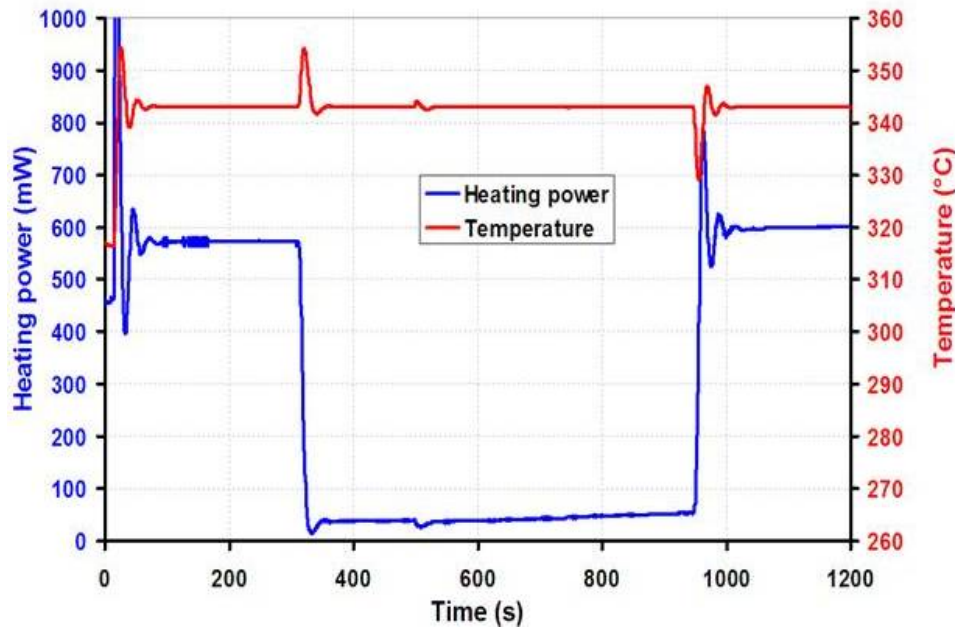


*Figure 3.5: Variation of probe temperature and heating power depicting the working of the active thermal probe [73].*

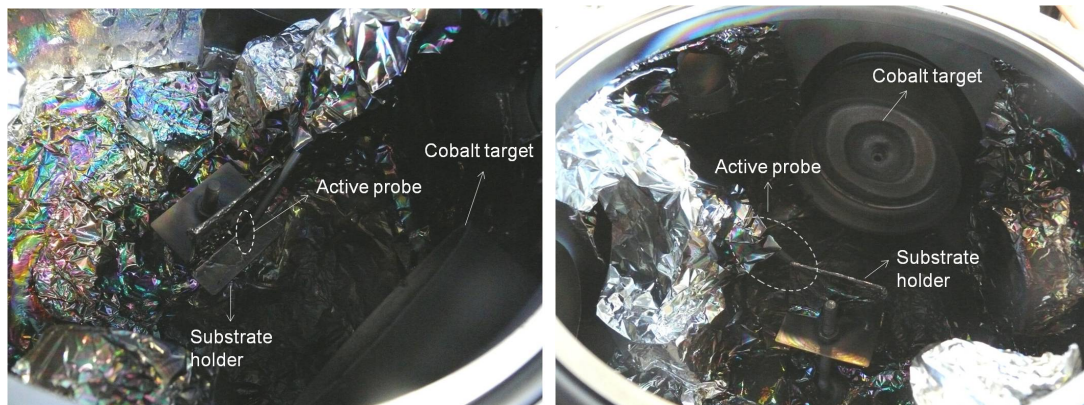


*Figure 3.6: a) Front and b) Back view positioning of active thermal probe in the reaction chamber.*

### 3.1.4 Optoelectrochemical measurements

$\text{Co}_3\text{O}_4$ –dielectric matrix nanocomposite thin films of thickness  $\sim 100$  nm were prepared on thoroughly pre cleaned and dried conductive fluorine-doped tin oxide (FTO) substrates (Solaronix). FTO substrates were cleaned in several stages. Firstly, the substrates were immersed in acetone on an ultrasonic bath for 30 min, then in ethanol on an ultrasonic bath for 30 min. Later they were placed in 20% nitric acid solution for 5 min. Then the samples were washed several times in double distilled water together with an ultrasonic bath treatment. After the cleaning process the FTO substrates were dried at  $150^\circ\text{C}$  for an hour. The size of the substrates was  $2.5\text{ cm} \times 2.5\text{ cm}$ . During deposition masks were placed on the four corners of the FTO substrate which were removed after the process. The masks help in establishing the electrical connection between the  $\text{Co}_3\text{O}_4$ –dielectric matrix nanocomposite thin film and the three electrode electrochemical cell.

Electrochemical investigations were performed using an AUTOLAB Type III potentiostat/galvanostat.  $\text{Co}_3\text{O}_4$ –dielectric matrix nanocomposite thin films were used as working electrodes, Platinum (Pt) as the counter electrode and silver/silver chloride (Ag/AgCl (3 M NaCl)) as the reference electrode. A stock solution of 0.1 M  $\text{Na}_2\text{HPO}_4$  was prepared. Phosphate solutions of concentrations  $10^{-6}$  M,  $10^{-5}$  M,  $10^{-4}$  M,  $10^{-3}$  M,  $10^{-2}$  M mixed with 0.1 M ammonium acetate-ammonia buffer solution adjusted to a pH = 9.3 were prepared. These solutions were used as the electrolytes. The complete electrochemical cell was mounted in the spectrophotometer in such a way that the UV-Vis radiation passes through the working electrode ( $\text{Co}_3\text{O}_4$ –dielectric matrix nanocomposite thin film). A schematic of the experimental set up is shown in Figure 3.7.

When a potential is applied to the nanocomposite thin film electrochemical reactions take place. This causes change in the optical transmittance which was simultaneously measured by a UV–Vis spectrophotometer. A Perkin Elmer Lambda 850 spectrometer was used. The optical transmittance of the working electrode immersed in phosphate solutions of various concentrations and at various applied potentials was measured. A photograph of the experimental set up is shown in Figure 3.8.

Figure 3.9 depicts the placement of the working electrode inside the electrochemical cell. The four corners of the FTO substrate where the masks were removed indicate the electrical connection between the working electrode i.e.  $\text{Co}_3\text{O}_4$ –dielectric matrix nanocomposite and the electrochemical cell.

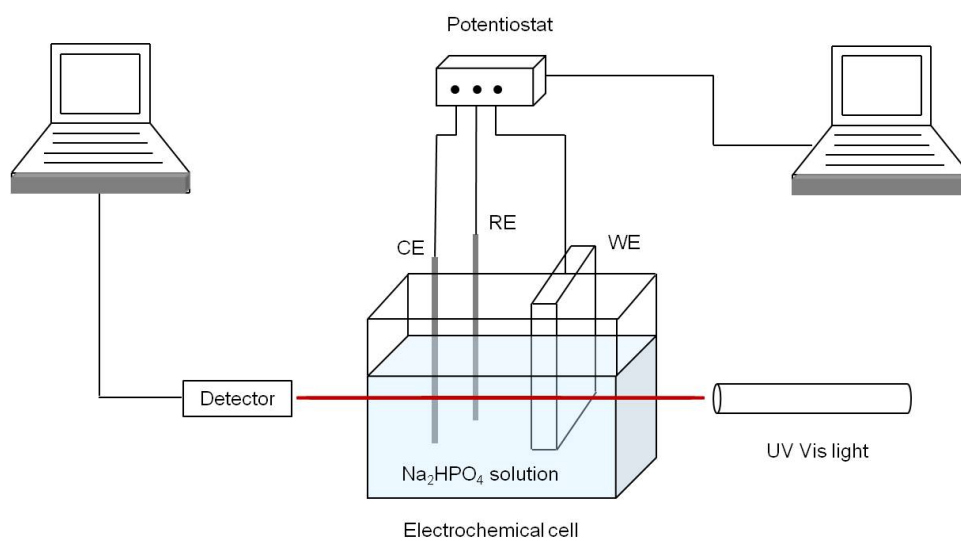


*Figure 3.7: Schematic of experimental set up for optoelectrochemical measurements. WE: Working electrode ( $\text{Co}_3\text{O}_4$  - dielectric matrix nanocomposite thin film).*

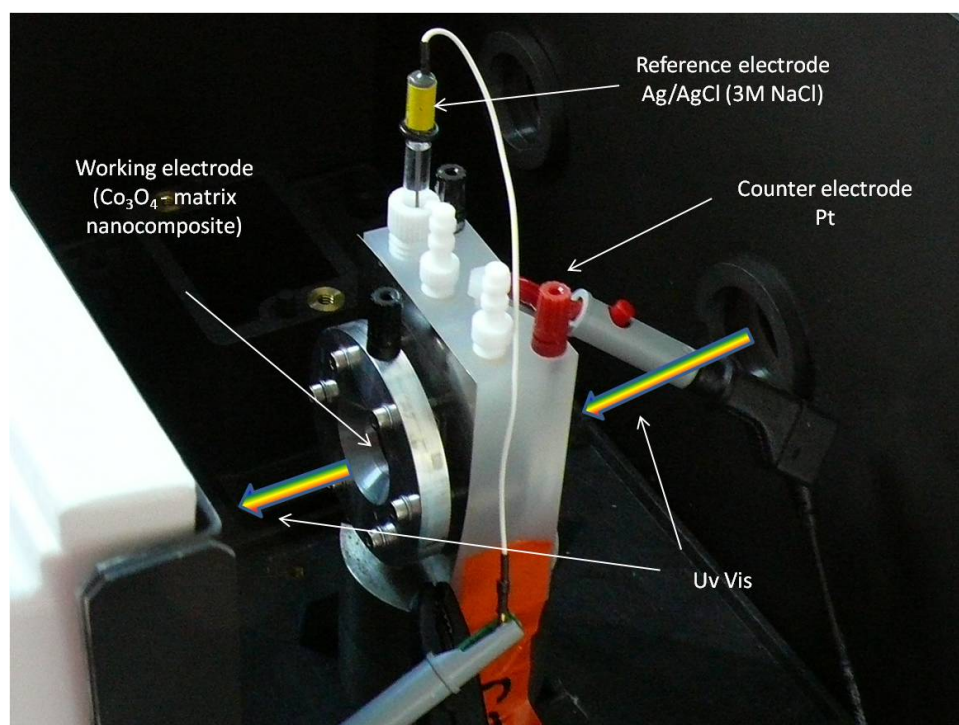


*Figure 3.8: Photograph of experimental setup for optoelectrochemical measurements.*

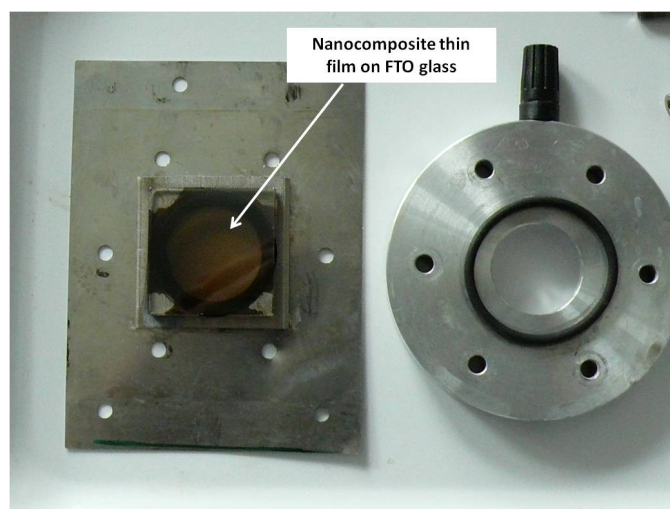


**Figure 3.9:** Photograph depicting the placement of the working electrode ( $\text{Co}_3\text{O}_4$  – dielectric matrix nanocomposite thin film) in the three electrode cell.

## 3.2 Characterization

Phase composition of the nanocomposites was investigated by X-ray diffraction (XRD) using  $\text{CuK}_\alpha$  radiation ( $\theta$ - $2\theta$  Diffractometer Siemens D5000). Samples prepared on aluminum substrates were used for XRD analysis to estimate the particle size. The measurements were made in grazing incidence (highly asymmetric Bragg case) set at an angle of  $0.5^\circ$  to the sample surface. The determination of the cobalt concentration in the nanocomposite was made with an energy dispersive X-ray spectroscopy (EDX) system (Bruker X-Flash spectrometer) with a  $30\text{ mm}^2$  silicon drift droplet detector specified with energy resolution of 127 eV. For EDX analysis Co–ppHMDSN nanocomposites were prepared on aluminum substrates. For the optimal count rate during the EDX analysis, the acceleration voltage of the electron beam was adjusted to 5 kV. Compositional analysis was performed using X-ray photoelectron spectroscopy (XPS) and Fourier transform infrared spectroscopy (FTIR). For XPS analysis the samples were prepared on teflon substrates and for FTIR on aluminum foils. The thickness of the samples was determined used a Profilometer (Dektak 3 ST). Samples prepared on silicon substrates were used for profilometry. The metal volume fraction or the metal filling factor was estimated using a combination of EDX and profilometry [74]. The microstructure of the nanocomposites was investigated using transmission electron microscopy (TEM). For TEM analysis the nanocomposites were prepared on carbon coated copper grids. TEM analysis was done using the machine Leo 906 (Zeiss, Oberkochen, Germany) at

80 kV. Surface conductivity properties of nanocomposites deposited on borosilicate glass substrates were studied using conductive atomic force microscopy (CAFM).

### 3.2.1 X-ray diffractometry (XRD)

The crystallography, physical properties and chemical composition of thin films can be studied using tools like grazing incidence X-ray diffractometry (GIXD). It is a non-destructive technique. GIXD is used to determine the phase, chemical composition, crystallographic properties and preferred orientation.

In X-ray diffractometry (XRD) characteristic X-rays hit a material, and the X-rays interact with the electrons of the atoms in the material. The deflected X-rays from different atomic planes interact with each other. If the atoms are arranged in a periodic fashion, like in a crystal, the X-rays interfere constructively resulting in a sharp intensity peak in the XRD pattern. The peaks (peak position and intensity) in an X-ray diffraction pattern are related to the crystal structure of the material. Consider a material with crystalline structure in which the atoms are arranged regularly as shown in Figure 3.10. The peak position is described by the Bragg equation.

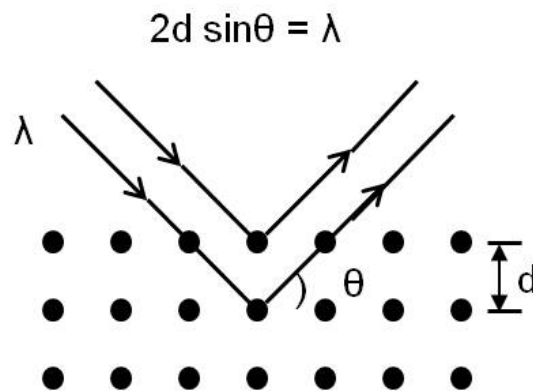


*Figure 3.10: Bragg's law depicting the condition for constructive interference in X-ray diffraction.*

When a monochromatic and parallel beam of X-rays are incident on the crystal the deflected rays from the atoms interfere either constructively or destructively. X-ray diffraction occurs when constructive interference takes place and when the following condition is satisfied

$$2d \sin \theta = n \lambda \quad (3.2)$$

where ‘d’ is the distance between the lattice planes,  $\lambda$  is the wavelength of incident X-rays,  $\theta$  is the X-ray incidence angle and ‘n’ is an integer.

Diffraction occurs only when the distance travelled by the reflected rays from successive planes differ by ‘n’ number of wavelengths. By varying the angle  $\theta$  and plotting the angular positions against the intensities of the diffraction peaks an X-ray diffraction pattern is produced, which is a characteristic of the crystal lattice of the sample. The XRD pattern of a crystalline material is its own fingerprint because it differs from the pattern of every other crystalline material.

The width of the peak in the XRD pattern can be used to determine the average crystallite size. Normally crystallite size is calculated using the Scherrer’s equation.

$$L = k\lambda/B\cos\theta \quad (3.3)$$

where ‘L’ is the crystallite size, ‘K’ is the crystallite-shape factor,  $\lambda$  is the X-ray wavelength,  $\theta$  is Bragg’s angle and ‘B’ is full width at half maximum (FWHM).

### **Grazing incidence X-ray diffractometry (GIXD)**

XRD of thin films possess the problem of weak diffraction intensities due to the smallness of the diffraction volume. It can be increased by decreasing the angle of incidence which can be achieved using GIXD. GIXD is schematically illustrated in Figure 3.11 [75] in which the optical path is depicted.

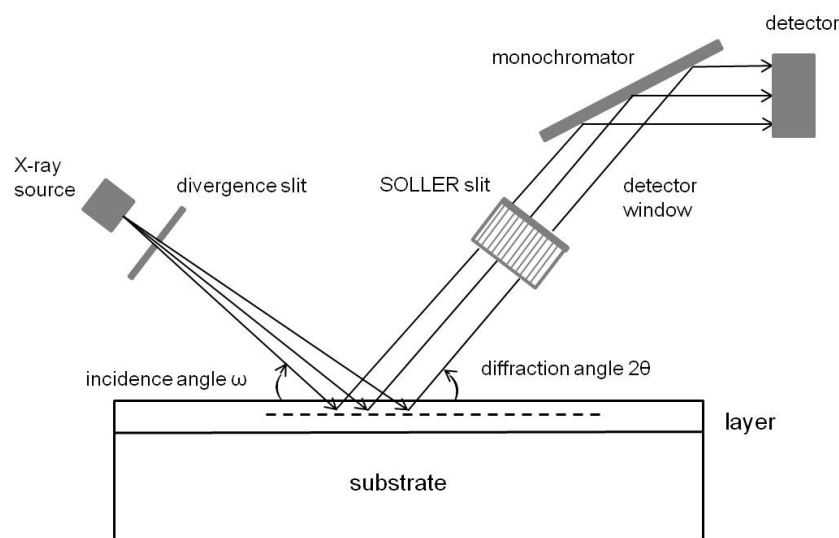


**Figure 3.11:** Schematic diagram of grazing incidence X-ray diffractometry (GIXD) [75].



### 3.2.2 X-ray photoelectron spectroscopy (XPS)

X-ray photoelectron spectroscopy (XPS) is a powerful and sensitive spectroscopic technique used to study the elemental and chemical composition on the surface of materials. XPS is also known as electron spectroscopy for chemical analysis (ESCA) and was developed for the first time by Kai Siegbahn [76]. Surface analysis is performed using XPS by irradiating the sample with monoenergetic soft X-rays and by analysing the energy of the emitted electrons [77]. XPS is based on the photoelectric effect in which the incident photons interact with the atoms on the sample surface causing electrons to be emitted. The energy of the emitted electron can be written as

$$E_{K.E} = h\nu - E_{B.E} - \phi_s \quad (3.4)$$

where  $\nu$  is the photon energy,  $E_{B.E}$  is the binding energy of the atomic orbital from which the electron originates and  $\phi_s$  is the spectrometer work function.

Each element has a unique set of binding energies. Thus, XPS can be used to identify the elements present on the sample surface. The binding energies can vary causing ‘chemical shifts’. This occurs because of the difference in the chemical potential and polarizability of compounds [77]. The chemical state of the material can be analysed using these chemical shifts.

The mean free path of electrons in solids is very small. Thus, the detected electrons in XPS originate from the top few nm ( $\sim 10$  nm) of the sample surface. This makes XPS a surface sensitive technique for chemical composition analysis. The detected electrons which originate from the surface produce the peaks in the XPS spectra. The XPS spectra are plotted such that the Fermi level corresponds to zero binding energy.

#### Quantitative analysis using XPS

The relative concentration of the various constituents can be determined from peak heights and peak areas. If a sample that is homogeneous in the analysis volume is considered, the number of photoelectrons per second in a specific peak is given as [77]:

$$I = n f \sigma \theta y \lambda A T \quad (3.5)$$

where ‘n’ is the number of atoms of the element per  $\text{cm}^3$  of the sample, ‘f’ is the X-ray flux in photons/ $\text{cm}^2\text{-s}$ ,  $\sigma$  is the photoelectric cross section for the atomic orbital of interest in  $\text{cm}^2$ ,  $\theta$  is the angular efficiency factor for the instrumental arrangement based on the angle between the photon path and detected electron, ‘y’ is the efficiency

in the photoelectric process for formation of photoelectrons of the normal photoelectron energy,  $\lambda$  is the mean free path of the photoelectrons in the sample, 'A' is the area of the sample from which photoelectrons are detected and 'T' is the detection efficiency for electrons emitted from the sample. From equation 3.5 we can write

$$n = I/f\sigma\theta y\lambda AT \quad (3.6)$$

Let the denominator be defined as atomic sensitivity factor S. The relative concentrations between two elements can be written as

$$n_1/n_2 = (I_1/S_1)/(I_2/S_2) \quad (3.7)$$

Similarly the atomic fraction of any element 'x' in a sample,  $C_x$  can be written as

$$C_x = n_x/\Sigma n_i = (I_x/S_x)/\Sigma(I_i/S_i) \quad (3.8)$$

The value of S is based on empirical data.

XPS measurements are performed to investigate the chemical bonding nature and the elements present on the surface of the sample (except hydrogen). The analysis by XPS is restricted to depths of some nanometers. XPS is not able to detect hydrogen. In this work XPS analysis was performed using X-ray photoelectron spectrophotometer Axis Ultra, Kratos, Manchester, GB equipped with an X-ray source monochromator. Axis Ultra provides a high energy resolution capability for both conductive and insulating samples through the incorporation of a charge neutralisation system. A photograph showing the XPS machine is shown in Figure 3.12. For the excitation of the photoelectron spectra Al  $K\alpha$  ( $h\nu = 1.4867$  keV) was used. Spectra were recorded using an electron take-off angle of  $90^\circ$  relative to the sample surface. Charge neutralization was used for all samples. The analyzed spot size was  $\sim 300 \mu\text{m}^2$ . Two sets of measurements were performed. Wide scans and individual photoelectron lines were acquired using the X-ray source operating at a power of 150 W and an analyzer pass energy of 80 eV. Moreover high resolution measurements of the C  $1s$ , Si  $2p$ , N  $1s$  and Co  $2p$  regions with a pass energy of 10 eV at a power of 225 W were performed. Casa XPS 2.3.29 software was used for the XPS analysis. All spectra were referenced to the aliphatic carbon at binding energy (BE) of 285.0 eV. The error can be estimated to be around 5%.

For X-ray photoelectron spectroscopy (XPS) analysis samples prepared on teflon substrates were used. Teflon is not a common substrate for XPS analysis. But the samples prepared on teflon substrates were used in the another experimental technique

of X-ray absorption spectroscopy (XAS) complementary to XPS. In order to minimize the errors in analysis arising from different substrates the same samples prepared on teflon substrates were used for XPS analysis.



*Figure 3.12: Photograph showing the XPS machine used to analyse the Co–pp HDMSN nanocomposites.*

### 3.2.3 Fourier transform infrared spectroscopy (FTIR)

Fourier transform infrared spectra (FTIR) of the nanocomposites films prepared on aluminum foil were taken using Perkin Elmer spectrometer in attenuated total reflection (ATR) mode. The ATR-FTIR spectroscopy was used to investigate the bonding nature of the nanocomposites. All FTIR spectra were smoothed and baseline corrected.

FTIR spectroscopy is based on the principle that almost all molecules absorb infrared radiation. IR spectroscopy is a quick and relatively cheap analytical technique. Moreover, the IR spectrum of a given compound is unique. The IR spectrum can serve as a fingerprint for this compound. In IR spectroscopy the sample is exposed to IR radiation. Absorption occurs when the IR radiation matches the energy of a specific molecular vibration. The absorption of the sample varies as a function of the energy of input IR radiation. The wavenumber is proportional to energy. The IR absorption spectrum is plotted as a function of the wavenumber. The shapes and wavenumbers of

the peaks give useful information about the functional groups and chemical structure of the material. The infrared region of the electromagnetic spectrum extends from  $14,000\text{ cm}^{-1}$  to  $10\text{ cm}^{-1}$ . The region of interest for studying the functional groups is the mid IR range, i.e.  $4000\text{ cm}^{-1}$  to  $400\text{ cm}^{-1}$ .

The theory of infrared radiation is based on the principle of molecular vibrations [78]. At the temperature above absolute zero, all the molecules are in a state of vibration. When the frequency of the incident IR radiation matches that of the molecular vibrations the molecule absorbs the radiation. A polyatomic molecule with 'n' atoms has '3n-6' degrees of fundamental vibrations, i.e. vibrations other than translational and rotational modes. There are two types of molecular vibrations: stretching and bending. As an example the fundamental vibrations of  $\text{CH}_2$  group are depicted in Figure 3.13 [79]. Not every possible vibration in a molecule results in an absorption band in the IR spectrum. For the molecule to be active in the IR region, atleast one vibrational motion must alter the net dipole moment of the molecule. Then the absorption of the molecule can be observed in the IR spectrum. The interpretation of the IR spectra is based on correlation charts and tables of infrared data.

#### **Attenuated total reflection (ATR-FTIR spectroscopy)**

The reflection technique of ATR-FTIR has been used during the FTIR analysis of the Co – ppHMDSN samples. Figure 3.14 depicts the ATR technique. In the ATR technique an ATR crystal is in contact with the sample. It is an optically dense crystal with high refractive index. The infrared beam incident on the ATR crystal reflects via total internal reflection. The IR light is introduced into the crystal at an angle greater than the critical angle so that total internal reflection takes place. The sample is in close contact with the ATR crystal. The evanescent wave from the total internal reflection extends beyond the surface of the crystal into the sample which is in contact with the crystal. This evanescent wave protrudes only a few microns (maximum  $5\text{ }\mu\text{m}$ ) into the sample. This means that ATR technique requires good contact between the crystal and the sample. The sample absorbs the evanescent IR radiation at specific wavenumbers corresponding to the chemical structure of the sample. The altered evanescent wave is passed to the detector which generates an IR spectrum. For the ATR-FTIR technique to be successful it is important that a) there must be a good contact between the sample and the crystal and b) the refractive index of the crystal must be greater than that of the sample so that total internal reflectance occurs.

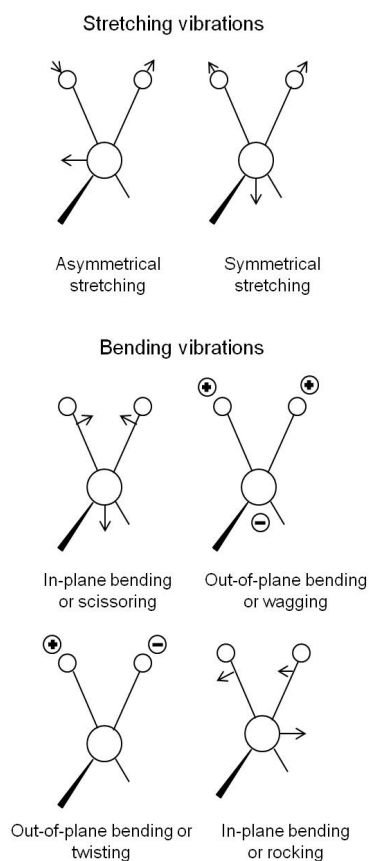


**Figure 3.13:** Fundamental vibrational modes for a nonlinear  $\text{CH}_2$  group (+ indicates motion out of the plane of paper, - indicates motion into the plane of paper) [79].

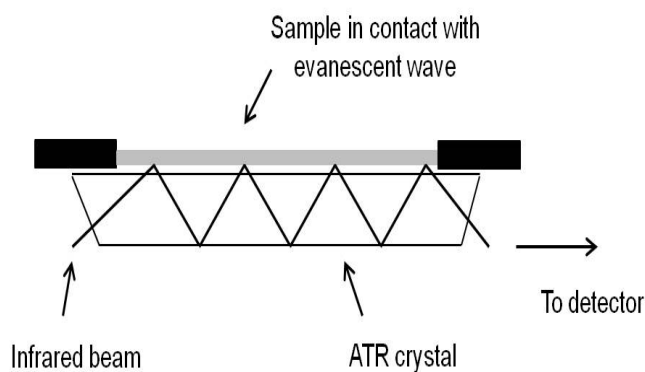


**Figure 3.14:** Principle of operation of attenuated total reflection technique [80].

### 3.2.4 UV-Vis spectroscopy

Ultraviolet-visible spectroscopy (UV-Vis spectroscopy) is an analytical technique used to study the chemical structure of materials. UV-Vis spectroscopy utilises the ultraviolet (UV) and visible (Vis) range of electromagnetic spectrum. When UV-Vis light is incident on a material, absorption takes place, and the electrons in the atoms and molecules of the material are excited to higher energy states. As the absorption of the UV-Vis radiation is dependent on the molecular structure, the UV-Vis absorption spectra can be used to qualitatively identify atom and molecular species.

When a light radiation of intensity  $I_0$  is incident on a transparent solution the transmitted light intensity 'I' can be written according to Beer's law as:

$$A = -\log(I/I_0) = \epsilon_{\lambda}bc \quad (3.9)$$

where 'A' is the absorbance, 'b' is the cell path length in cm, 'c' is the concentration of solution in mol/l and  $\epsilon_{\lambda}$  is the molar absorption coefficient in l/mol/cm.  $\epsilon_{\lambda}$  is dependent on the wavelength.

In UV-Vis spectroscopy the sample is irradiated with a sweeping range of frequencies in the UV-Vis range. UV-Vis spectra are plotted as absorbance versus wavelength. The absorption spectrum shows absorption bands which correspond to structural groups within the molecule.

### 3.2.5 Electron microscopy

Electron microscopy was used to characterize the prepared nanocomposites. An electron microscope utilises a beam of high energy electrons to image a specimen and to gain information about structure and composition. A stream of electrons is accelerated onto the specimen resulting in interactions between the electrons and the atoms in the specimen. These interactions are detected and transformed to an image. The two types of electron microscopes used in this work are:

1. Scanning electron microscope
2. Transmission electron microscope

A brief description about the operation and working of both instruments is presented below.

### 3.2.5.1 Scanning electron microscopy (SEM)/Energy dispersive X-ray spectroscopy (EDX)

Scanning electron microscope (SEM) works on the principle of scanning a finely focused beam of electrons with energies of 1–20 keV onto a sample. The various signals that are produced from the sample interaction are used to analyze the sample. Energy dispersive X-ray spectroscopy (EDX) is an analytical technique to analyze the elemental concentration in a specimen. When a sample is bombarded with a high energy electron beam the beam interacts with the sample. The electron beam incident on the sample undergoes two types of scattering: elastic and inelastic. During elastic scattering only the trajectory of the electron changes and its kinetic energy and velocity remain constant. During inelastic scattering the incident electron interacts with the atoms in the sample. This interaction causes displacement of electrons from the orbits of the atoms and thus the atoms get excited. The interaction of the electrons with the specimen results in a range of signals. The different types of signals produced during the interaction of the electron beam with the specimen is schematically illustrated in Figure 3.15.

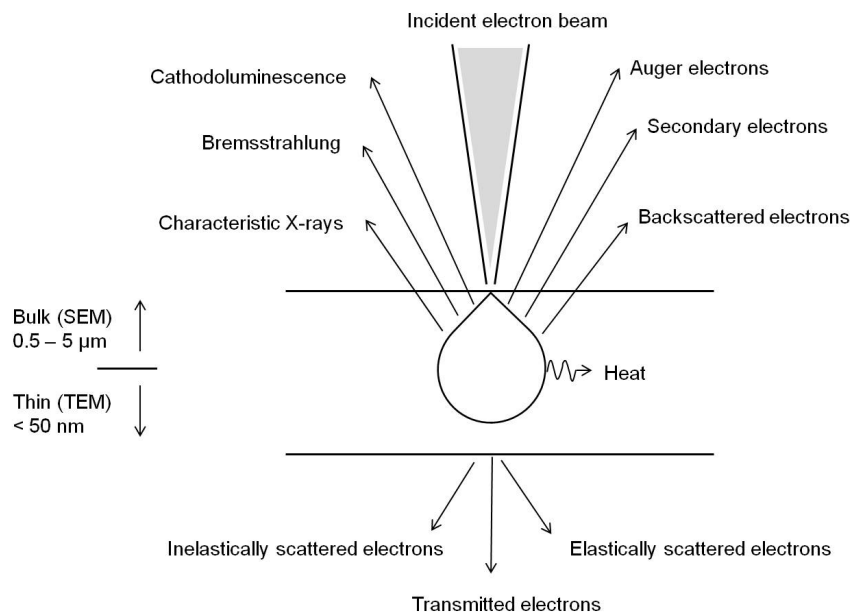


**Figure 3.15:** Schematic illustration of various signals produced when an electron beam interacts with a specimen [81].

For EDX/SEM analysis the interactions (signals) depicted on the top in Figure 3.15 are utilized while examining bulk or thick specimens. The signals on the bottom of Figure 3.15 are used for examining thin specimens using TEM. Secondary electrons pro-

vide topographical image of sample surface. X-rays provide information about elemental composition of the sample.

When the excited atoms return to the ground state the atom gives away the excess energy as X-rays, cathodoluminescence and Auger electrons. The EDX X-ray detector measures the intensity of X-rays versus their energy. The energy of the X-ray is the fingerprint of each element. When the electron beam interacts with the atoms in the sample two types of X-rays are produced:

1. Characteristic X-rays are produced when the beam electrons eject inner shell electrons of the atoms in the sample.
2. Continuum X-rays or Bremsstrahlung are produced when the beam electrons interact with the nucleus of the atoms in the sample.

A schematic description of the construction of SEM is shown in Figure 3.16. The virtual source represents the source of electron beam (electron gun) which is accelerated down the column. The lenses are used to control the diameter of the beam and to focus the beam on the specimen. Apertures are used to construct the beam and to eliminate high angle electrons. The scan coils are used to scan or sweep the beam in a raster mode. The whole system is maintained at high vacuum level.

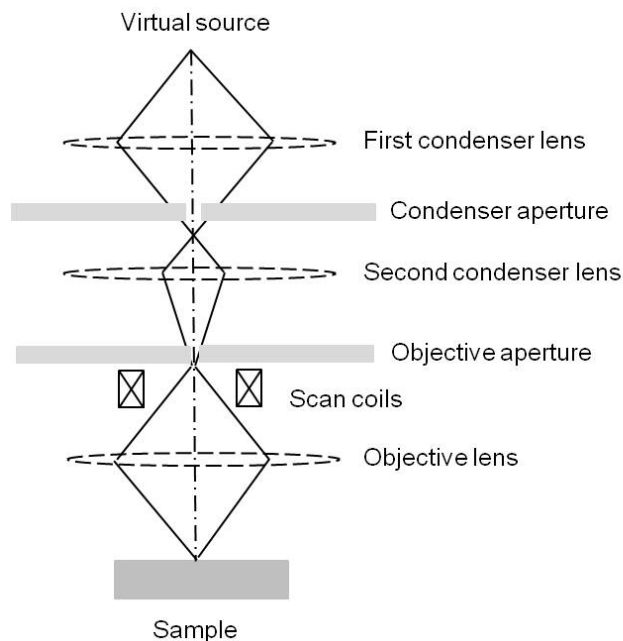


*Figure 3.16: Schematic illustration of the construction of an SEM machine [82].*



When the electron beam strikes the sample interactions occur within the sample and the various signals (as shown in Figure 3.15) are detected using detectors. One of the uses of SEM is acquiring chemical composition information using EDX. The X-rays produced during the interaction of electron beam with the sample are detected using the energy dispersive X-ray detector (EDX). The EDX detector separates the characteristic X-rays of different elements into an energy spectrum. A spectrum of the histogram of X-ray intensities versus the X-ray energy is plotted.

EDX systems are usually integrated into an SEM. An EDX detector contains a crystal. When incoming X-rays are absorbed by the crystal ionization takes place and free electrons are produced. These free electrons produce an electrical charge bias. Thus the energy of the individual X-rays is converted into electrical voltage pulses or counts of proportional size. A typical EDX spectrum is a plot of X-ray counts versus X-ray energy. The energy peaks correspond to various elements in the sample. The qualitative analysis of the elements involves identification of lines in the spectrum. The quantitative analysis, i.e. determination of the concentration of the elements present involves measuring line intensities of each element. In addition to the characteristic X-ray lines electron bombardment of the sample also gives rise to continuous X-ray spectrum. This continuous spectrum contributes to the 'background' upon which characteristic elemental lines are superimposed.

EDX in combination with profilometry helps in estimating the metal volume fraction or metal filling factor of the nanocomposites. For this, in addition to the nanocomposite, a uniform cobalt standard thin film was prepared under the same conditions as the nanocomposite. The intensity (cps) of the cobalt line in both the nanocomposite and the standard thin films was measured using EDX. Additionally, thicknesses of both the films were measured. The fraction of cobalt in the nanocomposite was determined from the ratio of intensities of the nanocomposite to the standard. Furthermore, the effective thickness of cobalt in the nanocomposite was evaluated by multiplying the fraction of cobalt in the nanocomposite with the thickness of the standard film. Finally, the metal filling factor was estimated from the ratio of effective thickness of cobalt in the nanocomposite to the thickness of nanocomposite [74].

### 3.2.5.2 Transmission electron microscopy (TEM)

Transmission electron microscopy (TEM) is a versatile and sophisticated technique used to provide topographical, morphological, compositional and crystalline information. TEM usually employs an electron beam accelerated at a voltage of 100–400 kV. For a TEM analysis the electrons need to penetrate the specimen. Therefore, it must be very thin ( $< 50$  nm). When a thin specimen is irradiated with an electron beam various signals are produced (see Figure 3.15). The fraction of the incident beam which passes through the thin specimen is studied in TEM. The signals which are utilized in TEM are unscattered electrons (transmitted beam) and elastically scattered electrons (diffracted beam).

The basic layout and the optics of TEM is schematically depicted in Figure 3.17.

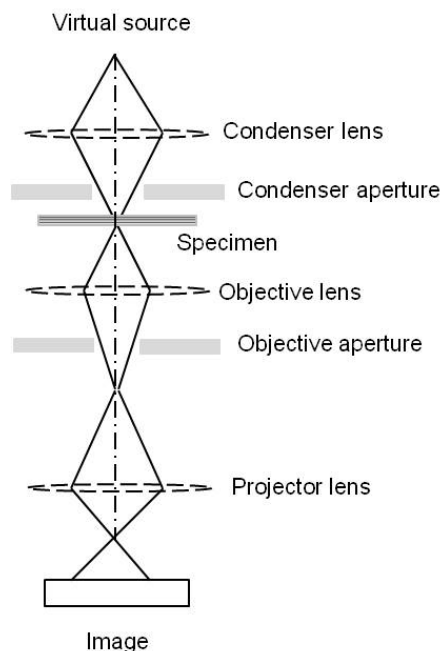


*Figure 3.17: Schematic illustration of layout and optics in TEM [83].*

TEM consists of a source of electron beam, a series of lenses, the specimen and the imaging system. The condenser lenses are used to focus the illuminating beam onto the specimen. When the electron beam hits the specimen a part of it is transmitted. The transmitted beam is focused on the objective lens which is used to produce the magnified image of the illuminated area. The projector lenses are used to provide further magnification of the image. Apertures are used at various stages to restrict the beam and also to block out high angle electrons. The image is observed on a fluorescent screen or

captured using a digital camera. The transmitted electrons hit a fluorescent screen and emit light. In modern instruments, an electronic imaging device such as CCD (charge-coupled device) camera is used. The whole system is maintained under high vacuum conditions.

Different types of images can be obtained using TEM by using the different apertures and the various signals from the specimen. A bright field image is obtained when the unscattered transmitted beam is selected whereas a dark field image is obtained when the diffracted beam is selected. Fewer transmitted unscattered electrons pass through thicker or denser areas of the specimen. Consequently such areas appear darker in the TEM image. Thinner or less denser areas have less transmitted unscattered electrons. They appear brighter in the TEM image. In the present work cobalt–ppHMDSN nanocomposites were investigated using TEM. As the metal nanoparticles are denser when compared to the polymer they appear as darker spots in the TEM image. The polymer appears lighter in colour.

### 3.2.6 Atomic force microscopy (AFM)

Atomic force microscopy (AFM) is a technique used for the surface characterization of the specimen at macroscopic level. The principle operation of AFM is depicted in Figure 3.18. A very fine sharp tip is brought into contact or into close proximity of the specimen being imaged. The length of the tip is a few microns and the diameter is around 100 Å. The tip is located at the free end of a cantilever that is 100–200  $\mu\text{m}$  long. The interactive force between the tip and the cantilever causes the cantilever to bend or deflect. The tip deflects as the cantilever is scanned across the sample surface. This deflection is measured using a detector, and a surface topography image is generated. AFM can be used to study conductors, insulators and semiconductors. A piezo electric scanner is used to scan the tip with respect to the sample or the sample with respect to the tip. A split photo diode is used as a detector. A laser beam reflected off from the back of the cantilever is used to monitor the tip-sample interaction. The difference of the photo detector output voltage is used to map the surface topography of the sample. There are three common modes of operating an AFM: contact mode, non-contact mode and tapping mode. They are depicted in Figure 3.19.

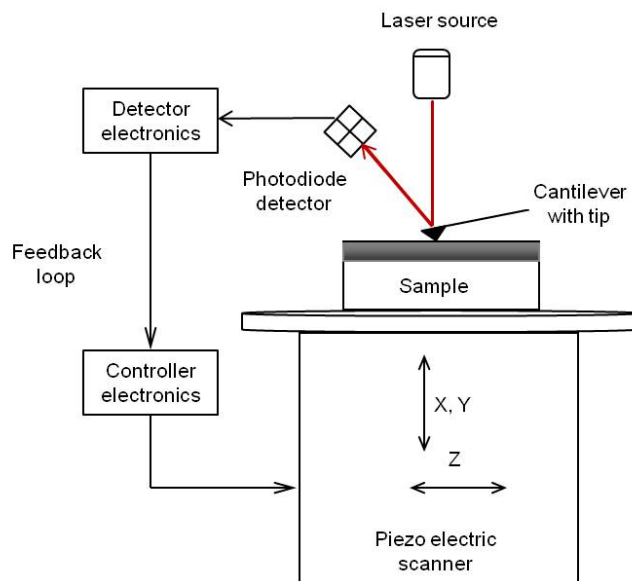


*Figure 3.18: Schematic illustration depicting operation of AFM [84].*

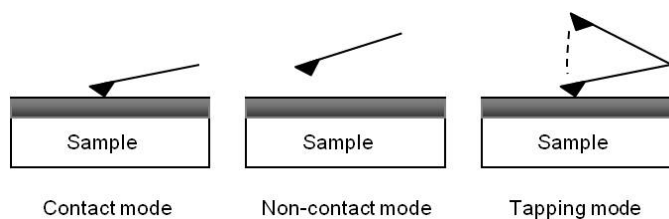


*Figure 3.19: Different modes of AFM operation.*

In contact mode of operation the tip is in touch with the sample surface. In this regime the force between the tip and sample is repulsive. There are two modes of operation in contact mode: constant force and constant height modes. In constant force mode the tip is scanned across the sample while a feedback loop maintains a constant cantilever deflection by vertically moving the scanner. The distance moved by the scanner at each  $x, y$  data point is used to map the topography of the sample surface. In constant height mode the relative height between the tip and the sample is maintained constant. The variations in the signal of the photo detector is used to generate the topography signal.

In non-contact mode the cantilever is oscillated close to its resonant frequency, and the tip of the cantilever does not touch the sample surface. Due to the van der Waals attraction force between the tip and the sample the frequency of the cantilever changes. The feedback loop monitors the changes and controls the tip-to-sample distance

which in turn generates the surface topography. Tapping mode of operation is similar to non-contact mode, but the tip lightly ‘taps’ the sample surface during scanning. Using tapping mode the influence of friction, adhesion and electrostatic forces is minimized.

### 3.2.6.1 Conductive atomic force microscopy (CAFM)

Conductive atomic force microscopy (AFM) was operated in contact mode to study the topography and surface conductivity [85] of the nanocomposites prepared on borosilicate glass. Nanocomposite films prepared on borosilicate glass were used for conductive atomic force microscopy (CAFM) analysis. The AFM images were taken using a Veeco DI CP II instrument. Commercial AFM cantilevers (SCM-PIC) which are made of n-doped Si and coated with Pt/Ir are used. The length of the cantilever is maximum  $495\ \mu\text{m}$  with a spring constant of  $0.2\ \text{N/m}$  and a resonant frequency of  $10\text{--}16\ \text{kHz}$ . The radius of curvature of the tip is not more than  $25\ \text{nm}$ . A schematic describing the experimental setup used in conductive atomic force microscopy (CAFM) is shown in Figure 3.20. An electrical connection is established between the surface of the nanocomposites and the top of the piezo scanner by using a silver paint. Silver paint acts as one electrode to which a DC bias voltage is applied and the cantilever tip as the second electrode which is grounded. The feedback signal from the scanner is used to measure topography whereas the current passing between the sample and the tip generates the conductivity image. The conductivity image is passed through a pre-amplifier. The whole setup is controlled using an AFM electronics controller. In this work conductivity and topography images were obtained simultaneously for the Co–ppHMDSN nanocomposite thin film with 34% metal filling factor.

### 3.2.7 Three electrode electrochemical cell

In a three electrode electrochemical cell, a potential is applied to the electrodes which causes an electrochemical reaction to take place. The reaction results in the flow of current due to the applied potential. A three electrode cell consists of a working electrode (WE), a reference electrode (RE), and an auxiliary(or counter) electrode(AE). WE is the electrode under study and to this electrode the potential is applied. The electrochemical reactions of oxidation or reduction occur at the WE. RE is used as the reference for the electrochemical potential applied to the WE. RE holds a constant potential during the electrochemical process. There are several commonly used reference electrodes such as silver/silver chloride (Ag/AgCl), saturated calomel electrode (SCE). The AE carries the

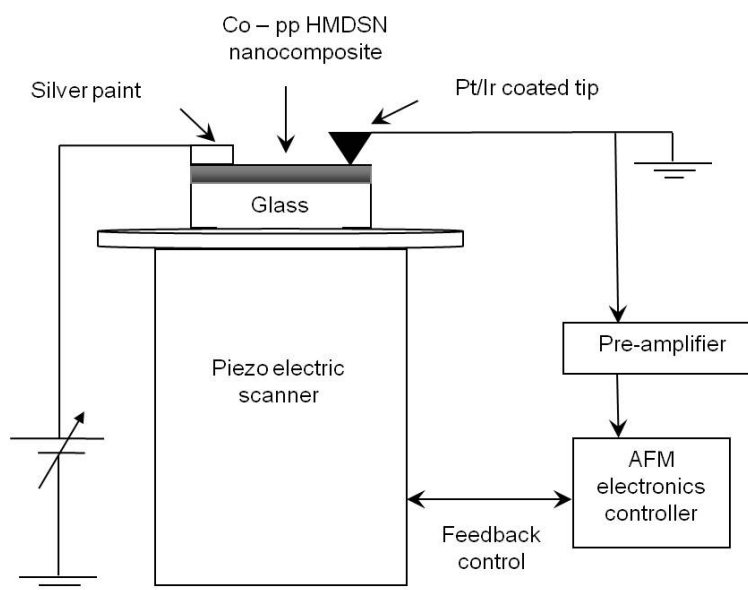


**Figure 3.20:** Schematic of experimental set-up for conductive atomic force microscopy (CAFM) to map surface conductivity of cobalt-plasma polymerized HMDSN nanocomposite thin films.

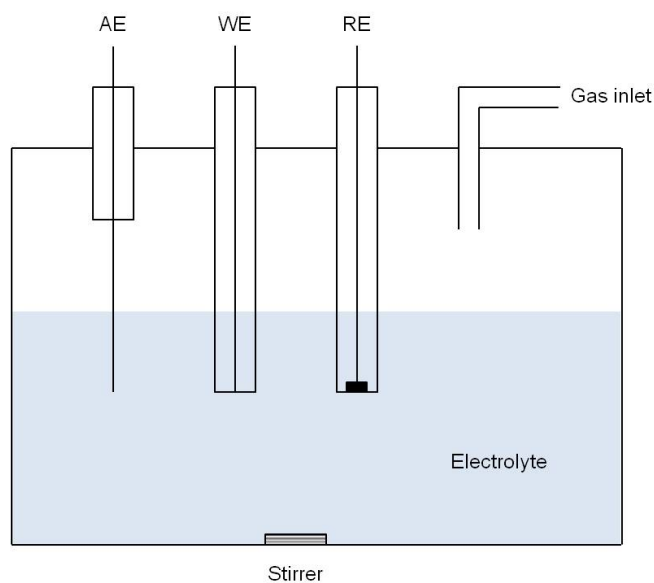


**Figure 3.21:** Schematic representation of a typical three electrode electrochemical cell. AE: Auxiliary electrode, WE: Working electrode, RE: Reference electrode [86].

bulk of the current. It completes the current path by serving as a current source/sink. Usually inert materials like graphite or platinum are used as auxiliary electrodes. All the three electrodes are connected in a circuit with precise control of the potential applied to the WE. The whole set up is called a potentiostat. Figure 3.21 depicts the schematic of a typical three electrode electrochemical cell.

### 3.2.8 X-ray absorption spectroscopy

X-ray absorption spectroscopy (XAS) is a non-destructive, element-specific technique. It can be used to study at the atomic level which makes it suitable for use even for materials with amorphous structure. XAS study was carried out to investigate the local chemical environment around cobalt. In particular, XANES was used to find out the oxidation state of cobalt. EXAFS is useful for amorphous materials and nanocomposites with small metal particles [87]. For the XAS analysis Co–ppHMDSN nanocomposites were prepared on teflon substrates. Teflon is made up of low atomic weight elements, and using teflon substrates would not influence the X-ray absorption of the heavier cobalt atoms. XAS studies on Co K-edge at an edge energy of 7700 eV was performed at the synchrotron radiation facility BESSY II in Berlin. Beamline KMC 2 was used for this purpose. The synchrotron source D92 was running at a minimal energy of 1.7 GeV with an average flux of 107–1010 photons/s/100mA. The beamline KMC 2 provides experimental setup for EXAFS and XANES measurements in the energy range of 5 keV–14 keV [88]. The beam intensity was stabilised using electronics with an accuracy of 0.3%. A double crystal monochromator with two SiGe 111 graded crystals was used. The detector system consisted of three ionization chambers, a Si-PIN photodiode for fluorescence measurements, a scintillation counter and an energy-dispersive detector (Roente X-Flash) [88]. The top view of BESSY synchrotron radiation source in Berlin is shown in Figure 3.22.

Co–ppHMDSN nanocomposites were prepared on teflon substrates of size  $\sim 1$  x 1 cm. XAS measurements were performed in fluorescence mode because of the low concentration of cobalt. The teflon substrates were attached to the sample holder using a double sided tape. The position of the sample holder was adjusted using an X-Y-Z,  $\theta$ – $2\theta$  goniometer such that the X-ray beam hits the center of the teflon substrate. This makes sure that the XAS measurements are performed on all samples at the same place.



*Figure 3.22: Top view of BESSY synchrotron radiation source in Berlin.*

### 3.2.8.1 Analysis software

The measured XAS spectra were analysed using freely available software ATHENA from the IFEFFIT 1.2.11 program [89, 90]. IFEFFIT is an interactive program for XAS analysis. It uses the analysis algorithms AUTOBK and FEFFIT. The AUTOBK algorithm was used for background removal. FEFFIT algorithm was used for fitting EXAFS function  $\chi(k)$ . ATHENA was used for XAS data processing and analysis.



# 4 Cobalt – plasma polymerized HMDSN nanocomposites

Cobalt/cobalt oxide – polymer nanocomposites have been suggested for potential applications such as NO<sub>x</sub> sensors [91], magnetic nanostructures [92], anti corrosion [33] and catalysis [2]. Various methods such as sol–gel [13, 36], co-sputtering [91, 93], pulsed laser deposition [94] and dual plasma process [95] have been used to prepare cobalt – polymer nanocomposites. In this work cobalt sputtering and simultaneous plasma polymerization of the monomer HMDSN was employed aiming at a new cobalt – polymer nanocomposite system. The prepared Co – pp HMDSN nanocomposites were investigated using various analytical techniques.

## 4.1 Structural investigations

### 4.1.1 Estimation of metal filling factor from EDX and profilometry

The metal filling factor of the nanocomposites was estimated using a combination of EDX and profilometry [74]. A standard cobalt sample was taken as reference. In order to estimate the metal filling factor of the nanocomposite, the nanocomposite and standard were prepared under the same plasma conditions. The thicknesses of both the samples were measured using a profilometer. The value of intensity of cobalt line (in counts/s) in both nanocomposite and standard was measured using EDX. As an example,

Thickness of Co – pp HMDSN nanocomposite film = 90 nm

Thickness of cobalt standard film = 40 nm

Intensity of cobalt line in nanocomposite (from EDX) = 1167 cps

Intensity of cobalt line in standard (from EDX) = 1545 cps

Hence, the fraction of cobalt in nanocomposite

$$\begin{aligned} &= \text{Intensity of cobalt line in nanocomposite} / \text{Intensity of cobalt line in standard} \\ &= 1167/1545 = 0.76 \end{aligned}$$

$$\begin{aligned} &\text{Therefore, the effective thickness of cobalt in nanocomposite} \\ &= \text{fraction of cobalt in nanocomposite} * \text{thickness of standard} \\ &= 0.76 * 40 \\ &= 30.4 \end{aligned}$$

Metal filling factor of nanocomposite

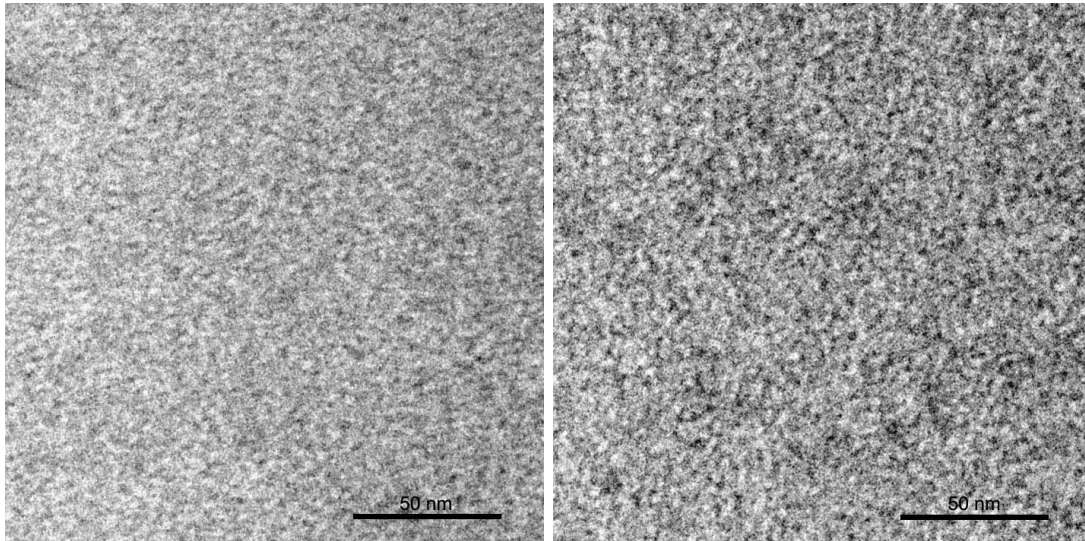
$$\begin{aligned} &= (\text{effective thickness of cobalt in nanocomposite} / \text{thickness of nanocomposite}) * 100 \\ &= (30.4 / 90) * 100 \\ &= 34 \% \end{aligned}$$

The metal filling factors of the prepared nanocomposites was estimated in this manner. In this work Co–ppHMDSN nanocomposites with 4%, 17%, 25% and 34% metal filling factors were prepared.

#### 4.1.2 Structure and microstructure analysis using TEM and XRD

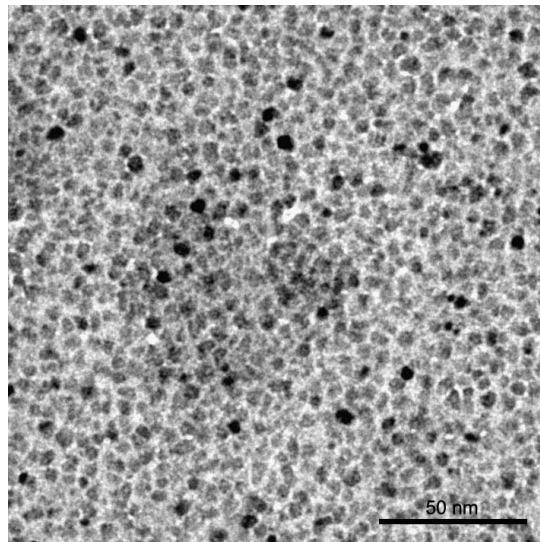
Cobalt – pp HMDSN nanocomposites prepared on carbon coated copper grids were analysed using transmission electron microscopy (TEM). The thickness of the films was ~20–40 nm. The morphology of the nanocomposites was studied using TEM which gives information about the microstructure. The morphology and microstructure of the nanocomposites play an important role in various applications.

Co–ppHMDSN nanocomposites with four different metal filling factors of 4%, 17%, 25% and 34% were prepared. Figure 4.1 shows the TEM micrographs of the Co–ppHMDSN nanocomposites at three different filling factors. The size, shape, crystallinity and distribution of the nanoparticles vary with the filling factor. At lower filling factors the microstructure consists of amorphous nanoparticles whereas at higher filling factors crystalline nanoparticles were observed. The TEM micrographs of nanocomposites with filling factors of 17% and 25% depict nanoparticles of very small size (~2–3 nm). The amorphous and very low distribution is clearly seen. A slight increase in the number of nanoparticles can be seen in the nanocomposite at 25% metal filling factor which appears as more dark spots in the micrograph. Nanocomposite at 34% metal filling factor contains nanoparticles of size ~6 nm homogeneously distributed in the polymer matrix as indicated by Figure 4.1(c) and the histogram shown in Figure 4.2. The average size is in close agreement with the domain size calculated from the XRD pattern of the nanocomposite. XRD patterns of nanocomposites at 25% and 34%



(a) 17% metal filling factor

(b) 25% metal filling factor



(c) 34% metal filling factor

**Figure 4.1:** TEM micrographs of cobalt–plasma polymerized HMDSN nanocomposites with varying metal filling factors: a) 17%, b) 25%, c) 34%.

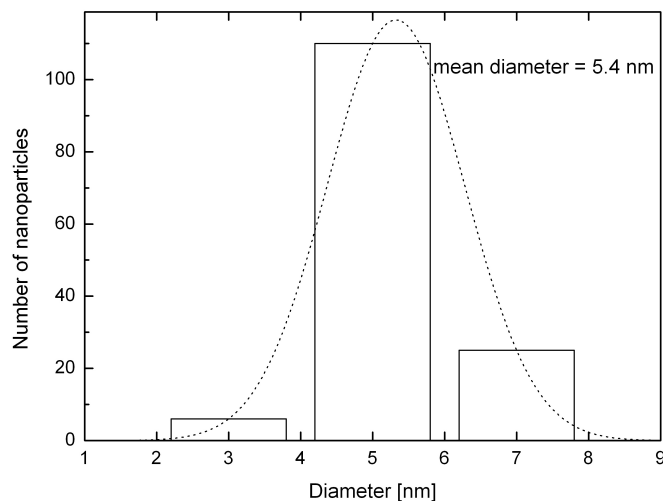


**Figure 4.2:** Histogram of size distribution of nanoparticles of cobalt – plasma polymerized HMDSN nanocomposite at 34% metal filling factor with a Gaussian fitting (line).

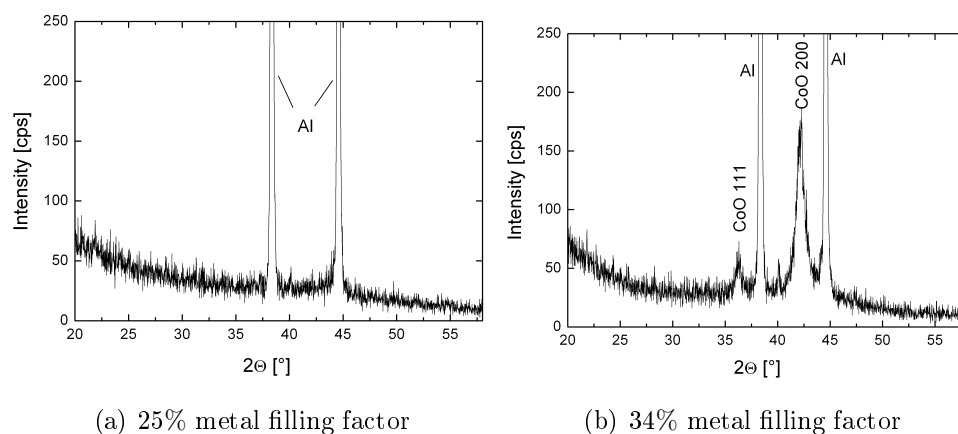


**Figure 4.3:** Grazing incidence XRD patterns ( $\omega = 0.5^\circ$ ) of cobalt – plasma polymerized HMDSN nanocomposites at metal filling factors of a) 25%, b) 34%.

metal filling factors are shown in Figure 4.3. XRD pattern of nanocomposite at 25% metal filling factor shows no peak from cobalt reflecting the x-ray amorphous nature of the nanoparticles. The peaks only correspond to the aluminum substrate. The TEM micrograph of nanocomposite at 25% metal filling factor (Figure 4.1(b)) indicates nanoparticles  $\sim 2\text{--}3$  nm in size which is difficult to infer from the XRD pattern. Similar results were reported [96] indicating the presence of amorphous nanoparticles at lower metal

filling factors. The XRD pattern of nanocomposite at 34% metal filling factor depicts peaks from CoO in addition to the peaks from the aluminum substrate. The average domain sizes were calculated from the line profile of the diffraction peaks by Fourier analysis using the Warren Averbach method [75]. For nanocomposite at 34% metal filling factor the average domain size is estimated to be 6 nm which is in good agreement with the size obtained from the TEM micrograph. The presence of CoO indicates the influence of oxygen either from the atmosphere or from residual water vapor in the reaction chamber.

### 4.1.3 Compositional analysis using XPS and EDX

Figure 4.4 depicts the survey scan XPS spectrum of Co–ppHMDSN nanocomposites at various metal filling factors. The survey scan indicates that the surface of the nanocomposites contains cobalt, silicon, nitrogen, carbon and oxygen. Though there is no oxygen present in HMDSN, the peaks corresponding to oxygen might be because of the atmospheric attack or due to the influence of water vapor deposited on the walls of reaction chamber.

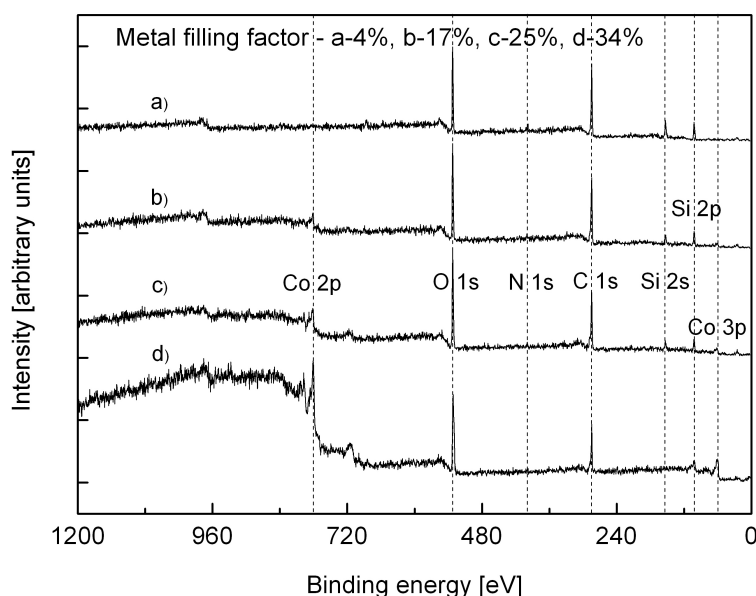


**Figure 4.4:** XPS survey spectra of cobalt–plasma polymerized HMDSN nanocomposites at various metal filling factors.

The percentage of elements detected on the surface of the samples analyzed by XPS is summarized in Table 4.1. As XPS is a surface sensitive technique the elemental

composition depicted in Table 4.1 corresponds to only the upper few nanometers of the nanocomposites. The elemental composition in the bulk is different from the surface.

**Table 4.1:** Elemental content of Co – pp HMDSN nanocomposites at various metal filling factors measured by XPS

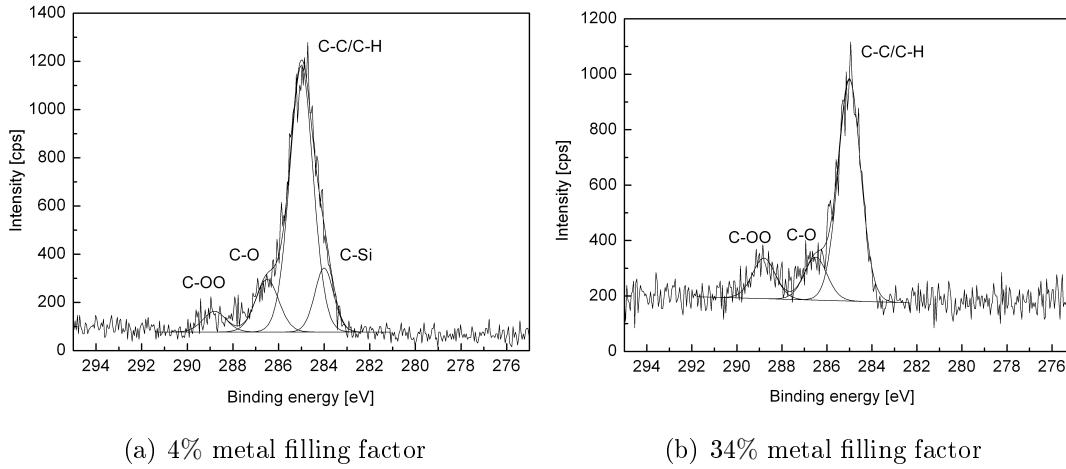
Filling factor	C - at%	N - at%	O - at%	Si - at%	Co - at%
4%	57	3	25.1	14	0.8
17%	56	2	29	8.3	4.2
25%	47	1.5	34	3	14
34%	41	1	38	0	20

Table 4.1 demonstrates an increase in the amount of cobalt and a decrease in the amount of silicon with increasing metal filling factor. Carbon is observed in the nanocomposites which can be attributed to the influence of atmospheric carbon and also from the methyl group of the HMDSN precursor. Nanocomposites at higher metal filling factors contain more oxygen. As more magnetron power was used to prepare nanocomposites at higher metal filling factors it results in more breaking of bonds and thus the presence of more number of unsaturated methyl bonds at higher metal filling factors. More number of such unsaturated bonds were attacked by more amount of atmospheric oxygen [97] which explains the increase in oxygen content at higher metal filling factors.

To study the various bindings further, highly resolved measured spectra of C 1s, Si 2p, N 1s and Co 2p<sub>3/2</sub> peaks were taken at six points on the Co – pp HMDSN nanocomposites. The highly resolved measured spectra of C 1s peak of Co – pp HMDSN nanocomposites at metal filling factors 4% and 34% are shown in Figure 4.5. They are studied in detail in order to understand the various bindings present on the surface of the samples.

Table 4.2 gives a summary of different bindings observed on the surface of the nanocomposites using XPS analysis. From the C 1s peak four compounds can be resolved: C–Si, C–C/C–H, C–O, and COO. The broad Si 2p signal was deconvoluted into two compounds: Si–C and Si–O. The peaks observed in the binding energy range of 101.0–103.7 eV in the highly resolved Si 2p signal indicates the presence of Si–C bonds [98]. From the Si 2p signal it can be inferred that Si–O bond is also one of the bonds in the plasma polymerized matrix. Although it is difficult to fit the N binding peak in the

Si  $2p$  signal the presence of a small amount of Si–N bonds cannot be excluded. This is because a small amount of



**Figure 4.5:** A typical highly resolved measured C  $1s$  spectrum of cobalt–plasma polymerized HMDSN nanocomposites at two different metal filling factors: a) 4%, b) 34%.

**Table 4.2:** Binding energies used to fit the C  $1s$ , Si  $2p$ , and Co  $2p_{3/2}$  high res peaks

S.No	Photoelectron line	Chemical bond	Binding energy (eV)	Reference
1	C $1s$	C–Si	283.8	[98]
2	C $1s$	C–C/C–H	285.0	[99]
3	C $1s$	C–O	286.5	[99]
4	C $1s$	COO	288.8	[99]
5	Si $2p$	Si–C	101.0	[100]
6	Si $2p$	Si–N	102.2	[100]
7	Si $2p$	Si–O	103.7	[100]
8	Co $2p_{3/2}$	Co	778.7	[101]

nitrogen was detected in the survey scan of the nanocomposites (Figure 4.4). Thus, the polymer matrix can be considered to be a mixture of bonds Si–C and Si–O.

The amount contributed by each bond to the total chemical composition of the polymer matrix can be analyzed from the high resolution peaks. Figure 4.6 gives a

summary of percentage of each binding in the C 1s and O 1s highly resolved peaks of Co–ppHMDSN nanocomposites at various metal filling factors. The bindings in C 1s peak depict that the number of C–Si bonds decreases with increasing metal filling factor. This is perhaps because of the breaking of C–Si bond with increasing power as higher power was used at higher metal filling factors. The bindings in O 1s peak indicate the presence of Co–O bonds in the nanocomposites. The number of Co–O bonds is less in nanocomposites at 4%, 17% and 25% metal filling factors. But the number of Co–O bonds is more in the nanocomposite at 34% metal filling factor. This confirms the presence of Co–O bonds as shown from XRD.

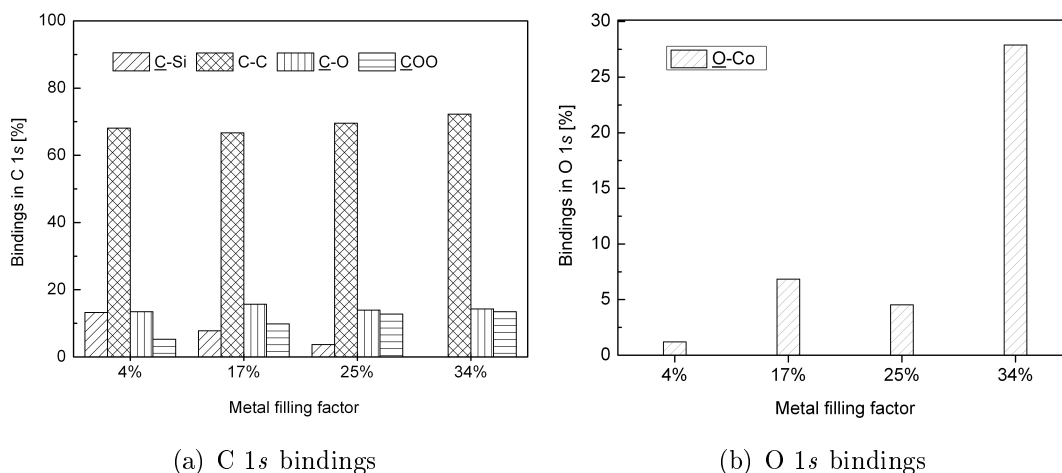


**Figure 4.6:** Summary of percentage of bindings of: a) C 1s and b) O 1s highly resolved peaks of cobalt–plasma polymerized HMDSN nanocomposites at various metal filling factors.

Figure 4.7 depicts the Co  $2p_{3/2}$  highly resolved peak of nanocomposite with 34% filling factor. The presence of both oxides and metallic cobalt is observed. A peak at  $\sim 780$  nm indicates the presence of CoO [41]. From XRD patterns of these nanocomposites (Figure 4.3) one cannot see the presence of any Co metal. But the XRD pattern of nanocomposite with 34% filling factor suggested the presence of crystalline cobalt oxide (CoO) nanoparticles. XPS spectra revealed the presence of Co metal and/or cobalt oxide while XRD patterns showed the presence of CoO only in the nanocomposite with 34% filling factor. This suggests that Co metal is in amorphous phase. The presence of metallic cobalt and CoO is also confirmed by the Fourier transform peaks from XAS (see Section 4.2).



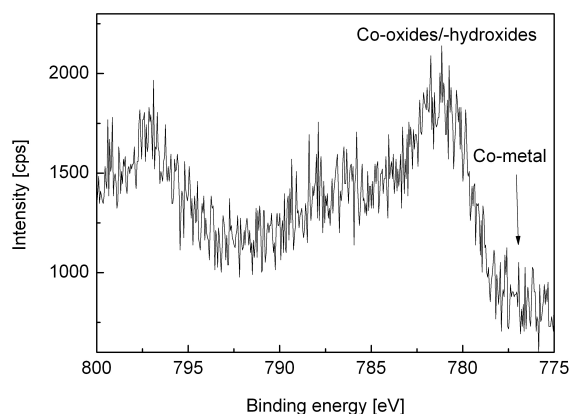


**Figure 4.7:** *Co 2p<sub>3/2</sub> hi res peaks of Co–ppHMDSN nanocomposite with 34% metal filling factor.*

The elemental content of the Co–ppHMDSN nanocomposites at the bulk level was analyzed using EDX. The relative atomic percentages of various elements of Co–ppHMDSN nanocomposites at various metal filling factors analyzed from EDX is shown in Figure 4.8. The increase in metal filling factor correlates with the decrease in the amount of carbon. The amount of silicon is higher at lower filling factors and decreases at higher filling factors. Oxygen is present in all nanocomposites which might be due to the influence of atmospheric oxygen or from water molecules deposited on the walls of the reaction chamber. The elemental analysis results from EDX are in agreement with the results from XPS (Table 4.1).

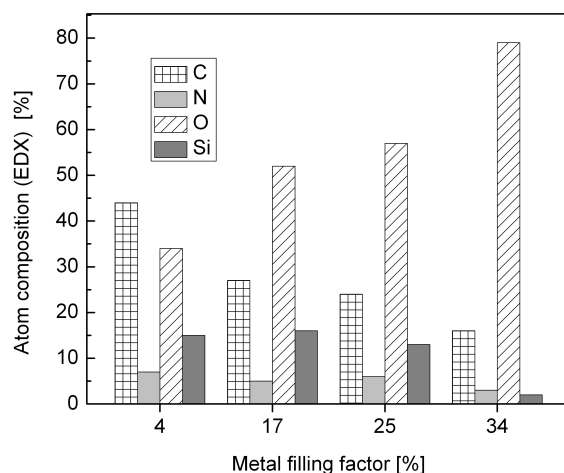


**Figure 4.8:** *Column chart representation of bulk relative atomic concentrations of various elements of cobalt–plasma polymerized HMDSN nanocomposites at various metal filling factors analyzed by EDX*

#### 4.1.4 ATR-FTIR investigations

The structure and bondings of the Co – ppHMDSN nanocomposites were studied using ATR-FTIR spectroscopy. The FTIR spectra showed characteristic peaks which can be attributed to several bonds. Table 4.3 gives a summary of the characteristic infrared absorption bonds of organo-silicon compounds from literature.

*Table 4.3: Characteristic infrared absorption bonds of organosilicon compounds. The label numbers correspond to the peak numbers in Figure 4.9.*

Wavenumber ( $\text{cm}^{-1}$ )	Mode	Label	Reference
3370	N–H stretching	1	[102]
2960	C–H stretching in $\text{CH}_3$	2	[102]
2900	C–H stretching in $\text{CH}_2$	3	[103]
1705	C=O stretching	4	[103]
1410	$\text{CH}_3$ asymmetric bending in $\text{Si}(\text{CH}_3)$	5	[104]
1260-1250	C–H symmetric deformation in $\text{Si}-\text{CH}_3$	6	[102]
1181	N–H bending	7	[102]
$\sim 1000$	Si–O asymmetric stretching	8	[103]
960-900	Si–N stretching	9	[105]
880-850	Si–C stretching	10	[105]
$\sim 780$	Si–C stretching	11	[98]

The measured FTIR spectra of the Co – ppHMDSN nanocomposites of various metal filling factors are illustrated in Figure 4.9. The FTIR spectrum of the pure plasma polymerized HMDSN film is also given. Several distinct peaks are observed in the pure HMDSN spectrum which are listed in Table 4.3. The label numbers in Table 4.3 correspond to the peak numbers in Figure 4.9.

### Pure plasma polymerized HMDSN film

Pure plasma polymerized (pp) HMDSN film was obtained by using only the upper RF electrode of the reaction chamber (see Figure 3.1). The obtained pure pp HMDSN film deposited on borosilicate glass substrates was transparent. A summary of organosilicon peaks from literature is given in Table 4.3. The different peaks in Figure 4.9 correspond to the labels in Table 4.3. Several distinctive peaks are observed in the FTIR spectrum of pure pp HMDSN films. They are:

- N–H stretching vibrations are seen at  $\sim 3370\text{ cm}^{-1}$ . This is a very broad

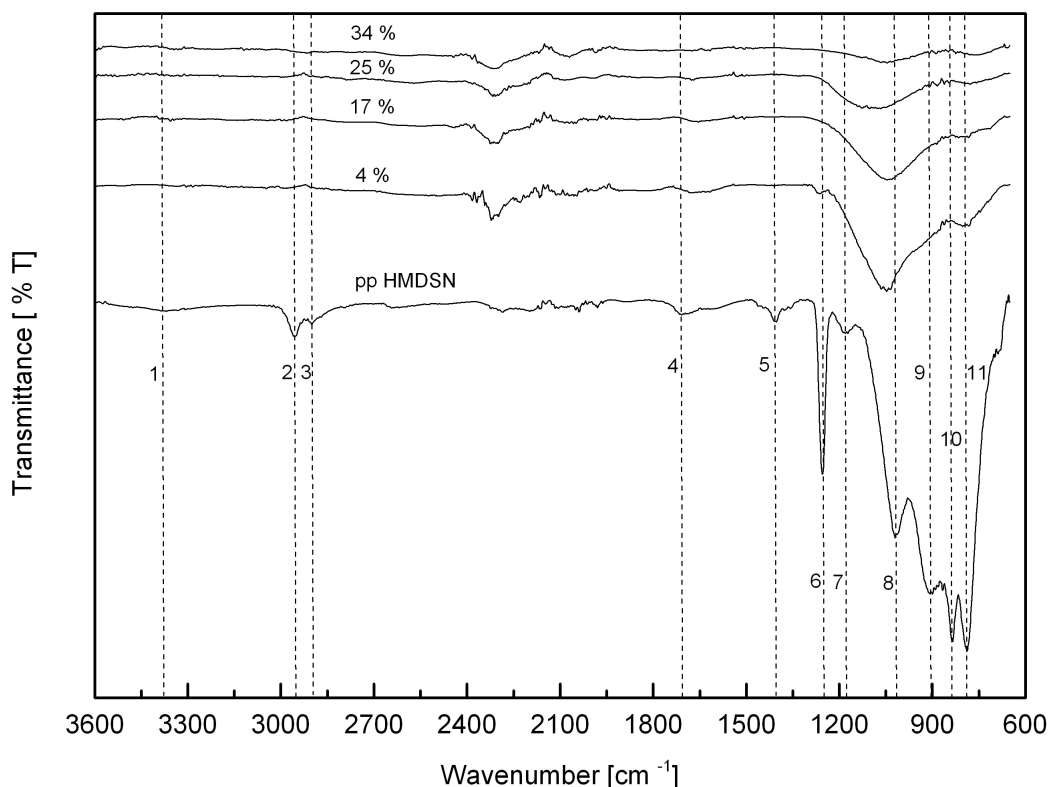


*Figure 4.9: ATR-FTIR spectra of cobalt-plasma polymerized HMDSN nanocomposites at various metal filling factors and pure plasma polymerized (pp) HMDSN film. The spectra are offset by the same value for better clarity. The labels correspond to Table 4.3*

peak and can be hardly seen (Label 1).

- C–H stretching vibrations in  $\text{CH}_3$  are seen at  $\sim 2960\text{ cm}^{-1}$ . This peak is seen as a narrow, sharp, distinctive peak (Label 2).

- C–H stretching vibrations in CH<sub>2</sub> are seen at ~2900 cm<sup>-1</sup>. This is observed as a small peak (Label 3).
- The weak, broad peak at ~1705 cm<sup>-1</sup> is due to the C=O stretching vibrations (Label 4).
- A small peak at ~1410 cm<sup>-1</sup> is seen which is due to CH<sub>3</sub> asymmetric bending in Si(CH<sub>3</sub>) (Label 5).
- The sharp peak at ~1260–1250 cm<sup>-1</sup> is due to the C–H symmetric deformation in Si–CH<sub>3</sub> (Label 6).
- The very small peak at ~1181 cm<sup>-1</sup> is due to the N–H bending vibrations (Label 7).
- Si–O asymmetric stretching vibrations are seen as the sharp, intense peak at ~1000 cm<sup>-1</sup> (Label 8).
- The peak at ~960–900 cm<sup>-1</sup> is due to the Si–N stretching vibrations (Label 9).
- The sharp peak at ~880–850 cm<sup>-1</sup> is due to the Si–C stretching vibrations (Label 10).
- The sharp peak at ~780 cm<sup>-1</sup> is due to the Si–C stretching vibrations (Label 11).

### **FTIR spectra of Co – pp HMDSN nanocomposites**

Different peaks are observed in the FTIR spectra of the Co – pp HMDSN nanocomposites:

1. A broad peak in the range 750–1150 cm<sup>-1</sup> is observed in all Co–pp HMDSN nanocomposites. This peak is an overlap of peaks due to Si–C stretching vibrations at 880–850 cm<sup>-1</sup>, Si–N stretching vibrations at 900–960 cm<sup>-1</sup> [105–107] and Si–O asymmetric stretching vibrations at around 1000 cm<sup>-1</sup> [102].
2. The peak obtained from C–H symmetric stretching in Si–CH<sub>3</sub> is seen at 1256 cm<sup>-1</sup> [102] at 4% metal filling factor.
3. The typical peaks at around 2950 cm<sup>-1</sup> and 2900 cm<sup>-1</sup> correspond to the C–H stretching in CH<sub>3</sub> and CH<sub>2</sub> bonds respectively [102, 103].
4. The peak at 2285 cm<sup>-1</sup> is due to the presence of atmospheric carbon dioxide.

There are many variations observed in the intensities of peaks and chemical structure as a function of metal filling factor. With respect to the Co–ppHMDSN nanocomposites the following points can be noted:

1. With the increase in metal filling factor there is a shift of the peak at  $\sim 1000\text{ cm}^{-1}$  to the higher wavenumbers. The peak was observed at  $1048\text{ cm}^{-1}$  at 4% metal filling factor which shifted to  $1084\text{ cm}^{-1}$  at 25% metal filling factor. The left shift of peak at  $1000\text{ cm}^{-1}$  with increasing filling factors can be ascribed to hydrolysis caused by water vapor [108].
2. With the increase in filling factor the polymer tends to get modified. More methyl groups are broken at higher metal filling factors because more magnetron power was used to prepare these nanocomposites. The degree of methyl abstraction increases as more methyl groups recombine and form volatile hydrocarbons which get pumped out of the chamber [109]. Accordingly, the intensity of the peak at  $1256\text{ cm}^{-1}$  decreases with an increase in the metal filling factor.
3. The N–H bond at  $\sim 1180\text{ cm}^{-1}$  is not observed in the Co–ppHMDSN nanocomposites suggesting the decomposition of the N–H bond. Additionally, the Si–N bond at  $\sim 960\text{--}900\text{ cm}^{-1}$  gets dissociated in the Co–ppHMDSN nanocomposites due to its lower bond energy [109]. Thus, with the increase in filling factor the Si–N,  $\text{CH}_3$  bonds in the polymer matrix tend to get destroyed.
4. The peak at  $2285\text{ cm}^{-1}$  in all films is due to the presence of atmospheric carbon dioxide.
5. The influence of water is observed in all nanocomposites as Si–O vibrations at  $1000\text{ cm}^{-1}$ . Consequently, the broad peak at  $1000\text{ cm}^{-1}$  in all investigated nanocomposites corresponds to a mixture of Si–O and Si–C bonds.

#### 4.1.5 Surface conductivity map using CAFM

Conductive atomic force microscopy was employed in contact mode to study the surface conductivity properties of Co–ppHMDSN nanocomposites. Surface conductivity was observed only in the nanocomposite with 34% metal filling factor. At other filling factors no signal was observed in the conductivity mode. The 3D topography and conductivity images taken simultaneously for the nanocomposite at the 34% filling factor are shown in Figure 4.10. A DC bias voltage of 4 V was applied.

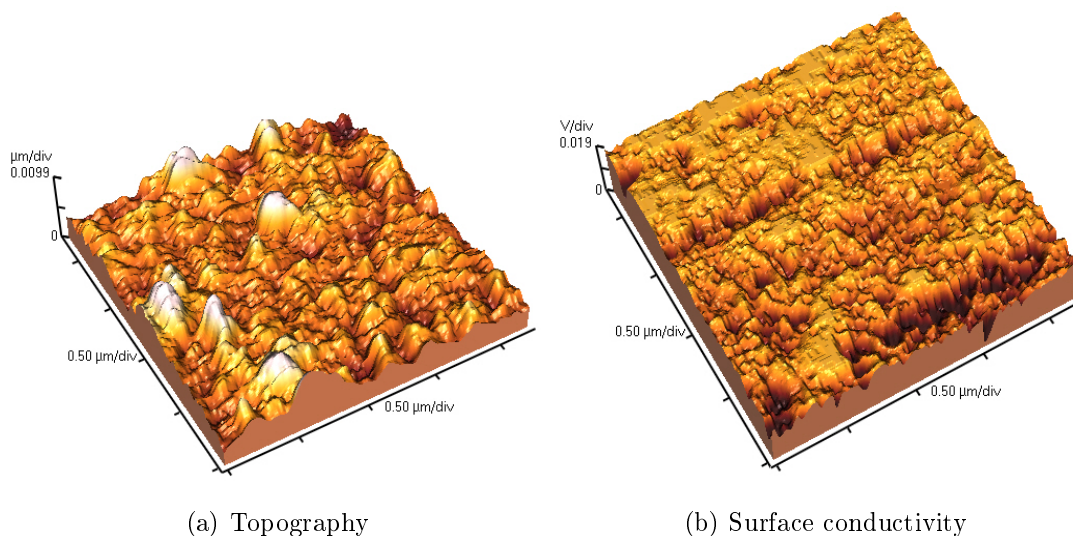


**Figure 4.10:** 3D a) topography and b) surface conductivity images of cobalt–plasma polymerized HMDSN nanocomposite at 34% metal filling factor. DC bias voltage applied = 4 V.

In Figure 4.10 the conductive areas are indicated by bright regions, and the non-conductive areas by dark regions. The conductivity image in Figure 4.10(b) depicts that the surface of the nanocomposite is almost conductive with a few dark spots or holes which might correspond to the non-conducting regions. The size of the CoO particle as evaluated from XRD and TEM is  $\sim 6$  nm. However, the features in conductivity image are more than 6 nm in size. This is because of the limitation of the radius of the cantilever tip. As the tip radius is  $\sim 25$  nm and when the tip encounters a conducting region it maybe in contact with several CoO nanoparticles. Thus the feature size in conductivity image corresponds to the tip radius. Therefore, the conductivity map from Figure 4.10(b) is an indication that the Co–ppHMDSN nanocomposite with 34% metal filling factor exhibits surface conductivity. No surface conductivity signal was observed in nanocomposites with 17% and 25% metal filling factors. Using conductive AFM the surface conductivity properties of the Co–ppHMDSN nanocomposites was qualitatively studied. Thus, Co–ppHMDSN nanocomposites with varying surface conductivity characteristics were prepared.

## 4.2 X-ray absorption spectroscopy analysis

Co–ppHMDSN nanocomposites were analysed using various techniques like XRD, XPS, EDX, and FTIR. However, it was observed that cobalt was present mostly in amorphous form in these nanocomposites. In order to study the local structure around the cobalt atom powerful XAS technique was employed. Co–ppHMDSN nanocomposites were analysed at the BESSY synchrotron radiation center in Berlin.

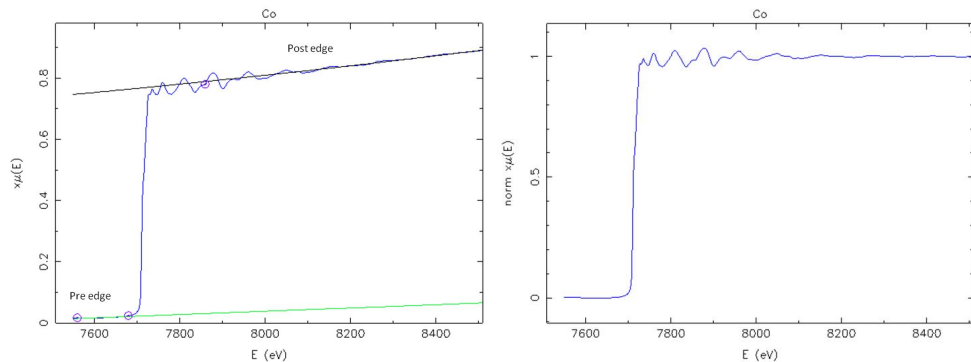
### 4.2.1 Steps and parameters in analysing an XAS spectrum

Several standards were used for comparison in the XAS analysis. Co on foil,  $\text{Co}_3\text{O}_4$ ,  $\text{CoO}$ , and  $\text{Co}_2\text{O}_3$  powder standards were analysed. For all the standards and the Co–ppHMDSN nanocomposites deglitching was performed prior to analysis. For some spectra truncation was done at the higher energy range to avoid the noise at the higher end of energies. An example depicting the steps in analysing the XAS spectrum of cobalt standard is shown in Figure 4.11. The cobalt foil standard is taken as an example. The detailed description of the steps is explained previously in Section 2.3.1.5.

The various parameters involved in the analysis of XAS spectra using the software ATHENA are discussed below.

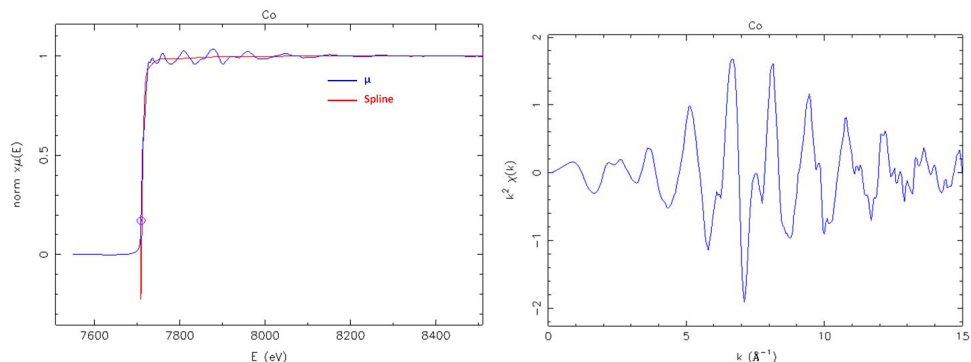
#### Background removal section:

- $E_0$  - threshold energy of the absorption edge - This is the energy where the photoelectron is released.  $E_0$  is determined by IFEFFIT as the first peak of the first derivative of  $\chi(E)$ .
- $\Delta\mu(E_0)$  - edge step: This is measured as  $\mu_0(E_0)$ . It is the value of background function evaluated at edge energy [89]. It is the difference of values at  $E_0$  of pre- and post-edge lines extrapolated to  $E_0$ .
- Rbkg - Background removal parameter: This parameter describes the frequency cutoff between the background and data. ATHENA uses AUTOBK algorithm for background removal. The part of  $\mu(E)$  with low frequency Fourier components is the background, whereas the high frequency Fourier components contain the data. The 'rbkg' parameter determines the value below which the AUTOBK algorithm removes the Fourier components [89]. 'Rbkg' should be chosen so that the necessary data should be present and also the low R peaks be minimized.



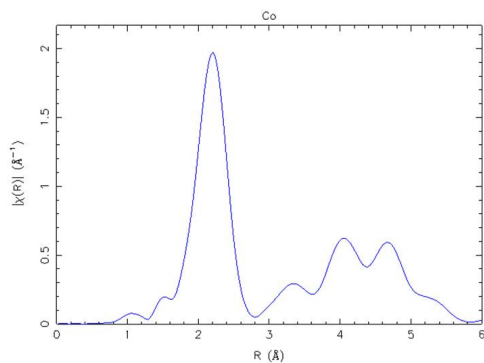
(a) Pre-edge removal

(b) Normalization



(c) Post edge background removal using spline

(d) EXAFS function  $\chi(k)$



(e) Fourier transform of  $\chi(k)$  to R-space resulting in Radial Distribution Function (RDF)

**Figure 4.11:** Steps involved in the analysis of X-ray absorption spectrum - example using a cobalt metal foil standard. The detailed description of the steps is explained previously in Section 2.3.1.5.



- Spline range: The range of spline function used to approximate the background function can be varied. Spline range should be chosen carefully as the EXAFS function  $\chi(k)$  will be zero outside the spline range. When the spectrum has a sharp, white line it makes background removal easier by choosing the lower end of the spline range a little above the white line. In this way the AUTOBK algorithm can overcome the difficulty of following the swiftly changing spectrum at the edge [89].

#### **Forward Fourier Transform section:**

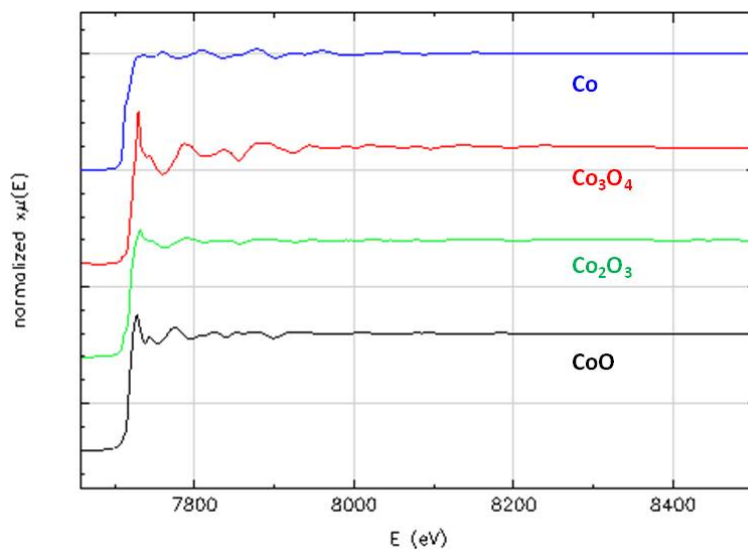
- k-weight: This parameter is varied such that the size of oscillation of the EXAFS function  $\chi(k)$  is roughly constant over the range of data. Since the oscillations attenuate quickly after the edge, k-weight is used to amplify the data at high k-values.
- k-range: This is the range of data of the EXAFS function  $\chi(k)$  which would be transformed to R-space using Fourier transform. k-range is chosen such that there are no glitches present and all the necessary data is present in the selected k-range.
- Window: This is the window function used in the Fourier transformation of the EXAFS function  $\chi(k)$  to the R-domain as  $\chi(R)$ .

Co–ppHMDSN nanocomposites prepared using a hybrid PVD/PECVD process were thoroughly investigated using X-ray absorption spectroscopy. Nanocomposites prepared at different metal filling factors were analyzed using EXAFS and XANES. Additionally, the variation of the x-ray absorption spectra of the nanocomposites with the variation of the plasma parameters like power of magnetron, flow of gases, and distance from the target were studied using EXAFS and XANES. It is shown that by tuning the plasma parameters nanocomposites containing metallic cobalt, cobalt oxide and a mixture of both metallic cobalt and oxides can be produced.

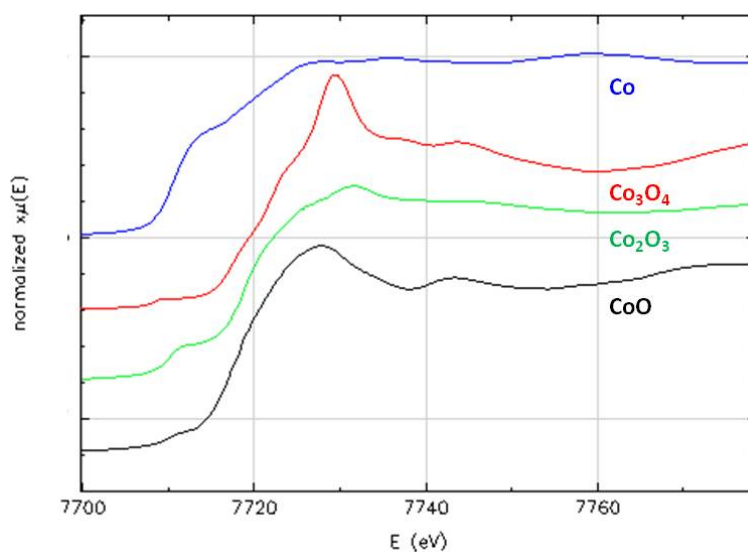
#### **4.2.2 XAS investigations of cobalt standards**

In addition to the Co–ppHMDSN nanocomposites XAS measurements were also performed on the standard Co, CoO, Co<sub>2</sub>O<sub>3</sub> and Co<sub>3</sub>O<sub>4</sub> samples. The normalized absorption spectra of the standards are shown in Figure 4.12. The normalized XANES spectra of the standards are shown in Figure 4.13. The various peaks from the XANES spectra of the cobalt standards are tabulated in Table 4.4. The edge energies ( $E_0$ ) are also

indicated. The edge energies and the XANES peaks are consistent with the values in literature as mentioned in Table 4.4.



*Figure 4.12: Normalized absorption spectra of cobalt standards.*

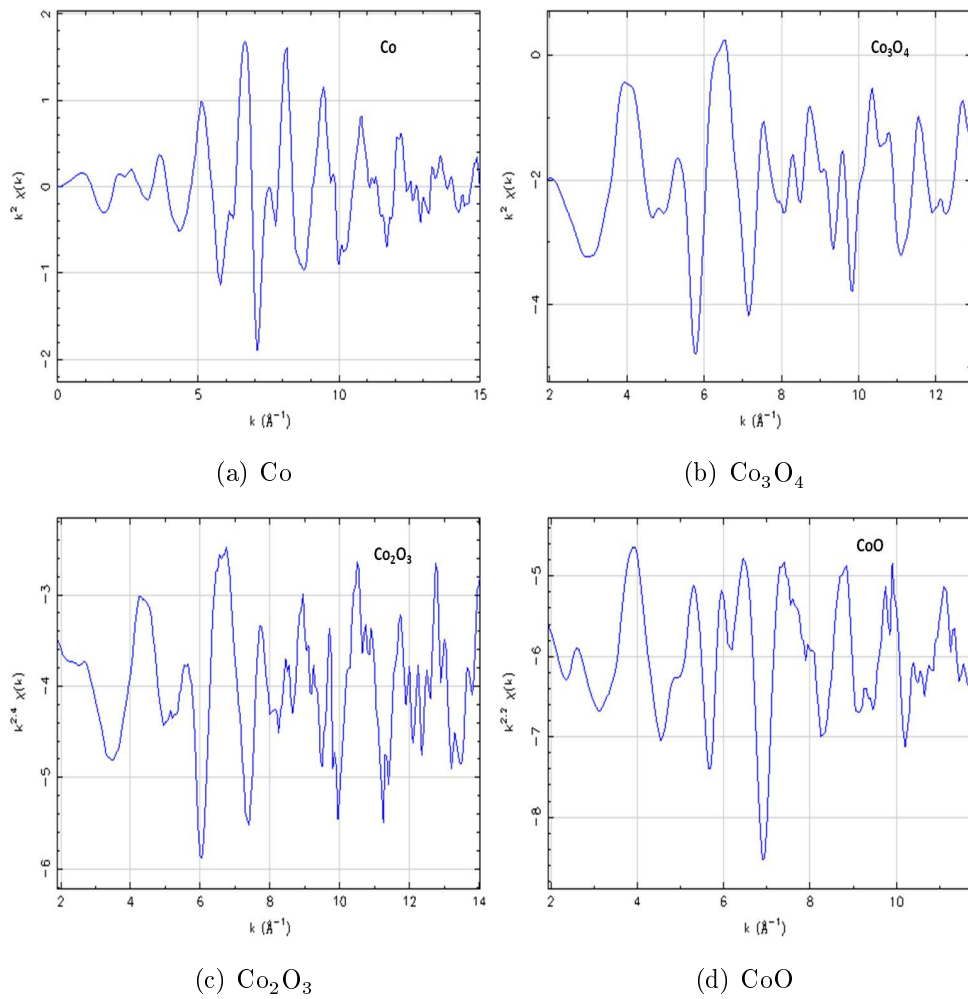


*Figure 4.13: Normalized XANES spectra of cobalt standards.*

Figure 4.14 gives the EXAFS function  $\chi(k)$  of the various cobalt standards. The EXAFS function  $\chi(k)$  of the cobalt standards was transformed into R-space using Fourier transform to obtain the radial distribution function (RDF). Kaiser-Bessel window was used for all standards. The Fourier transform (FT) plots are shown in Figure 4.15 and

*Table 4.4: Edge energies and XANES peaks of cobalt standards*

Sample	$E_0$ (eV)	XANES peaks (eV)	Reference
Co	7709.28	7726.61, 7735.80, 7759.60	[110]
Co <sub>3</sub> O <sub>4</sub>	7728.32	7729.75, 7737.05, 7743.80, 7775.00	[110]
Co <sub>2</sub> O <sub>3</sub>	7718.68	7731.56, 7745.72, 7777.37	[111]
CoO	7717.28	7727.9, 7743.5, 7775.3	[110]

*Figure 4.14: EXAFS function  $\chi(k)$  of the cobalt standards.*

the peaks in Table 4.5. The RDFs and the peaks in the FT plots of the standards are consistent with the values in literature as mentioned in Table 4.5.

The peak at 2.2 Å in the RDF of the cobalt standard corresponds to the first coordination sphere [110]. The peak at 1.62 Å in the RDF of CoO corresponds to Co–O bond in the first coordination shell, whereas the peak at 2.64 Å corresponds to Co–Co bond in the second coordination shell [112, 113]. Co<sub>3</sub>O<sub>4</sub> has a spinel type structure with Co<sup>2+</sup> ions in tetrahedral interstices and Co<sup>3+</sup> ions in octahedral interstices. The peaks in the RDF of Co<sub>3</sub>O<sub>4</sub> do not always correspond to a single coordination shell. The peak at ~1.45 Å in the RDF of Co<sub>3</sub>O<sub>4</sub> corresponds to the Co–O bonds of the first shell of both Co<sup>3+</sup> and Co<sup>2+</sup> ions. The peak at 2.5 Å in the RDF of Co<sub>3</sub>O<sub>4</sub> corresponds to the Co–Co bond of the second coordination shell around Co<sup>3+</sup> ions. The peak at ~3.05 Å in the RDF of Co<sub>3</sub>O<sub>4</sub> corresponds to both Co–O and Co–Co bonds of higher order coordination shell of both Co<sup>3+</sup> and Co<sup>2+</sup> ions [111].

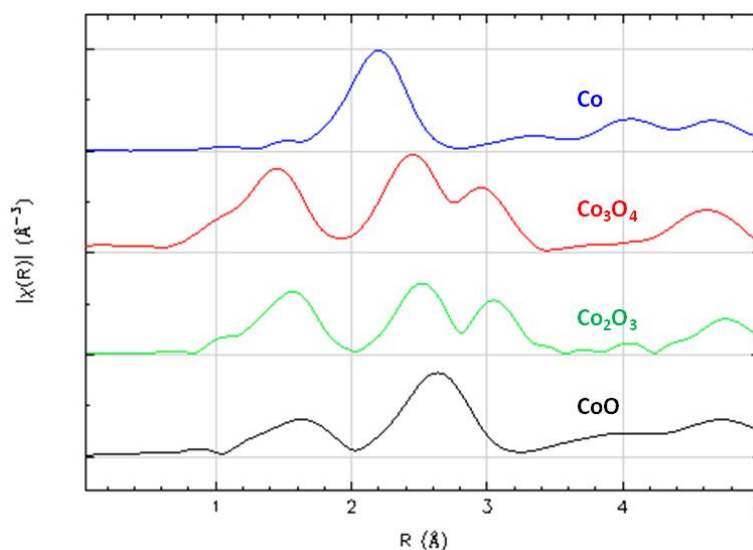


**Figure 4.15:** Radial distribution function (RDF) of cobalt standards.

**Table 4.5:** Fourier transform (FT) peaks of cobalt standards

Sample	FT peaks (Å)	Reference
Co	2.2	[110]
Co <sub>3</sub> O <sub>4</sub>	1.45, 2.45, 2.95	[112]
Co <sub>2</sub> O <sub>3</sub>	1.57, 2.53, 3.05	[111]
CoO	1.62, 2.64	[111], [113]

### 4.2.3 XAS investigations of Co – pp HDMSN nanocomposites with different metal filling factors

XAS investigations was performed on three nanocomposites with metal filling factors of 34%, 25% and 17%. The normalized absorption spectra of Co – pp HDMSN nanocomposites at three different metal filling factors are show in Figure 4.16. Cobalt standards are also illustrated for comparison.

Figure 4.16 depicts that the absorption spectra of the three nanocomposites are quite similar to each other. When compared with the standards, all three spectra appear to be identical to the spectrum of CoO. The presence of high peak, i.e. the white line after the edge in the spectra of all three nanocomposites suggests the influence of oxygen. A closer look can be had by observing the XANES spectra in Figure 4.17.

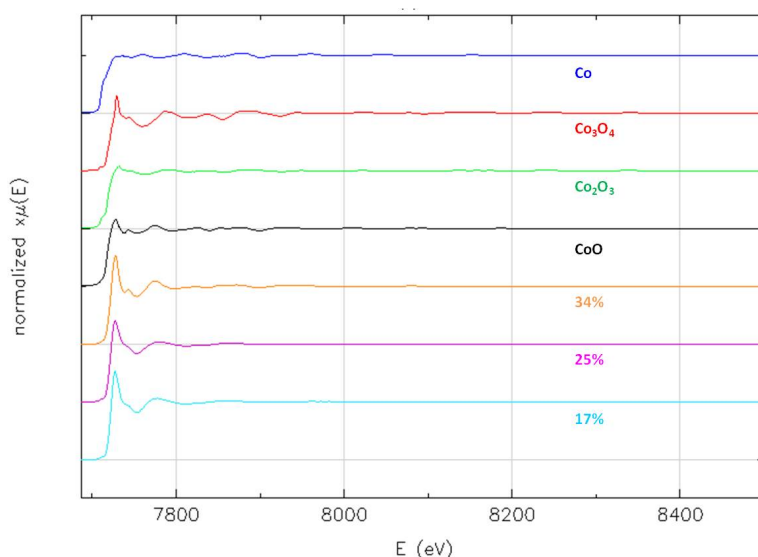


**Figure 4.16:** Normalized absorption spectra of cobalt standards and Co – pp HDMSN nanocomposites at various metal filling factors (34%, 25% and 17%).

By comparing the pre-edge region of all nanocomposites and the standards it can be said that the pre-edge region in the XANES spectra of the nanocomposites closely follow CoO. The width of the absorption edge in XANES increases with decreasing metal volume fraction pointing to higher disorder around cobalt [114]. The various peaks in the XANES spectra are tabulated in Table 4.6. The edge energies ( $E_0$ ) are also indicated. Table 4.6 indicates a shift in the absorption edge  $E_0$  of the nanocomposites when compared to the standards Co,  $\text{Co}_2\text{O}_3$ , CoO, and  $\text{Co}_3\text{O}_4$  (see Table 4.4). This infers that the effective valence state of cobalt in the nanocomposites is more than that

of the standards. The valency of Co in CoO is +2 and in  $\text{Co}_2\text{O}_3$  is +3. The movement of the absorption edges to higher energies in the XANES spectra of the nanocomposites suggests an increase in the effective valence state of cobalt in the nanocomposites [111]. The XANES peaks of the nanocomposites are close to the peaks of CoO spectrum. Additionally, when compared to the  $\text{Co}_3\text{O}_4$  standard, the absorption edge is shifted and the valence state is not higher than in  $\text{Co}_2\text{O}_3$ . This indicates that besides the main CoO component a smaller fraction of  $\text{Co}_3\text{O}_4$  is present. Upon observing the pre-edge features, XANES peaks and the shift of the absorption energies it can be said that +2 is one of the valence states of cobalt and CoO is one of the probable chemical configurations of Co in all three nanocomposites.

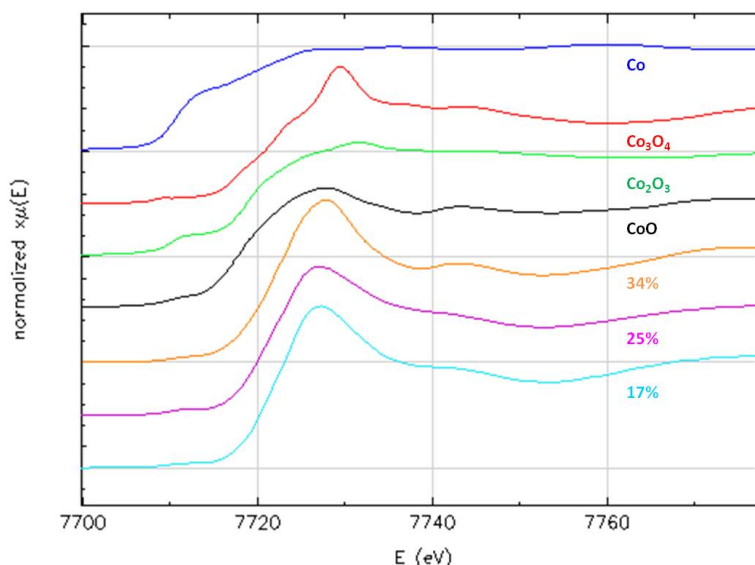


**Figure 4.17:** Normalized XANES spectra of cobalt standards and Co-pp HMDSN nanocomposites at various metal filling factors (34%, 25% and 17%).

**Table 4.6:** Edge energies and XANES peaks of Co-pp HMDSN nanocomposites at various metal filling factors.

Filling factor	$E_0$ (eV)	XANES peaks (eV)
34%	7721.4	7728.00, 7743.12, 7775.56
25%	7721.21	7727.00, 7742.77, 7778.30
17%	7723.36	7727.00, 7743.34, 7776.92

Figure 4.18 gives the EXAFS function  $\chi(k)$  of the nanocomposites. The EXAFS function  $\chi(k)$  of each nanocomposite was transformed into R-space using Fourier transform. Kaiser-Bessel window was used. Upon transformation the radial distribution function (RDF)  $\chi(R)$  was obtained. The Fourier Transform (FT) plots are shown in Figure 4.19. The FT plots of the standards are also depicted for comparison purpose. The peaks in the FT plots are tabulated in Table 4.7. From the FT plots and peaks it can be said that there is an influence of oxides in the nanocomposites. The nanocomposite with 34% metal filling factor has two peaks. The first peak at  $\sim 1.56 \text{ \AA}$  overlaps with peaks corresponding to cobalt oxides. The second peak at  $\sim 2.54 \text{ \AA}$  has an overlapping area both with cobalt oxides and metallic cobalt. Because of the complex FT plot it is difficult to determine exactly what species comprise the first and second coordination shells. However, by observing the XANES and the RDF it can be said that in the nanocomposite at 34% filling factor the first and second coordination shells are comprised of a mixture of cobalt and cobalt oxides.

FT plots of nanocomposites at 25% and 17% filling factors indicate only one major peak at  $1.43 \text{ \AA}$  and  $1.47 \text{ \AA}$  respectively. These peaks have an overlap with the  $1.45 \text{ \AA}$  peak of  $\text{Co}_3\text{O}_4$ . But, the peaks in the nanocomposites at 25% and 17% filling factors have a very little overlap with the peak of the Co metal at  $2.2 \text{ \AA}$ . This suggests that the oxide content is dominant over the metallic content in these nanocomposites. The XANES spectra of nanocomposites at 25% and 17% filling factors point to the presence of CoO configuration. If the RDF and the XANES of the nanocomposites at 25% and 17% filling factors are taken into consideration it can be said that these two nanocomposites are chemically dominated by cobalt oxides with a small amount of metallic cobalt. The overlap of the nanocomposite at 34% filling factor and the metallic cobalt in the RDF is higher when compared to the overlap of other nanocomposites with metallic cobalt. This infers the presence of more cobalt in the nanocomposite at 34% filling factor when compared to the other two nanocomposites. The nanocomposites at 25% and 17% filling factors also have an overlap with the metallic cobalt in the range of  $R = 1\text{--}2 \text{ \AA}$ . However, this is less when compared to the overlap of the nanocomposite at 34% filling factor with the metallic cobalt in the range of  $R = 2\text{--}3 \text{ \AA}$ . Thus it can be said that the nanocomposite at 34% filling factor has more metallic cobalt than oxide, and nanocomposites at 25% and 17% filling factors have more oxide than metallic cobalt. A trend is observed such that with the increase in the filling factor the metallic cobalt dominates over cobalt oxides.

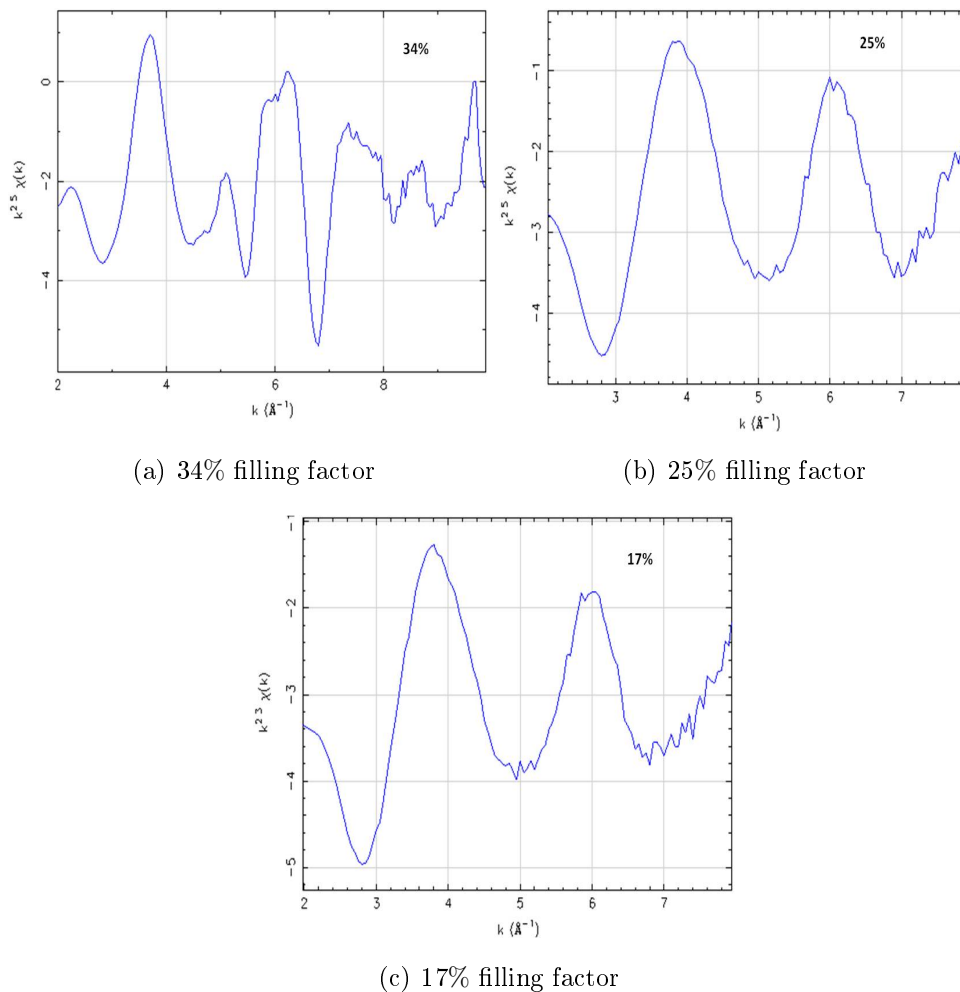


**Figure 4.18:** EXAFS function  $\chi(k)$  of Co – pp HMDSN nanocomposites at various metal filling factors (34%, 25% and 17%).

**Table 4.7:** FT peaks of Co – pp HMDSN nanocomposites at various metal filling factors.

Filling factor	FT peaks (Å)
34%	1.56, 2.54
25%	1.43
17%	1.47



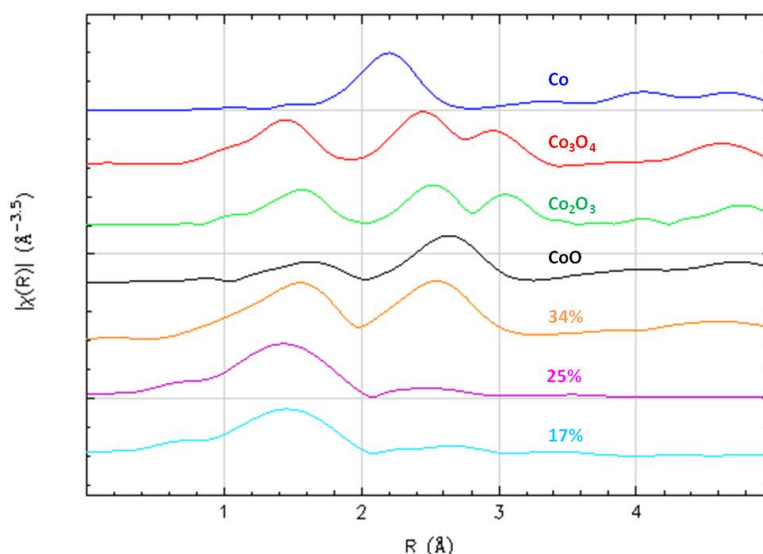


**Figure 4.19:** *RDF of cobalt standards and Co-ppHMDSN nanocomposites at various metal filling factors (34%, 25% and 17%).*

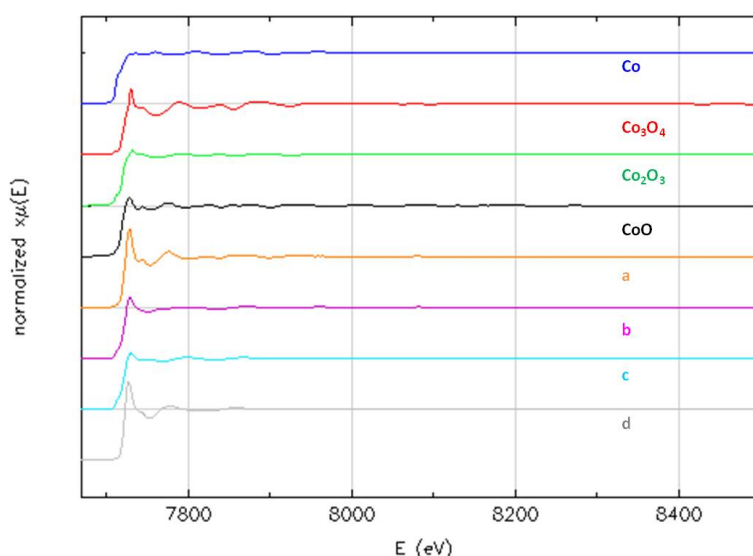
#### 4.2.4 Influence of the variation of plasma parameters - XAS investigations of Co-ppHMDSN nanocomposites prepared with varying plasma parameters

The effects of the variation of plasma parameters such as the flow of HMDSN, power of magnetron and distance between the source and target on the X-ray absorption spectra were studied. Various nanocomposites were prepared at varying plasma parameters as shown in Table 4.8. Figure 4.20 shows the normalized absorption spectra of the Co-ppHMDSN nanocomposites a-d. The spectra from cobalt standards are also depicted for comparison.

Figure 4.20 illustrates the presence of white line in nanocomposites ‘a’, ‘b’ and ‘d’. However, it is not prominent in nanocomposite ‘c’ when compared to the other nanocomposites. This is perhaps because of the higher amount of cobalt introduced in nanocomposite ‘c’ as it is more close to the target when compared to the other nanocomposites. The presence of more cobalt reduces the influence of oxygen as evidenced by the lesser peak of the white line in nanocomposite ‘c’. The normalized XANES spectra of samples a-d and the standards are depicted in Figure 4.21. The pre-edge features and XANES spectra after the edge demonstrate that the spectra of nanocomposites ‘a’ and ‘d’ are similar to CoO spectrum. The pre-edge features of nanocomposites ‘b’ and ‘c’ are similar to each other and also to  $\text{Co}_2\text{O}_3$ . However, their spectra after the edge

**Table 4.8:** Co – pp HMDSN nanocomposites prepared at various plasma parameters.

Nanocomposite	Flow of Ar (sccm)	Flow of HMDSN (sccm)	Power of magnetron (W)	Distance from target (cm)
a	8	0.06	300	6
b	8	0.06	200	6
c	8	0.06	300	3
d	8	0.2	300	6

**Figure 4.20:** Normalized absorption spectra of cobalt standards and Co – pp HMDSN nanocomposites a–d.

are not similar. Additionally, the peak of the white line in nanocomposite ‘c’ is much less when compared to the others suggesting less influence of oxygen or more presence of cobalt. Table 4.9 gives a summary of the edge energies  $E_0$  and the XANES peaks of nanocomposites a–d. The edge energies  $E_0$  of all nanocomposites a–d are shifted to the right when compared to the Co and cobalt oxide standards. As the XANES peaks of nanocomposites ‘a’ and ‘d’ are close to CoO it can be said that CoO maybe a part of the chemical configuration of nanocomposites ‘a’ and ‘d’. The onset and rising of the peak in the pre-edge region of nanocomposites ‘b’ and ‘c’ look similar. The peak of the white line is less in nanocomposites ‘b’ and ‘c’ when compared to nanocomposites ‘a’ and ‘d’.

Therefore, it indicates that nanocomposites 'b' and 'c' have more metallic cobalt than nanocomposites 'a' and 'd'.

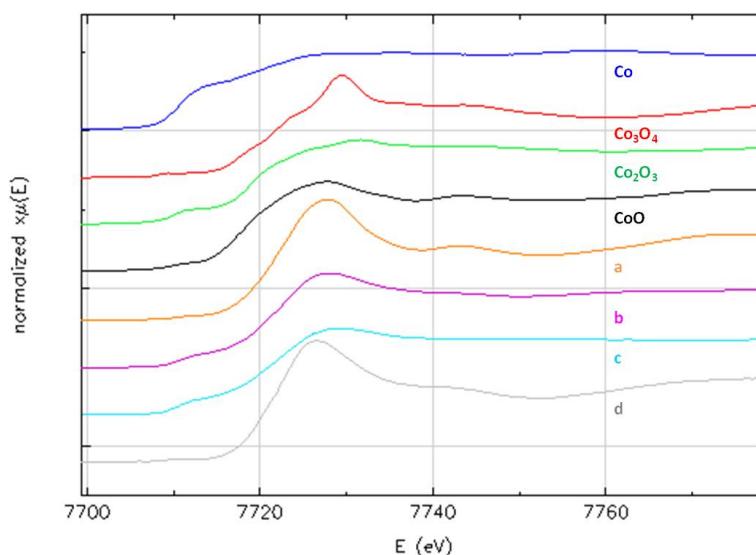


**Figure 4.21:** Normalized XANES spectra of cobalt standards and Co-ppHMDSN nanocomposites a-d.

**Table 4.9:** Edge energies and XANES peaks of Co-ppHMDSN nanocomposites a-d.

Nanocomposite	$E_0$ (eV)	XANES peaks (eV)
a	7721.4	7727.85, 7743.42, 7774.99
b	7722.25	7728.04, 7743.17
c	7724.61	7729.4
d	7722.54	7726.68, 7743.25, 7775.6

Figure 4.22 depicts the EXAFS function  $\chi(k)$  of nanocomposites a-d. The Fourier transform (FT) of  $\chi(k)$  was performed using Kaiser-Bessel window, and the obtained RDFs for nanocomposites a-d are shown in Figure 4.23. The RDFs of the cobalt standards are also illustrated. The peaks from the FT plots are shown in Table 4.10.

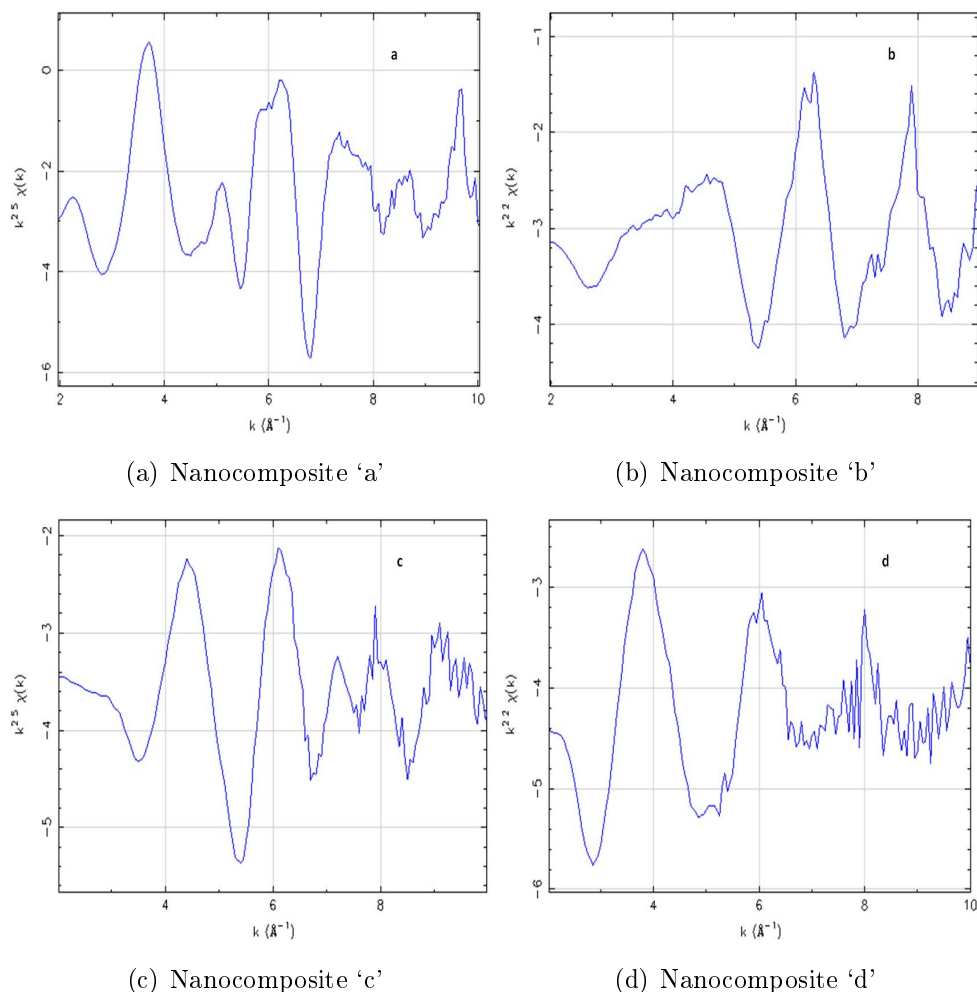


**Figure 4.22:** EXAFS function  $\chi(k)$  of Co–pp HMDSN nanocomposites a–d.

The FT peaks and the FT plots depict the influence of oxides in all nanocomposites. Nanocomposite 'a' has two peaks which overlap with the peaks from both the cobalt oxides and metallic cobalt. Therefore it is difficult to distinguish exactly what species contribute to the first and second coordination shells. The FT plots of nanocomposites 'b' and 'c' are similar. Both of them have peaks at  $\sim 2 \text{ \AA}$  which are close to the peak in the cobalt standard. Nanocomposites 'b' and 'c' have more overlap with the metallic cobalt in the range  $R = 2\text{--}3 \text{ \AA}$  than with cobalt oxides in the range  $R = 1\text{--}2 \text{ \AA}$  or  $2\text{--}3 \text{ \AA}$ . This infers that the metallic cobalt species dominate over the oxide species in the first coordination shells of the nanocomposites 'b' and 'c'. Nanocomposite 'd' has a major overlap with CoO peak and very little with metallic cobalt. This suggests that the first coordination shell of nanocomposite 'd' is dominated by cobalt oxide. These

observations from the RDF analysis are in agreement with the XANES analysis.

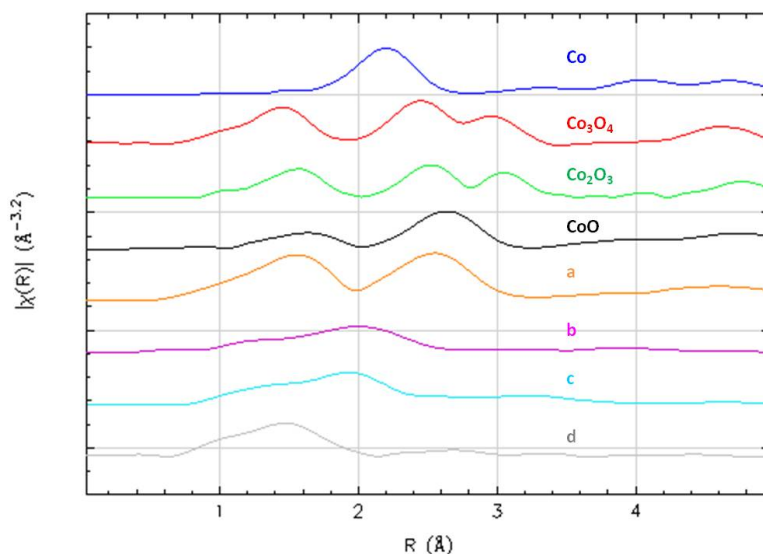


Figure 4.23: RDF of cobalt standards and Co-pp HMDSN nanocomposites a-d.

Table 4.10: FT peaks of Co-pp HMDSN nanocomposites a-d

Nanocomposite	FT peaks (Å)
a	1.56, 2.54
b	1.25, 2.00
c	1.93
d	1.47

To summarize the effect of variation of plasma parameters on the X-ray absorption spectra we can say that:

- With the decrease of the distance between the target and the substrate (compare nanocomposites ‘a’ and ‘c’ ) when all other plasma parameters are kept constant the influence of oxygen is reduced. The first coordination shell is dominated by metallic cobalt species. More amount of metallic cobalt is introduced and the influence of cobalt oxides is reduced as evident from the FT plots and the white lines in the absorption spectra.
- Upon increasing the flow of HMDSN the amount of Co is reduced as seen from the very little overlap of the 1.47 Å peak of nanocomposite ‘d’ with the 2.2 Å peak of

the metallic cobalt standard. In nanocomposite ‘d’ it is clear that cobalt oxide is the dominant species in the first coordination shell. But in nanocomposite ‘a’ even the contribution of metallic cobalt is appreciable and is in comparison to that of cobalt oxides.

- By reducing the power of magnetron the influence of oxygen in nanocomposite ‘b’ is less when compared to that in nanocomposite ‘a’. This is evident from the XANES peak of nanocomposite ‘b’ which is similar to that of nanocomposite ‘c’. Additionally, the FT plot indicates the presence of more oxygen in nanocomposite ‘a’. This might be because at higher magnetron power more bonds are broken in nanocomposite ‘a’ which results in more unsaturated bonds. Therefore, the influence of oxygen is higher.

#### 4.2.5 Influence of the variation of flow of Ar - XAS investigations of Co – pp HMDSN nanocomposites prepared with varying flow of Argon

Three nanocomposites e, f and g were prepared by varying the flow of Argon as 8, 5, and 1 sccm respectively. All three were prepared at 300 W magnetron power and at 6 cm distance from the target. The flow of HMDSN was kept constant at 0.06 sccm. The normalized absorption spectra of the three nanocomposites are shown in Figure 4.24. The spectra of cobalt standards are also shown.

A white line is observed in all three nanocomposites e–g indicating the influence of oxide. The normalized XANES spectra are shown in Figure 4.25, and the peaks are shown in Table 4.11. The edge energies  $E_0$  of all nanocomposites e–g are shifted to the right when compared to the standards cobalt, CoO and  $\text{Co}_2\text{O}_3$ .

**Table 4.11:** Edge energies and XANES peaks of Co – pp HMDSN nanocomposites e–g.

Nanocomposite	$E_0$ (eV)	XANES peaks (eV)
e	7721.4	7727.80, 7743.12, 7774.88
f	7722.31	7727.50, 7742.37
g	7721.2	7727.33, 7742.33, 7779.68

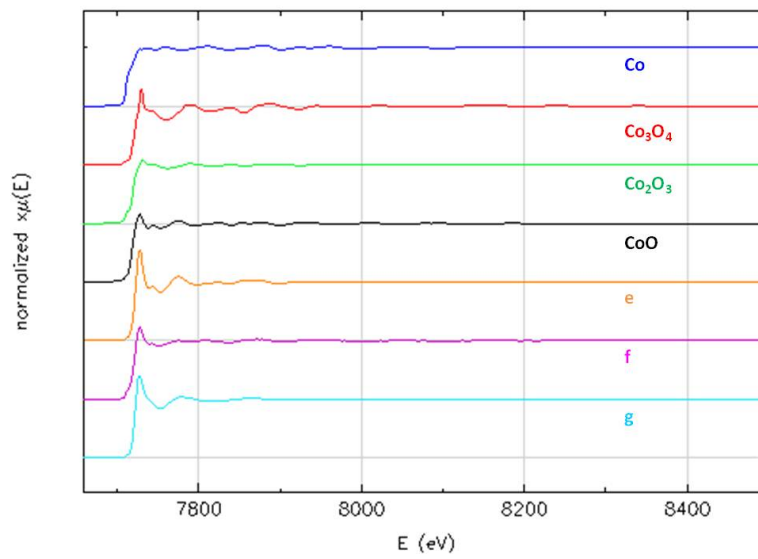


*Figure 4.24: Normalized absorption spectra of cobalt standards and Co-ppHMDSN nanocomposites e-g.*

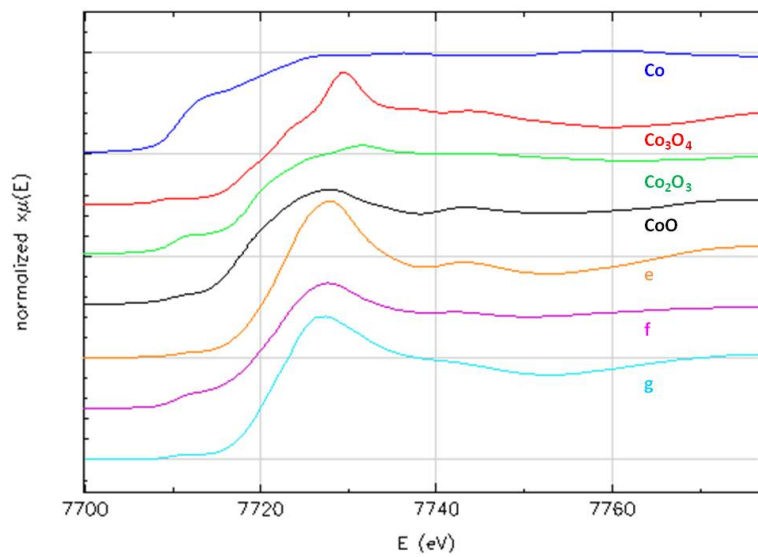


*Figure 4.25: Normalized XANES spectra of cobalt standards and Co-ppHMDSN nanocomposites e-g.*

This suggests that the effective valence state of cobalt in the nanocomposites is more than that of the standards. The valency of Co in CoO is +2 and in Co<sub>2</sub>O<sub>3</sub> is +3. The movement of the absorption edges to higher energies in the XANES spectra of the nanocomposites points to the increase in the effective valence state of cobalt in the nanocomposites [111]. The XANES peaks of the nanocomposites are close to the peaks of CoO spectrum. An observation of the pre-edge features, the XANES peaks and the shift of the absorption energies depicts that +2 is one of the valence states of cobalt, and CoO is one of the probable chemical configurations of Co in all three nanocomposites. The onset of peak in the pre-edge region of the nanocomposite ‘f’ illustrates the presence of more amount of metallic cobalt. This is also supported by a weaker white line in nanocomposite ‘f’. This can be explained because of the lower pressure in the chamber (due to less flow of Ar). Consequently, there are less number of collisions resulting in fewer energetic ions. This leads to lesser number of unsaturated bonds which must have reduced the influence of oxygen. Figure 4.26 depicts the EXAFS function  $\chi(k)$  of nanocomposites e–g. The Fourier transform (FT) of  $\chi(k)$  is performed using Kaiser-Bessel window and the obtained RDFs for nanocomposites e–g are shown in Figure 4.27. The RDFs of the cobalt standards are also shown. The peaks from the FT plots are shown in Table 4.12.

The FT peaks and the FT plots suggest the presence of oxides in all nanocomposites e–g. Nanocomposite ‘e’ has two peaks which overlap with the peaks of both cobalt oxides and metallic cobalt. Therefore it is difficult to distinguish exactly what species contribute to the first and second coordination shells. However, it can be said that nanocomposite ‘e’ has a complex configuration of first and second coordination shells with both metallic cobalt and cobalt oxides. When the flow of Ar is reduced to 5 sccm (nanocomposite ‘f’) the FT plot contains only one peak at  $\sim 2.1 \text{ \AA}$  which has overlapping areas with both metallic cobalt and cobalt oxides. It is difficult to determine exactly the different species of the first coordination shell of nanocomposite ‘f’. However, it can be said that there are both metallic cobalt and cobalt oxides present. When the flow of Ar is further reduced to 1 sccm Ar (as seen in nanocomposite ‘g’) the peak at  $\sim 1.44 \text{ \AA}$  corresponds to both cobalt oxide and metallic cobalt.

To summarize, with the increase in the flow of Ar the pressure in the chamber increases resulting in more number of unsaturated bonds, and thus there is more influence of oxygen. Furthermore, the chemical configuration of the first coordination shell around cobalt gets more complex, and the contribution from cobalt oxide increases.



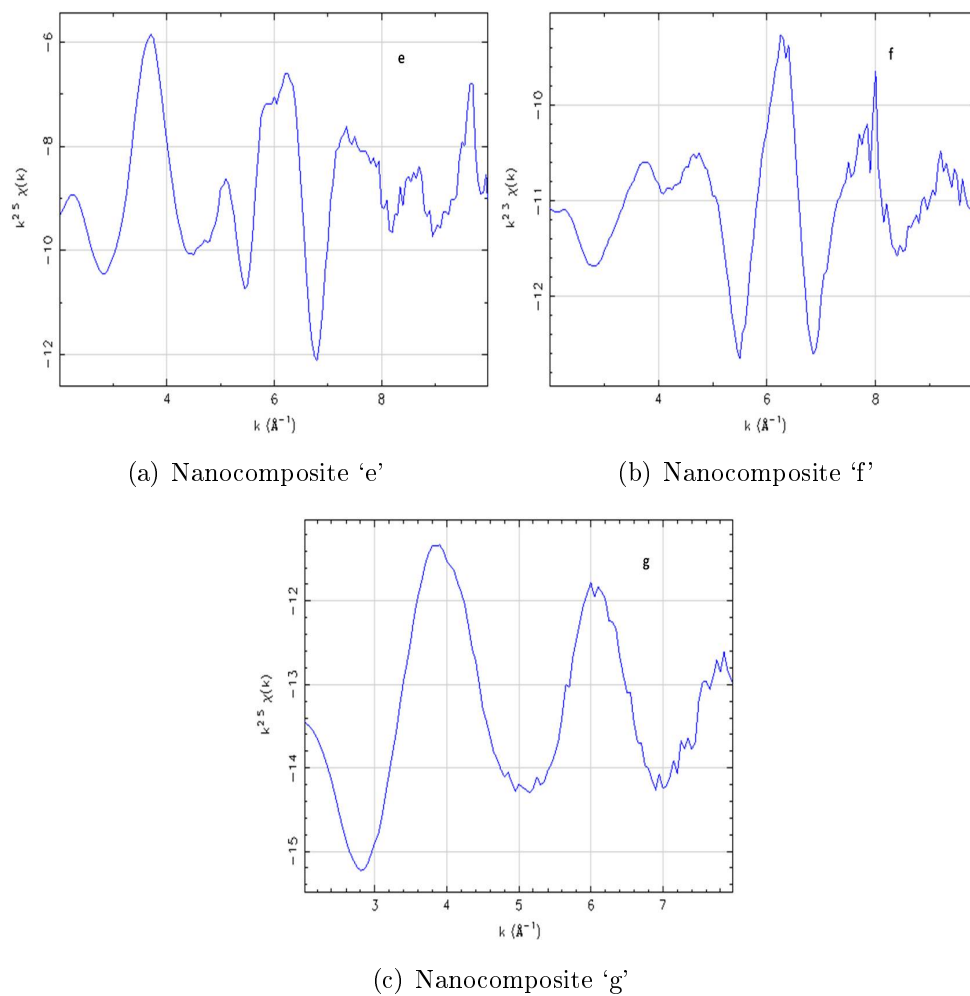


**Figure 4.26:** EXAFS function  $\chi(k)$  of Co–pp HMDSN nanocomposites e–g.

**Table 4.12:** FT peaks of Co–pp HMDSN nanocomposites e–g.

Nanocomposite	FT peaks (Å)
e	1.56, 2.54
f	2.10
g	1.44

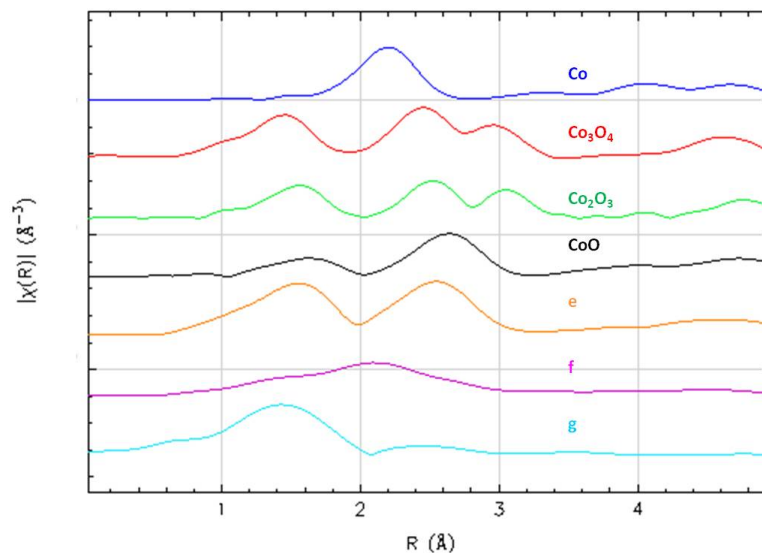


*Figure 4.27: RDF of cobalt standards and Co–pp HMDSN nanocomposites e–g.*

#### 4.2.6 Summary of XAS analysis

XRD and XPS analyses provided a little information about the nature of cobalt in the nanocomposites. However, XAS analysis demonstrated the nature of cobalt which could not be evidenced from the other techniques. The EXAFS and XANES analysis of the Co–ppHMDSN nanocomposites revealed the presence of metallic cobalt, cobalt oxide and a mixture of both. The structure of the nanocomposites is complex and it is difficult to distinguish between the contribution from metallic cobalt and cobalt oxides. However, the following conclusions can be made:

- With the increasing metal filling factor the metallic phase dominates over the oxide phase.
- With the decrease of distance between the target and substrate more amount of metallic cobalt is introduced, and the influence of oxygen is decreased.
- With the increase in the flow of HMDSN the amount of metallic cobalt is reduced.
- With the increase in flow of Ar there is more influence of oxygen.

## 4.3 Energy influx measurements using active thermal probe

An active thermal probe was used to study the plasma process and the interaction of plasma on the surface of the substrate. The variation of energy influx and power density with respect to time and magnetron power was measured in two plasmas: argon plasma and argon + HMDSN plasma.

### 4.3.1 Argon plasma

In this mode the chamber was only operated with the feed gas argon. Cobalt was sputtered at a constant flow of argon. The energy influx and power density were measured. The increase in flow of argon would only quantitatively increase the energy influx and power density values. Of course, qualitatively there would be little difference in the variation. Thus, the experiments were performed only at one flow of argon, i.e. at 1 sccm. The working pressure in the chamber was 0.024 mbar. Figure 4.28 depicts the measured heating power and power density of the active thermal probe in the argon plasma at a magnetron power of 100 W.

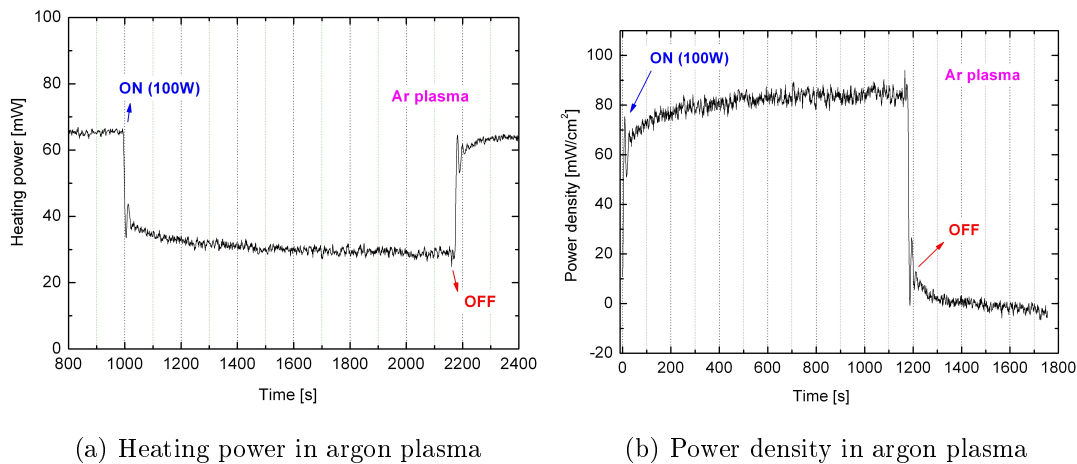


*Figure 4.28: Heating power and Power density in argon plasma measured by active thermal probe at a magnetron power of 100 W.*

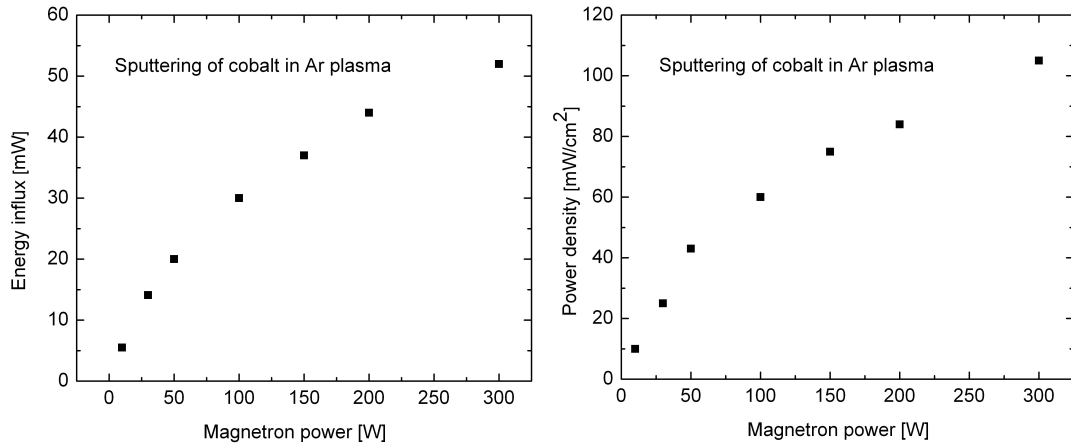
Figure 4.28 shows that when the plasma is switched ON the heating power supplied to the active thermal probe is reduced in order to compensate the increase in energy influx. The plasma is kept ON until there is a temperature balance, i.e. the

heating power is balanced. When the plasma is switched off the energy influx on the active probe gets reduced, and thus the heating power supplied to the probe is increased in order to keep the temperature constant. The change in the heating power is measured as the energy influx by the plasma. The temporal graph of power density in Figure 4.28 (b) shows the input power density on the surface of the active thermal probe starting from when the plasma is switched ON ( $t = 0$  s) till when it is switched OFF ( $t \sim 1200$  s). The power density value at the time when the plasma is switched ON is calculated by extrapolating the curve in Figure 4.28 (b) to  $t = 0$  s. For 100 W magnetron power in a pure argon plasma at a working pressure of  $\sim 0.024$  mbar this value is calculated to be  $\sim 60$  mW/cm<sup>2</sup>. The energy influx is calculated as the difference in the heating power (in Figure 4.28(a)) when the plasma is switched ON. This value is calculated to be  $\sim 30$  mW for 100 W power at 0.024 mbar pressure in a pure argon plasma.

The energy influx and power density values are calculated by varying the magnetron power from 10 W to 300 W and at the same flow of argon (or same working pressure) of  $\sim 0.024$  mbar. The variation of energy influx and power density with the variation of magnetron power in argon plasma is depicted in Figure 4.29. It shows an exponential increase in the energy influx with the increase in magnetron power. A similar trend is observed in the power density values. This increase is expected because with the rise in magnetron power more number of argon atoms get transformed into ions and radicals. Furthermore more such number of particles impinge on the substrate or the active thermal probe which eventually causes increase in the power density.

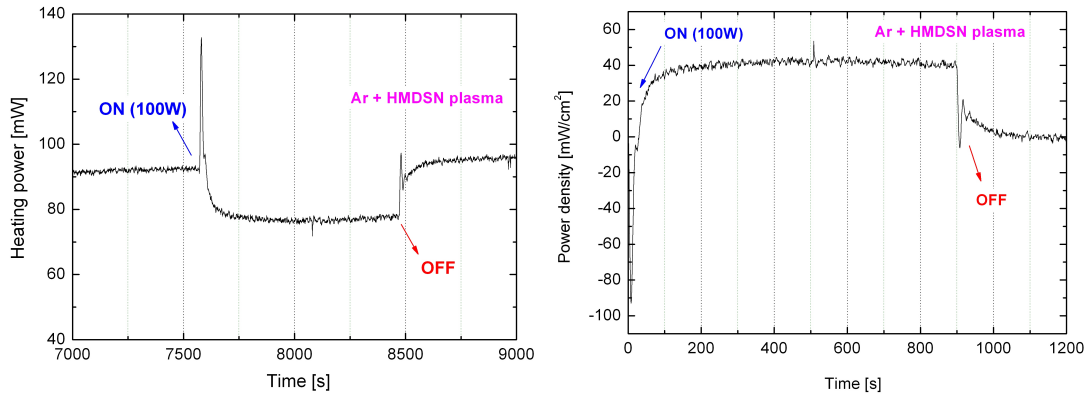
### 4.3.2 Argon + HMDSN plasma

In this mode the chamber is operated with both the feed gas argon and the monomer HMDSN. Cobalt was sputtered and HMDSN was simultaneously plasma polymerized. This represents the deposition of Co–ppHMDSN nanocomposites on the surface of the active thermal probe. The temporal change of energy influx and power density was measured. The increase in flow of argon would only quantitatively increase the energy influx and power density values. However, qualitatively there would be little difference in the variation. Thus, the experiments were performed only at one flow of argon, i.e. at 1 sccm. The flow of HMDSN was kept constant at 0.2 sccm. The working pressure in the chamber was 0.04 mbar. Figure 4.30 depicts the measured heating power and power density of the active thermal probe in argon + HMDSN plasma at a magnetron power of 100 W.



(a) Energy influx as a function of magnetron power in argon plasma (b) Power density as a function of magnetron power in argon plasma

**Figure 4.29:** Energy influx and power density as a function of magnetron power in argon plasma measured by active thermal probe.



(a) Heating power in argon + HMDSN plasma (b) Power density in argon + HMDSN plasma

**Figure 4.30:** Heating power and power density in argon + HMDSN plasma measured by active thermal probe at a magnetron power of 100 W.

In pure argon plasma exothermic reactions take place on the surface of the active thermal probe. This increases the energy influx due to external sources on the probe surface. The external control circuit decreases the heating power in order to compensate this increase in energy influx. This is what was observed in pure argon plasma in Figure 4.28. However, the types of reactions are different in argon + HMDSN plasma as shown

in Figure 4.30. When the plasma is switched ON a sharp increase in the heating power supplied by the external circuit is observed. This sharp peak is only for a very short duration. This means that the external circuit had to increase the heating power supplied to the probe. This suggests that an endothermic reaction has taken place on the probe surface. Thus, the probe surface has cooled down and is compensated by increase in the heating power which is shown by the sharp peak. The decomposition of the monomer and the methyl groups and the polymerization process requires energy. This is indicated by the endothermic reaction, i.e. the sharp peak in Figure 4.30.

A small peak is also observed when the plasma is switched off. Normally in an argon plasma (Figure 4.28), when the plasma is switched off, the external circuit increases the heating to the probe. That is because the energy input to the probe from the external plasma decreases. The same trend is also observed in argon + HMDSN plasma. An initial sharp peak is observed just when the plasma is switched off. This means that a little bit more heating power is supplied to the probe by the external circuit just when the plasma is switched off.

The power density is calculated by dividing the heating power with the area of the active probe and is displayed in 4.30 (b). As peaks are observed in the power density graph it is difficult to fit a curve to obtain the exact power density value when the plasma is switched ON.

In Figure 4.30 sharp peaks are observed when the plasma is switched on and off. Such peaks are always found in these cases. Figure 4.31 depicts the temporal variation of heating power and the various peaks observed when the plasma is switched on and off. The flow of HMDSN and argon is varied between ON1 and ON2 in order to study its influence on the heating power. The variation of argon and HMDSN as seen in between  $\sim 3000$ – $5000$  s does not seem to influence the heating power and does not cause any peaks. A detailed graph of heating power in the time range  $\sim 3000$ – $5000$  s is shown in Figure 4.32.

Figure 4.32 depicts that when the flow of HDMSN is kept zero and argon is varied no peaks are observed in the heating power. The peaks are only noticed when the plasma is switched on and off and when HMDSN is present. This implies that the peaks are due to the presence of HMDSN. It can be proposed that, when the plasma is switched on, some chemical reactions take place with respect to the monomer HMDSN so that there is an endothermic reaction at the active probe. Thus, in order to compensate the reduction in temperature the external circuit increases the heating power supplied to the probe. Furthermore, the variation of argon and HMDSN do not seem to be the

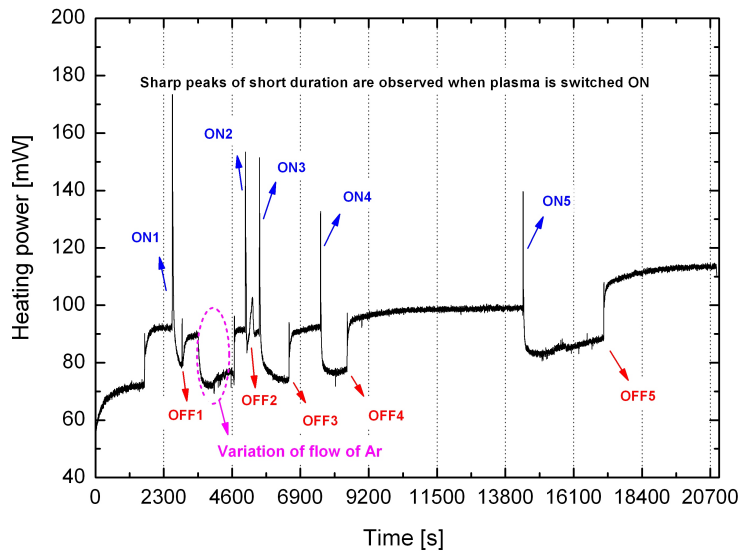


**Figure 4.31:** Heating power in argon + HMDSN plasma measured by active thermal probe at a magnetron power of 100 W. Several sharp peaks are seen when the plasma is switched on and off.

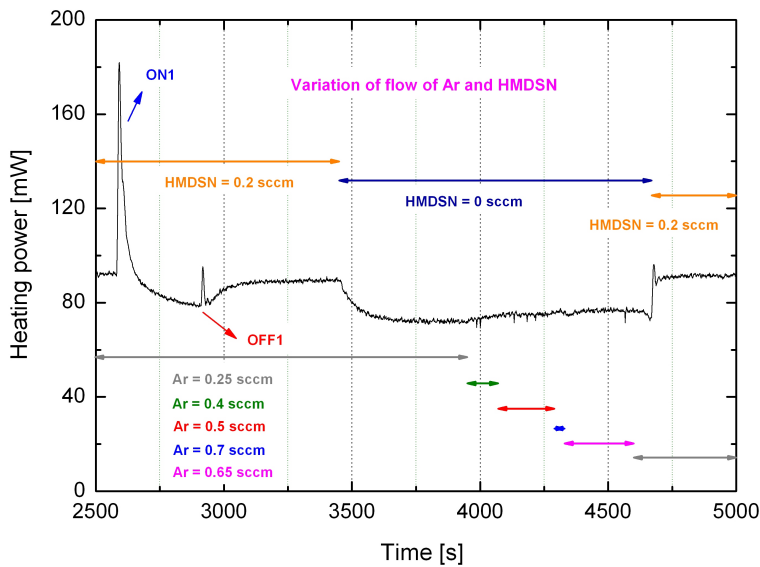


**Figure 4.32:** Heating power in argon + HMDSN plasma measured by active thermal probe at a magnetron power of 100 W. The influence of the variation of HMDSN and Ar is studied.

reason for the sharp peaks. But the reactions that happen when the plasma is switched ON causes the peaks.

A qualitative comparison between the energy influxes in argon (Figure 4.28) and argon + HMDSN plasmas (Figure 4.30) can be performed. Energy influx is measured as the difference of heating powers when plasma is switched on and off. For 100 W magnetron power in the pure argon plasma it was estimated to be 30 mW whereas in argon + HMDSN plasma it is 15 mW. Due to the presence of spikes it is not easy to estimate the exact value of energy influx in argon + HMDSN plasma when the plasma is switched on. However, the difference between the heating power levels when plasma was switched on and off can be considered as the energy influx. The energy influx is greater in pure argon plasma than in argon + HMDSN plasma. This suggests that during nanocomposite deposition more energy is consumed for monomer decomposition. Thus, active thermal probe measurements indicate that more energy is utilized in the argon + HMDSN plasma for the monomer decomposition when compared to pure argon plasma where no monomer was used. The thermal probe results show that the plasma reactions in a pure argon plasma are simple and straightforward. The energy influx and power density increase exponentially with the increase in magnetron power. But, during the nanocomposite preparation (i.e. in Argon + HMDSN plasma) spikes were observed when the plasma was switched ON and OFF. This suggested that the monomer decomposition and plasma polymerization processes influence the energy influx on the substrate surface. The active thermal probe measurements were performed in order to study the energy flux density in different plasma conditions (i.e. pure argon and argon + HMDSN plasmas). This would aid in a better understanding of the nanocomposite formation. The qualitative study pointed to lesser energy influx in argon + HMDSN plasma when compared to the argon plasma. This suggests that the monomer decomposition consumes some energy in the argon + HMDSN plasma. However, the thermal probe measurements illustrated complex reactions which made it difficult to determine the exact value of energy influx when plasma was switched on. A separate and in-depth study is required to shed further light on the matter. Nevertheless, the active thermal probe experiments performed in this work provide an example of how the study of a plasma process could be employed to understand the relation between energy influx and the nanocomposite film formation.



## 4.4 Conclusion

Cobalt–plasma polymerized HMDSN nanocomposites with varying metal filling factors were prepared by using RF magnetron sputtering of cobalt and simultaneous plasma polymerization of HMDSN monomer. TEM and XRD results indicate the presence of small, amorphous nanoparticles of size  $\sim 2\text{--}3$  nm at lower metal filling factor and crystalline nanoparticles of size  $\sim 6$  nm at higher metal filling factor. TEM micrographs reveal the homogeneous distribution of the nanoparticles in the polymer matrix. The composition of the polymer matrix determined by XPS and FTIR reveals a mixture of Si–O and Si–C bonds. The increase in metal filling factor correlates with the decrease in the amount of carbon and silicon. Cobalt is mostly oxidized in the nanocomposites. Additionally, the polymer matrix tends to get significantly modified with the increase in metal filling factor. The surface conductivity of the Co–ppHMDSN nanocomposites has been qualitatively studied using conductive AFM. The surface conductivity image of the nanocomposite at 34% metal filling factor shows the presence of conductivity. A thorough and in-depth XAS analysis of the nanocomposites was performed. The EXAFS and XANES analysis indicate the presence of metallic cobalt, cobalt oxide and a mixture of both. The local structure around cobalt seems complex and it was difficult to distinguish between the first and second coordination shells. Nevertheless, the variation of metallic cobalt and oxide content in the different nanocomposites could be qualitatively studied. A set of Co–ppHMDSN nanocomposites were prepared which are suitable as precursors for the next step of calcination. The calcinated cobalt–polymer nanocomposites were suggested for various magnetic, catalytic and gas sensor applications. Co–ppHMDSN nanocomposites as precursors for calcination are studied in detail as the functional properties of the calcinated sample depends on the precursors. It is also demonstrated that hybrid PVD/PECVD is a simple, easy and generalized technique to introduce finely dispersed metal nanoparticles in a polymer matrix. Active thermal probe was used to measure the energy influx and power density of the plasma in the reaction chamber. Active probe was employed in pure argon and argon + HMDSN plasmas. The energy influx measurements in pure argon plasma was quite straightforward. But, in argon + HMDSN plasma sharp peaks were observed when the plasma was switched on and off. This can be accounted to the various chemical reactions due to the monomer HMDSN. More energy was consumed by the argon + HMDSN plasma which can be accounted to the energy required by the monomer decomposition process.



## 5 $\text{Co}_3\text{O}_4$ – dielectric matrix nanocomposites

The Co–ppHMDSN nanocomposites with varying metal filling factor were used as precursors for the next step of calcination. The plasma process could not yield the desired spinel type cobalt oxide ( $\text{Co}_3\text{O}_4$ ) nanoparticles. The XRD patterns of Co–ppHMDSN nanocomposites depicted CoO nanoparticles (Figure 4.3) in the nanocomposite with 34% metal filling factor. In addition, the detailed XPS and XAS analysis investigations did not clearly provide the information about the exact oxide form of cobalt. Thus in order to obtain the required oxide of cobalt, the Co–ppHMDSN nanocomposites obtained from the hybrid PVD/PECVD process were annealed. Some groups performed such a similar annealing step to crystallize CoO to  $\text{Co}_3\text{O}_4$ . Guyon et al. [115] used cobalt nitrates in a plasma technique to prepare cobalt oxide thin films. After the plasma process, the deposited thin film was annealed at  $650^\circ\text{C}$  in air in order to eliminate nitrates and to obtain crystalline  $\text{Co}_3\text{O}_4$  nanoparticles. Similarly, Wang et al. [116] showed that in order to convert CoO to  $\text{Co}_3\text{O}_4$  it is essential to perform an annealing step at  $600^\circ\text{C}$  in air. It is also shown that annealing cobalt in air at a temperature of  $500^\circ\text{C}$  would yield spinel type cobalt oxide ( $\text{Co}_3\text{O}_4$ ) [117]. The literature indicates a calcination temperature range from  $500$ - $650^\circ\text{C}$  to obtain  $\text{Co}_3\text{O}_4$  phase. The aim of this study was to prepare  $\text{Co}_3\text{O}_4$ –matrix nanocomposites. Therefore, the choice of temperature is not significant when the end result of  $\text{Co}_3\text{O}_4$  phase is considered. Accordingly, in this work the Co–ppHMDSN nanocomposite precursors were calcinated at a randomly selected temperature of  $500^\circ\text{C}$  for 2 hours in air.

Phosphate ions are a major cause of water pollution. Research to develop new types of phosphate ion sensors is always growing. The motivation for this work was to develop a new type of optoelectrochemical phosphate ion sensor. Shimizu et al. [24] have already shown that  $\text{Co}_3\text{O}_4$  thin films display optoelectrochemical sensitivity to phosphate ions. Our aim was to prepare  $\text{Co}_3\text{O}_4$ –dielectric matrix nanocomposite thin films with better phosphate sensitivity when compared to the pure  $\text{Co}_3\text{O}_4$  thin films.

The increased sensitivity is expected due to the increase in the surface area of the  $\text{Co}_3\text{O}_4$  nanoparticles when embedded in the matrix. During calcination the agglomeration of the  $\text{Co}_3\text{O}_4$  nanoparticles is prevented by the matrix [27]. This reduces the grain size of  $\text{Co}_3\text{O}_4$  nanoparticles in the calcinated nanocomposite when compared to the pure  $\text{Co}_3\text{O}_4$  thin films. Thus the surface area is increased which in turn helps in increased sensitivity [7, 10, 12]. Additionally, by the process of calcination a porous structure is formed which helps in the increased migration of phosphate ions to reach the  $\text{Co}_3\text{O}_4$  nanoparticles [118]. The sensing properties of  $\text{Co}_3\text{O}_4$  nanostructures (such as nanosheets, nanorods) are more compared to the  $\text{Co}_3\text{O}_4$  agglomerated nanopowders as shown by Choi et al [119]. Thus, by preventing the agglomeration of the  $\text{Co}_3\text{O}_4$  nanoparticles an improved gas sensitivity was observed. Li et al. [120] showed that  $\text{Co}_3\text{O}_4$ –carbon nano tube nanocomposites display better gas sensing properties when compared to  $\text{Co}_3\text{O}_4$  thin films. Aggregation of  $\text{Co}_3\text{O}_4$  nanoparticles can be minimized by embedding them in a polymer or carbon to form nanocomposites [6, 121, 122].

Out of the prepared Co–ppHMDSN nanocomposites the one with the highest filling factor, i.e. 34%, was selected for the next step of calcination. This particular sample was chosen as it contained the highest amount of cobalt which would help in obtaining maximum sensitivity as phosphate sensor. In order to study the phosphate sensing properties of the  $\text{Co}_3\text{O}_4$ –dielectric matrix nanocomposites a standard  $\text{Co}_3\text{O}_4$  thin film was also prepared for comparison. The following section describes the characterization of both the  $\text{Co}_3\text{O}_4$ –dielectric matrix nanocomposite and  $\text{Co}_3\text{O}_4$  standard thin films. Moreover, the optoelectrochemical properties of these films in phosphate solutions of different concentrations were studied in detail.

## 5.1 Structural investigations

### 5.1.1 Structural analysis using XRD

The XRD patterns of the calcinated Co–ppHMDSN nanocomposite and  $\text{Co}_3\text{O}_4$  standard prepared on FTO substrates are shown in Figure 5.1. Figure 5.1(a) depicts the XRD pattern of the standard  $\text{Co}_3\text{O}_4$  thin film. The mean particle size calculated from the  $\text{Co}_3\text{O}_4$  reflections (220), (311), and (400) is about 12 nm. Additional peaks corresponding to the FTO substrate (denoted as S) are also observed in the XRD spectrum. The XRD spectrum of the calcinated Co–ppHMDSN nanocomposite is shown in Figure 5.1(b). After calcination, the oxide form of cobalt is converted from CoO to spinel type

$\text{Co}_3\text{O}_4$ . Thus, the desired spinel type  $\text{Co}_3\text{O}_4$  crystalline phase was achieved by calcinating the nanocomposite. The particle size was estimated using the pure physical line profile (Fourier transform method). The mean particle size calculated from the reflections (111), (220), and (311) is 3.5 nm which is less when compared to the mean size of 12 nm of  $\text{Co}_3\text{O}_4$  nanoparticles in the standard film. This means that the dielectric matrix helped in preventing the crystal growth of the nanoparticles. Thus the grain size of the nanoparticles is reduced by embedding them in a dielectric matrix. Similar results are also reported by Wang et al. [27].

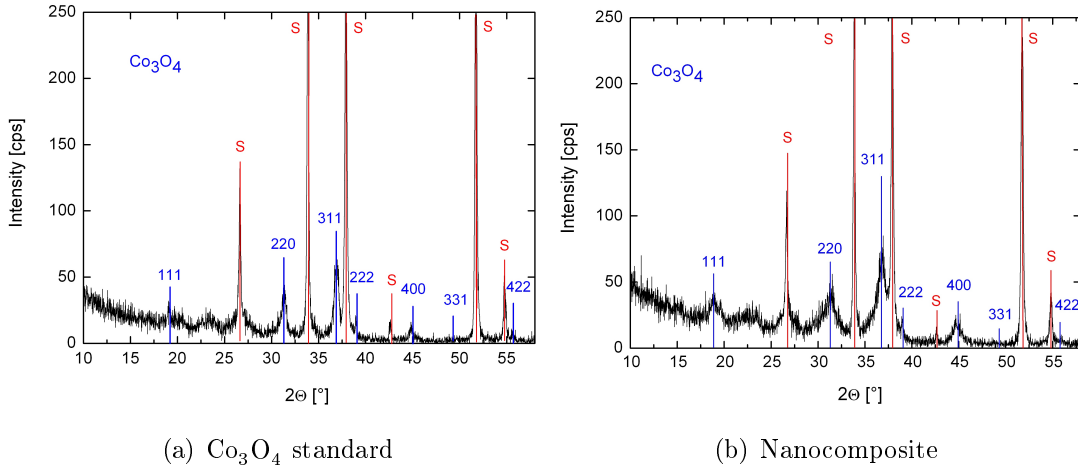


**Figure 5.1:** Grazing incidence XRD patterns ( $\omega = 0.5^\circ$ ) of a)  $\text{Co}_3\text{O}_4$  standard, b) Calcinated Co–pp HMDSN nanocomposite thin films. Peak corresponding to the FTO substrate are denoted as S.

### 5.1.2 Optical investigations using UV-Vis absorption spectroscopy

The UV-Vis absorption spectra (in air) of the standard and  $\text{Co}_3\text{O}_4$ –dielectric matrix nanocomposite thin films deposited on FTO substrates are depicted in Figure 5.2.

From profilometry the thicknesses of nanocomposite and standard were  $\sim 100$  nm. The optical absorption spectrum of the nanocomposite is similar to that of the  $\text{Co}_3\text{O}_4$  standard. Significant peaks are observed at  $\sim 450$  nm and  $\sim 750$  nm. These peaks indicate a spinel structure,  $\text{Co}_3\text{O}_4$  with the formation of  $\text{Co}^{3+}$  octahedral sites and  $\text{Co}^{2+}$  tetrahedral sites [8]. The UV-Vis optical absorption spectra confirm the results from XRD indicating the presence of spinel type  $\text{Co}_3\text{O}_4$  nanoparticles.

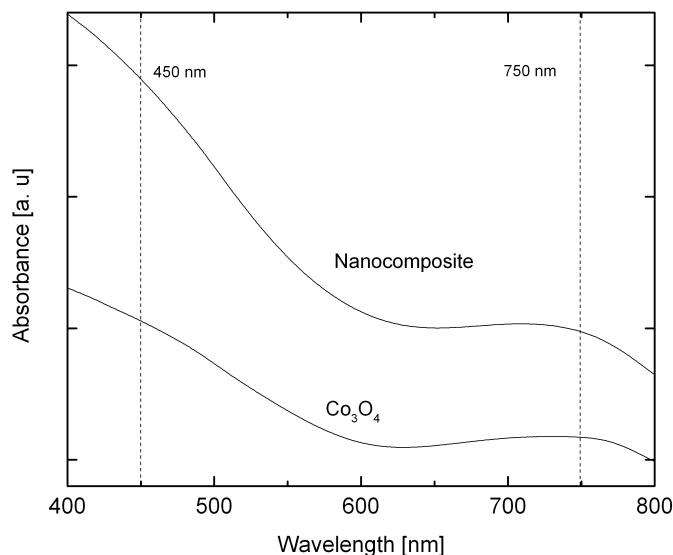


*Figure 5.2: Optical absorption spectra of  $\text{Co}_3\text{O}_4$  standard and  $\text{Co}_3\text{O}_4$  – dielectric matrix nanocomposite thin films in air.*

### 5.1.3 ATR-FTIR investigations

ATR-FTIR spectroscopy was performed in order to study the bonds present in the nanocomposite films. The ATR-FTIR spectrum is shown in Figure 5.3. There are many peaks observed in the FTIR spectrum. The broad peak from  $3500\text{--}3000\text{ cm}^{-1}$  is due to a combination of O–H stretching vibrations at  $\sim 3400\text{ cm}^{-1}$  and N–H stretching vibrations at  $\sim 3370\text{ cm}^{-1}$  [102]. The bands corresponding to C–C linkages are hidden in this broad band [115]. The noisy peaks at  $\sim 2300\text{ cm}^{-1}$  correspond to the atmospheric carbon dioxide. A zoomed in version of the FTIR spectrum at lower wavenumbers is shown in Figure 5.4.

The sharp, narrow band at  $\sim 680\text{ cm}^{-1}$  corresponds to Co–O bond stretching [115, 123]. The broad band at  $\sim 960\text{ cm}^{-1}$  can be interpreted in various ways. It can correspond to the Si–OH bonds [124–126]. Due to the broad width of the peak it can also correspond to Si–O bonds [125]. The small broad peak appearing as a shoulder at  $\sim 1100\text{ cm}^{-1}$  can correspond to the Si–O stretching vibrations [127]. Bonds corresponding to C–H vibrations were absent (at  $\sim 2900\text{ cm}^{-1}$ ). This is observed because these must have broken due to calcination. The analysis of the FTIR spectrum revealed the presence of various bonds such as Co–O, Si–O, Si–OH, O–H, N–H and C–C bonds in the nanocomposite thin films.

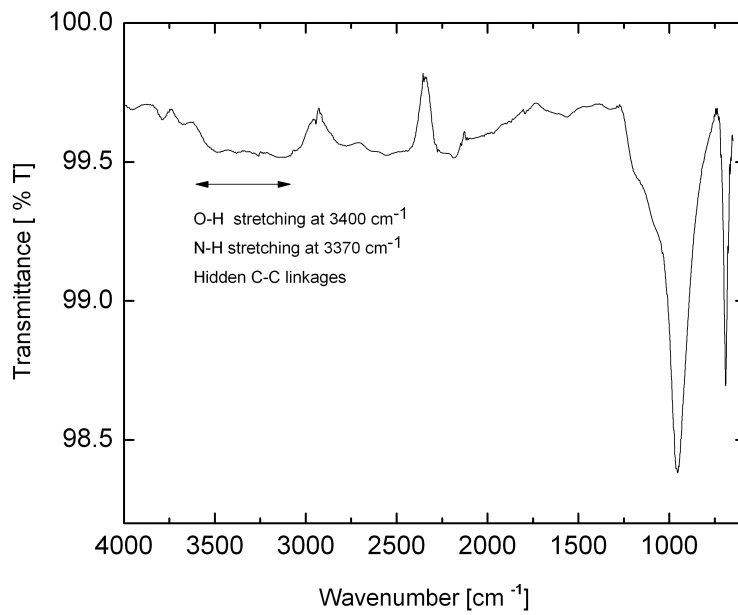


Figure 5.3: ATR-FTIR spectrum of  $Co_3O_4$ -dielectric matrix nanocomposite.

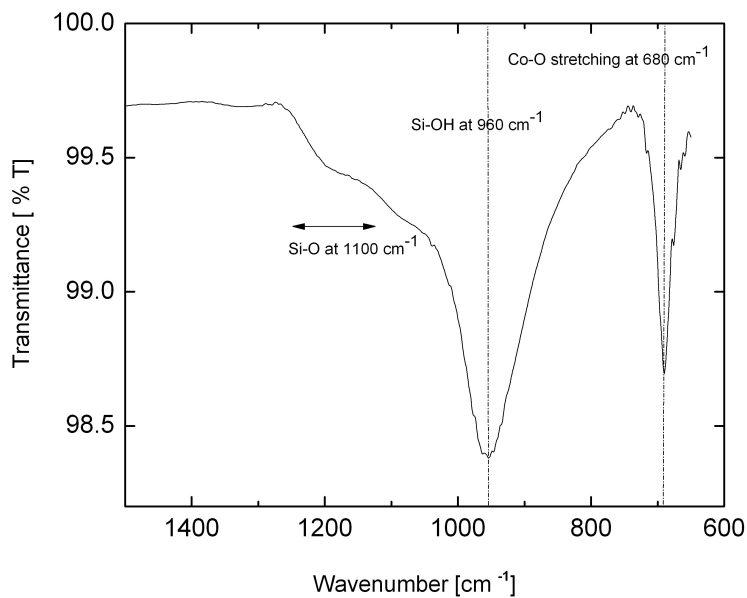
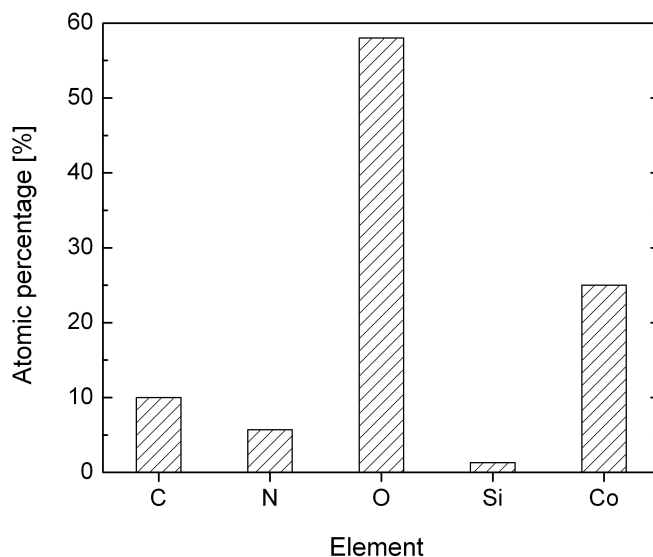


Figure 5.4: Zoomed in ATR-FTIR spectrum of  $Co_3O_4$ -dielectric matrix nanocomposite.

### 5.1.4 Elemental analysis using EDX

An EDX analysis was performed to estimate the atomic percentage of each element present in the nanocomposite. Figure 5.5 depicts the atomic percentage of elements present in  $\text{Co}_3\text{O}_4$  – dielectric matrix nanocomposite.



*Figure 5.5: EDX estimation of elemental atomic percentage of  $\text{Co}_3\text{O}_4$  – dielectric matrix nanocomposite.*

Figure 5.5 indicates that oxygen and cobalt possess large atomic percentages. There is also a considerable amount of carbon in the nanocomposite. When compared to the uncalcinated Co–ppHMDSN nanocomposite precursor (see Figure 4.8, 34% metal filling factor) the atomic percentage of carbon has not varied much. The large amount of carbon (due to the starting Co–ppHMDSN precursor) has remained even after calcination in air.

### 5.1.5 Surface analysis using SEM

SEM was used to study the surface of the nanocomposite films. Figure 5.6 presents the SEM micrographs of  $\text{Co}_3\text{O}_4$  – dielectric matrix nanocomposite thin films. The SEM micrographs depict the presence of cabbage-like structures. The nanocomposite film appears porous. The porosity can be attributed to the process of calcination. The development of porous structure after the annealing process is similar to the work previously reported [118, 128–130]. The porous structure aids in increased diffusion and



migration of the phosphate ions to reach the functional  $\text{Co}_3\text{O}_4$  nanoparticles. Thus, the reduced diffusion path and increased specific surface area results in faster chemical reactions. Consequently, the electrochemical performance of the nanocomposite increases. Indeed, the enhanced electrochromic performance of porous cobalt oxide thin films [131], porous NiO thin films [128] was reported previously.

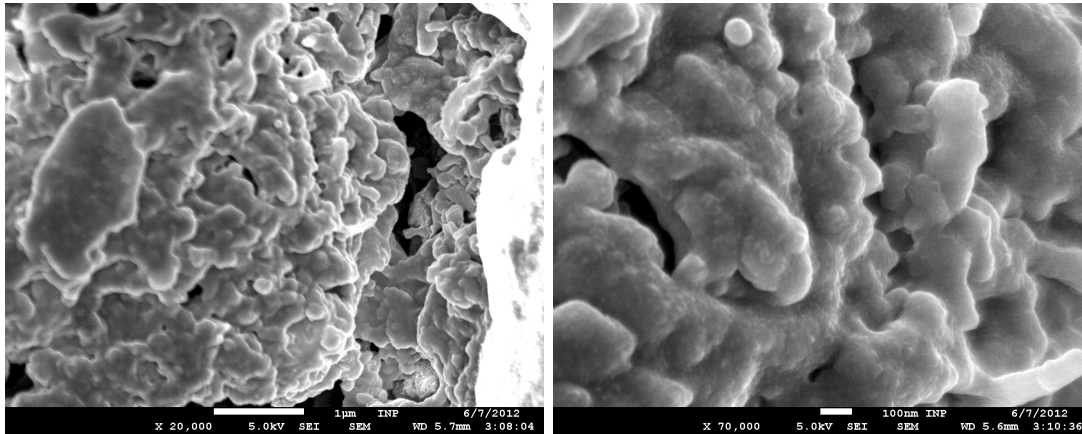


*Figure 5.6: SEM micrographs of  $\text{Co}_3\text{O}_4$ -dielectric matrix nanocomposite thin films. Scale is shown in the figure.*

### 5.1.6 Characterization summary

Co-ppHMDSN nanocomposites prepared by the plasma process could not yield the desired spinel type  $\text{Co}_3\text{O}_4$  phase. Therefore, a further annealing was performed. Co-ppHMDSN precursor with 34% metal filling factor was used as the precursor for calcination. After calcination crystalline cobalt oxide  $\text{Co}_3\text{O}_4$  nanoparticles of mean size  $\sim 3.5$  nm were obtained. XRD analysis and optical absorption spectra revealed the presence of crystalline  $\text{Co}_3\text{O}_4$  phase in the nanocomposite. FTIR spectrum depicted peaks corresponding to Si-O, and EDX elemental analysis showed a significant amount of carbon. Thus, the matrix can be interpreted as an amorphous, carbonaceous silicon oxide matrix (a-Si-O:C). The calcinated nanocomposite consists of  $\text{Co}_3\text{O}_4$  nanoparticles embedded in an amorphous Si-O:C matrix. The mean particle size of the  $\text{Co}_3\text{O}_4$  nanoparticles embedded in the dielectric matrix is less when compared to that of pure  $\text{Co}_3\text{O}_4$  thin films. This is because of the suppression of the increase of the grain size of the  $\text{Co}_3\text{O}_4$  nanoparticles by the surrounding dielectric matrix. With decreased grain

size the surface area of the Co<sub>3</sub>O<sub>4</sub> nanoparticles increases which aids in improving the electrochemical performance. Moreover, the calcination procedure resulted in a porous structure.

The high porosity structure is beneficial in improving the reaction kinetics by decreasing the path of diffusion and increasing the surface area for reaction. When the Co<sub>3</sub>O<sub>4</sub> – dielectric matrix nanocomposites are tested as phosphate sensors an increased sensitivity to the phosphate ions is expected. This is because of the increase in surface area of the Co<sub>3</sub>O<sub>4</sub> nanoparticles embedded in the dielectric matrix when compared to Co<sub>3</sub>O<sub>4</sub> nanoparticles in pure Co<sub>3</sub>O<sub>4</sub> thin film. Thus, Co<sub>3</sub>O<sub>4</sub> – dielectric matrix nanocomposite thin films and Co<sub>3</sub>O<sub>4</sub> thin films were prepared on FTO substrates which were further tested as optoelectrochromic phosphate sensors. The pure Co<sub>3</sub>O<sub>4</sub> thin film was prepared to compare its performance as a standard with the Co<sub>3</sub>O<sub>4</sub> – dielectric matrix nanocomposite.

## 5.2 Optoelectrochemical properties - phosphate ion sensor

The synthesized Co<sub>3</sub>O<sub>4</sub> – dielectric matrix nanocomposite thin films were tested for their optoelectrochemical properties. The electrochemical properties were investigated in a three electrode electrochemical cell. The optical properties were studied using a spectrophotometer. The optoelectrochromic properties were investigated by applying potential to the nanocomposite and simultaneously observing the optical properties. Electrochromism is the process of reversible change in optical transmittance of a material upon the application and removal of potential. The reversible optical response of electrochromic sensors are based on electrochemical oxidation and reduction reactions [132].

Optoelectrochromic measurements were carried out in Na<sub>2</sub>HPO<sub>4</sub> solutions of different concentrations: 10<sup>-6</sup> M, 10<sup>-5</sup> M, 10<sup>-4</sup> M, 10<sup>-3</sup> M, 10<sup>-2</sup> M. Initially the optical transmittance of the nanocomposite thin film was measured at zero applied potential. The spectra were measured in the wavelength range of 400 to 800 nm. An initial change in the transmittance with respect to the phosphate concentration was observed. But, with the application of potential there was a significant change in the transmittance. Moreover, the change was dependent on the applied potential. Potentials of 0.2 V, 0.4 V, 0.6 V, 0.8 V vs Ag/AgCl were applied to the Co<sub>3</sub>O<sub>4</sub> – dielectric matrix nanocomposite thin film. Figure 5.7 shows the variation of optical transmittance in 10<sup>-3</sup> M Na<sub>2</sub>HPO<sub>4</sub>

solution with the application of potential.

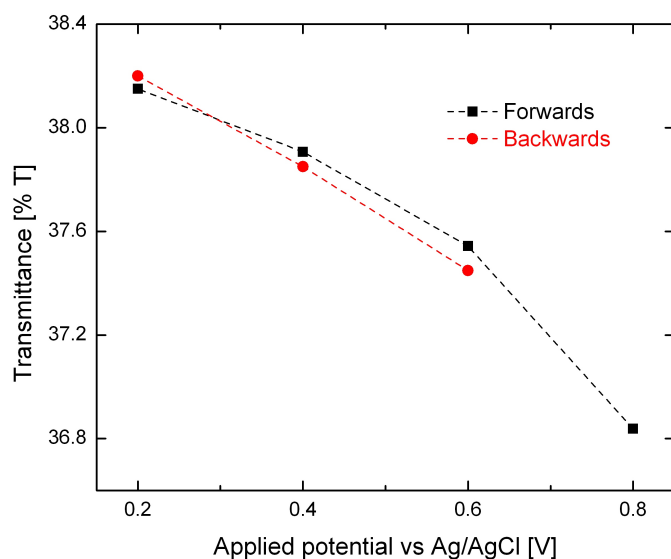
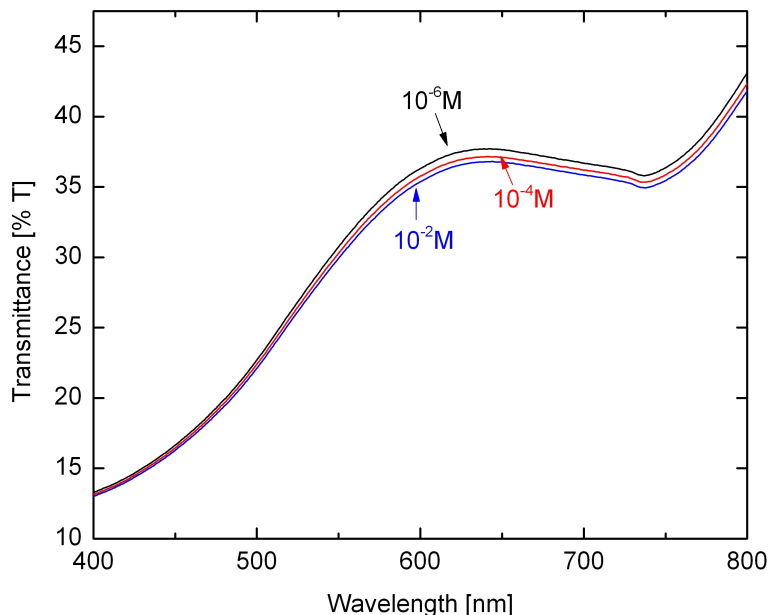


**Figure 5.7:** Optical transmittance values of  $\text{Co}_3\text{O}_4$ -dielectric matrix nanocomposite thin film at different applied potentials in  $10^{-3}$  M  $\text{Na}_2\text{HPO}_4$  solution. The transmittance values are reversible and reproducible upon the application and removal of potential. ‘Forwards’ indicates increase and ‘Backwards’ indicates decrease in applied potential respectively.

As the applied potential increases the film becomes darker and the transmittance value is decreased. The maximum change in transmittance was found at an applied potential of 0.8 V vs Ag/AgCl. The potential was not increased beyond the value of 0.8 V vs Ag/AgCl as too high potential can cause damage to the electrochemical cell and the reference Ag/AgCl electrode. When the applied potential was reversed, i.e. when it was reduced from 0.8 V vs Ag/AgCl to 0.2 V vs Ag/AgCl the optical transmittance values were reproducible and reversible. This demonstrates an interesting electrochromic property of the  $\text{Co}_3\text{O}_4$ -dielectric matrix nanocomposite thin films. The response is reversible as the increase of voltage makes the film darker, and decrease of voltage brings the original colour to the film. This means that the film is stable and exhibits electrochromic properties in phosphate solutions. Such reproducible and reversible phosphate sensing properties were observed also in  $\text{Na}_2\text{HPO}_4$  solutions of other concentrations. Thus, the prepared  $\text{Co}_3\text{O}_4$ -dielectric matrix nanocomposite films exhibited an electrochromic property in the phosphate solutions.

As a further step, the applicability of the  $\text{Co}_3\text{O}_4$ -dielectric matrix nanocomposite thin films as phosphate sensors over a range of phosphate concentrations was tested.

The potential at which the maximum change in transmittance occurred, i.e. 0.8 V vs Ag/AgCl, was applied to the cell containing phosphate solutions of different concentrations. The transmittance spectra in different  $\text{Na}_2\text{HPO}_4$  concentrations at an applied potential of 0.8 V vs Ag/AgCl is depicted in Figure 5.8.



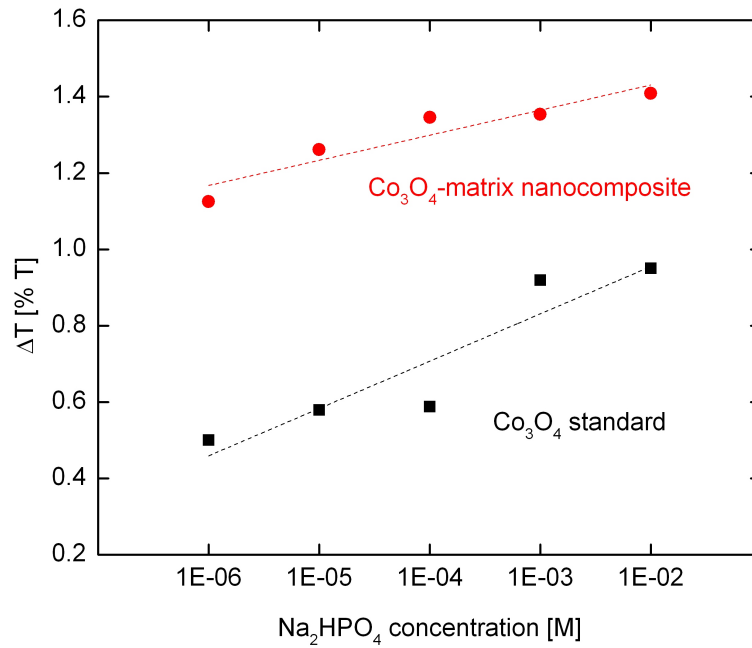
**Figure 5.8:** Transmittance spectra of  $\text{Co}_3\text{O}_4$  – dielectric matrix nanocomposite thin film at three different  $\text{Na}_2\text{HPO}_4$  concentrations at an applied potential of 0.8 V vs Ag/AgCl.

Figure 5.8 displays that with the increase in phosphate concentration the transmittance decreases. The transmittance spectra dependence on the phosphate concentration is similar to the work reported by Shimizu et al. [24] who showed that pure  $\text{Co}_3\text{O}_4$  thin films deposited on ITO substrate exhibit optoelectrochromic sensitivity to phosphate ions. Following their work this dissertation aims to develop a new type of phosphate sensor based on  $\text{Co}_3\text{O}_4$  – dielectric matrix nanocomposite thin film. By embedding the  $\text{Co}_3\text{O}_4$  nanoparticles in a matrix an improved optoelectrochromic performance is expected. In the case of  $\text{Co}_3\text{O}_4$  – dielectric matrix nanocomposites, Figure 5.8 shows that the change in transmittance below 550 nm was not much significant. But the region between 550 and 800 nm displays an appreciable change. Moreover, this change in transmittance was dependent on the phosphate concentration. This property could make the  $\text{Co}_3\text{O}_4$  – dielectric matrix nanocomposite thin films a suitable choice for optoelectrochemical phosphate ion sensors. The wavelength at which maximum change in transmittance occurred was observed at 620 nm.

To characterize the  $\text{Co}_3\text{O}_4$ –dielectric matrix nanocomposites as phosphate ion sensors the change in transmittance at 620 nm of the nanocomposite was plotted against the phosphate concentration. Figure 5.9 depicts the change in transmittance ( $\Delta T$ ) versus the concentration of phosphate solutions. Each data point of  $\Delta T$  is normalized to the transmittance value at 0 V.  $\Delta T$  is calculated as the difference of  $T_{0V}$  and  $T_{0.8V}$  at 620 nm at each  $\text{Na}_2\text{HPO}_4$  concentration.  $T_{0V}$  corresponds to the optical transmittance value at 0 V, i.e. no applied potential and  $T_{0.8V}$  corresponds to the transmittance value at 0.8 V vs Ag/AgCl.

In order to compare the performance of  $\text{Co}_3\text{O}_4$ –dielectric matrix nanocomposite with the standard  $\text{Co}_3\text{O}_4$  thin film, the whole experiment was repeated for  $\text{Co}_3\text{O}_4$  thin films. The graph of  $\Delta T$  versus  $\text{Na}_2\text{HPO}_4$  concentration for the standard  $\text{Co}_3\text{O}_4$  thin film is also presented in Figure 5.9. The linear fits of the curves are also depicted. With the logarithmic increase in  $\text{Na}_2\text{HPO}_4$  concentration  $\Delta T$  rises almost linearly for both the nanocomposite and the  $\text{Co}_3\text{O}_4$  standard. The sensitivity of the  $\text{Co}_3\text{O}_4$  standard at lower concentrations was not much appreciable. But on a whole, the increase of  $\Delta T$  with the increase in concentration was observed for the  $\text{Co}_3\text{O}_4$  standard. In the case of nanocomposite, the linear dependence of  $\Delta T$  on the logarithm of  $\text{Na}_2\text{HPO}_4$  concentration indicates that the  $\text{Co}_3\text{O}_4$ –dielectric matrix nanocomposite can be applicable as a novel type of optoelectrochromic phosphate ion sensor. To determine the sensitivity of the thin film sensors, the slope of the graph was calculated [133]. For the nanocomposite it was  $\sim 0.03$  Abs/dec. For the standard the fitted line was not satisfactory owing to the slight non-linearity of the points. Nevertheless, the calculated sensitivity for the standard was  $\sim 0.05$  Abs/dec which is a little more than the nanocomposite. Even though the sensitivities across the concentrations could not be satisfactorily compared, the value of absolute transmittance signal ( $\Delta T$ ) at a particular concentration is higher for the nanocomposite when compared to the standard. In this sense, it can be said that the nanocomposite has more absolute transmittance signal when compared to the standard. This observation presents an enhanced phosphate sensor at a particular phosphate concentration when compared to standard  $\text{Co}_3\text{O}_4$ . It has to be noted that  $\Delta T$  was calculated as the difference of  $T$  at 0 V and 0.8 V applied potential. Moreover, the thickness of both the nanocomposite and standard films was almost the same. This ensures that the comparison of  $\Delta T$  at a particular concentration of both the films is sensible. By embedding  $\text{Co}_3\text{O}_4$  nanoparticles in a matrix a reduced grain size (3.5 nm) was obtained when compared to the grain size of the standard  $\text{Co}_3\text{O}_4$  thin film (12 nm). The matrix has performed an important role in suppressing the agglomeration of  $\text{Co}_3\text{O}_4$

nanoparticles. Thus, reducing the grain size. The surface area of the  $\text{Co}_3\text{O}_4$  nanoparticles is significantly increased due to the reduction of the grain size, and increased surface area helps in enhancement of the electrochemical response. Moreover, with the process of calcination a porous structure has formed which improves the probability of diffusion of phosphate ions to the functional  $\text{Co}_3\text{O}_4$  species. Consequently, the porous structure can help in the improvement of the kinetics of reaction.



**Figure 5.9:** Plot of  $\Delta T$  vs  $\text{Na}_2\text{HPO}_4$  concentration of  $\text{Co}_3\text{O}_4$ –dielectric matrix nanocomposite and  $\text{Co}_3\text{O}_4$  standard thin films together with the fits.  $\Delta T = T_{0V} - T_{0.8V}$

## 5.3 Conclusion

Co-ppHMDSN nanocomposite precursor with 34% metal filling factor was calcinated to obtain  $\text{Co}_3\text{O}_4$ -a-Si-O:C nanocomposite. The mean particle size of the  $\text{Co}_3\text{O}_4$ -dielectric matrix nanocomposite was  $\sim 3.5$  nm when compared to the mean particle size of  $\sim 12$  nm of the  $\text{Co}_3\text{O}_4$  standard. Particle aggregation was prevented by the dielectric matrix which reduced the grain size. FTIR spectrum revealed peaks from Si-O, Co-O and C-C bonds. Additionally, EDX analysis showed the presence of Co, O, C, N, and Si. The matrix consists of amorphous carbonaceous silicon oxide. SEM micrographs revealed a porous structure.  $\text{Co}_3\text{O}_4$ -dielectric matrix nanocomposite films displayed sensitivity towards phosphate ions. A linear sensitivity to the logarithm of  $\text{Na}_2\text{HPO}_4$  concentration was observed. At a particular phosphate concentration, the  $\text{Co}_3\text{O}_4$ -dielectric matrix nanocomposite thin films exhibited more absolute transmittance signal ( $\Delta T$ ) when compared to the standard  $\text{Co}_3\text{O}_4$  thin film. A novel phosphate ion sensor which is sensitive enough to detect environmental level phosphate ion concentration ( $10^{-6}$  M) was proposed. The results indicate the potential for an improved sensor.





## 6 Summary

Cobalt–plasma polymerized HMDSN nanocomposite thin films with varying metal filling factors were prepared using a simple and easy hybrid PVD/PECVD process. The microstructural, physical, chemical and surface conductivity properties of the nanocomposites were studied in detail. The fundamental study of Co–ppHMDSN nanocomposites was presented.

Well dispersed Co–ppHMDSN nanocomposites with metal filling factors varying from 4% to 34% were prepared. The variation of the properties of the nanocomposites in correlation to the metal filling factor was studied. The morphology investigated using TEM indicated the size of the nanoparticles to be 2–3 nm at lower filling factor and 6 nm at higher filling factor. The TEM micrographs depict a homogeneous and narrow distribution of the nanoparticles. XRD analysis supported the TEM results and indicated amorphous nanoparticles at lower filling factors and crystalline nanoparticles at higher filling factors. EDX and profilometry were employed to determine the metal filling factor. Cobalt is mostly oxidised in the nanocomposites. The presence of oxygen is also seen from the EDX results. It has to be noted that the process of hybrid PVD/PECVD was carried out at a pressure of  $\sim 3.8$ –18 Pa. This high pressure, the rough vacuum conditions, and the water molecules deposited on the walls of the reaction chamber accounted for the presence of oxygen. As a result, the influence of oxygen is observed in the nanocomposites as evidenced from the XRD (CoO phase), FTIR (Si–O bonds), and EDX results. HMDSN was used as the monomer precursor for polymerization. When the plasma is switched ON the monomer HMDSN gets dissociated into reactive fragments of high energy. Plasma polymerization proceeds when these fragments hit the target with high energy and recombine to form a plasma polymerized film on the substrate [134]. As both PVD and PECVD processes occur simultaneously in the chamber, they are inter-dependent and affect each other. The deposition of cobalt and the plasma polymerization of HMDSN are affected by various factors such as the magnetron power, the pressure in the chamber, reactor geometry, distance between the target and substrate and the flow of gases. The polymer matrix was characterized using XPS and FTIR. It

was significantly modified with the increase in the filling factor. Distinct Si–C, Si–N and Si–O peaks were observed in pure plasma polymerized HMDSN thin film. However, the FTIR spectra of the nanocomposites lack distinct peaks indicating a mixture of Si–O and Si–C bonds in the polymer matrix. For the phosphate sensor application, the nature of the polymer matrix and the oxidation state of cobalt are not significant as the process of calcination would yield  $\text{Co}_3\text{O}_4$  nanoparticles embedded in a matrix.

XRD and TEM analyses revealed that by varying the plasma parameters it is possible to obtain nanocomposites with varying metal filling factors and nanoparticle size distributions. The chemical structure of the deposited polymer film is dependent on various plasma parameters such as the power density, reactor geometry and the dissociation of the monomer. From the XPS and FTIR spectra it can be inferred that the polymer matrix contains a mixture of Si–O and Si–C bonds. Higher magnetron power was used to deposit nanocomposites with higher filling factor. Consequently, the energy in the plasma increases which increases the bombardment of particles and the number of collisions per volume. Subsequently, the dissociation of the bonds in the polymer matrix becomes higher. As a result, the Si–N, N–H, and  $\text{CH}_3$  bonds tend to get more dissociated with the increase in filling factor as more magnetron power was used at higher filling factors. Furthermore, the influence of water vapor is seen in all nanocomposites as confirmed by the peak at  $1000\text{ cm}^{-1}$  corresponding to Si–O vibrations. Moreover, the FTIR spectra of Co–ppHMDSN nanocomposites lack distinct peaks because of the overlap of peaks due to Si–C and Si–O bonds. The oxygen content of the nanocomposites increases with increasing filling factor as the peak at  $\sim 1000\text{ cm}^{-1}$  shifts to higher frequencies. Also the decrease of peak intensity at  $\sim 1256\text{ cm}^{-1}$  corresponding to C–H vibrations indicates that nanocomposites with higher filling factor are free of C–H groups [58]. Even though the polymer matrix is significantly modified with increasing metal filling factors the matrix is dominated by the presence of Si–O and Si–C bonds.

The x-ray amorphous nature of cobalt in the Co–ppHMDSN nanocomposites was observed. XRD patterns revealed that cobalt is mostly amorphous in almost all Co–ppHMDSN nanocomposites. X-ray absorption spectroscopy (XAS) was employed to study the local structure around cobalt in detail. XAS is a technique which can be used to study amorphous, low or no crystalline samples. Co–ppHMDSN nanocomposites prepared at different plasma parameters were analyzed using XAS. XANES analysis revealed the information about the valency of cobalt in the nanocomposites. XANES spectra of the nanocomposites were compared to that of the standards Co, CoO,  $\text{Co}_2\text{O}_3$ ,  $\text{Co}_3\text{O}_4$ . Parameters such as the rise of the pre-edge before the absorption edge, pre-

---

edge features, XANES peaks, the shift of the absorption edge, and the shape of the XANES spectra were used to obtain local structure information and chemical configuration of cobalt. EXAFS analysis was performed to obtain information about the nature and number of neighbours around the absorbing cobalt atom. The radial distribution functions (RDF) (obtained after Fourier transformation) or the Fourier transform plots of the Co–ppHMDSN nanocomposites were compared to the standards. Distinctive peaks corresponding to specific standard could not be identified. The peaks in RDF of the nanocomposites comprised of a combination of peaks from one or more standards. As the Fourier transform plots of the nanocomposites were complex, it was difficult to distinguish between the first and second coordination shells. Consequently, determination of the exact composition of the first and second coordination shells around cobalt atom was not simple. However, the presence of both metallic cobalt and cobalt oxides was observed in all nanocomposites. But the overlap area of the peaks with different standards was not the same for all nanocomposites. The difference in the number of peaks, the amount of overlap with the peaks of standards, the shapes of the radial distribution function can be used to distinguish various properties of different Co–ppHMDSN nanocomposites. Even though the structure of the nanocomposites is complex, an in-depth study of XANES and EXAFS spectra, a careful study of the variation of spectra among different nanocomposites, and a comparison of XANES and EXAFS spectra gave some valuable information about the local structure of cobalt in the nanocomposites. For example, with rising metal filling factor the metallic content of the nanocomposites increased which could not be observed from other analyses like XRD and TEM. Similarly, with the decrease of distance between substrate and target the amount of metallic cobalt increased. The increase in the flow of gases or monomer reduced the amount of metallic cobalt. Thus, a detailed XAS analysis of the Co–ppHMDSN nanocomposites was performed to understand exactly the local structure around cobalt and also the oxidation state of cobalt. As much of the cobalt was amorphous the XAS technique indeed proved very useful for the qualitative structural investigations.

It is emphasized here that Co–ppHMDSN nanocomposites with varying cobalt concentrations are suitable as precursors for calcinated cobalt–polymer nanocomposites [13]. Even though cobalt is partly oxidized in the Co–ppHMDSN nanocomposite precursors, the further step of calcination would completely oxidize the cobalt nanoparticles. Therefore, the oxidation state of cobalt in the precursors is not important. It is significant that the Co–ppHMDSN nanocomposites precursors have well-dispersed cobalt nanoparticles with varying amount of cobalt which is clearly indicated by the

TEM and EDX results. The ability to disperse finely the cobalt nanoparticles in the polymer matrix and the variation of the metal filling factors are important for Co–ppHMDSN nanocomposites as precursors for the next step of calcination [8]. For the calcinated cobalt–polymer nanocomposites it is not significant to have a good control over the properties of the polymer matrix of the precursor. The polymer matrix is used to prevent agglomeration of the cobalt nanoparticles and hence, the variation of polymer matrix is not important when using Co–ppHMDSN nanoparticles as precursors for calcination. Using the simple and easy method of hybrid PVD/PECVD with only one magnetron source for metal sputtering, simultaneous plasma polymerization of monomer and without the use of high vacuum conditions it is demonstrated that finely dispersed metal–polymer nanocomposites with varying metal filling factors can be prepared. A generalized method to introduce finely dispersed cobalt nanoparticles in a polymer matrix is presented which can be used as precursor for the next step of calcination.

During this dissertation work an attempt was made to study the energy influx of the plasma process on the substrate surface. Indeed, it is important to consider the interaction of the plasma with the substrate. The morphological and structural properties are dependent on the power density on the substrate surface. Two different kinds of plasma were considered for the energy influx study. A pure argon plasma and an argon + HMDSN plasma were investigated using an active thermal probe. In the case of pure argon plasma, the energy influx increased exponentially with the increase in magnetron power. This can be a consequence of the increased number of active species (ions and radicals) in the plasma. However, the relationship between energy influx and magnetron power was not simple in the argon + HMDSN plasma. The heating power curve in the argon + HMDSN plasma (see Figure 4.30) illustrates sharp peaks when the plasma was switched on and off. The peaks could be ascribed to the decomposition of HMDSN monomer and the chemical reactions on the substrate surface. A qualitative comparison between the two plasmas indicated that more energy was consumed by the argon + HMDSN plasma. This maybe because of the energy required by the monomer dissociation process.

The prepared Co–ppHMDSN nanocomposites contained both metallic cobalt and cobalt oxides (as evidenced by XRD, XPS, and XAS analyses). The motivation for this work was to develop a new type of cobalt/cobalt oxide–polymer/dielectric matrix nanocomposite system and to test the applicability as phosphate ion sensors. The sensing mechanism employed was similar to that of Shimizu et al. [24]. Accordingly,

---

an optoelectrochemical method was used. Shimizu et al. [24] described the phosphate sensing properties of  $\text{Co}_3\text{O}_4$  thin films deposited on conductive indium tin oxide (ITO) substrates. In this work,  $\text{Co}_3\text{O}_4$ –dielectric matrix nanocomposite thin films were proposed as phosphate sensors. Moreover, an increased sensitivity of the nanocomposite when compared to the pure  $\text{Co}_3\text{O}_4$  standard is expected. As the required spinel type cobalt oxide ( $\text{Co}_3\text{O}_4$ ) could not be obtained by the plasma process, calcination of Co–ppHMDSN nanocomposites was performed to obtain crystalline  $\text{Co}_3\text{O}_4$  phase. The process of calcination resulted in  $\text{Co}_3\text{O}_4$  nanoparticles embedded in an amorphous, carbonaceous silicon oxide (a-Si–O:C) matrix. XRD analysis revealed crystalline  $\text{Co}_3\text{O}_4$  nanoparticles of mean size  $\sim 3.5$  nm in the nanocomposite film and a mean size of  $\sim 12$  nm in the  $\text{Co}_3\text{O}_4$  standard film. The matrix helped in the prevention of aggregation of the  $\text{Co}_3\text{O}_4$  nanoparticles during calcination. Consequently, the grain size of  $\text{Co}_3\text{O}_4$  nanoparticles decreased by embedding them in a matrix. As a result, the surface area of the  $\text{Co}_3\text{O}_4$  nanoparticles is more in the nanocomposite when compared to the  $\text{Co}_3\text{O}_4$  standard film. Therefore, an increased electrochemical activity and subsequently, an improved phosphate sensing activity can be expected. There is a large influence of carbon in the uncalcinated sample. The presence of carbon was also observed after calcination. In addition, calcination would develop porous structures facilitating more space for faster diffusion of phosphate ions to reach the functionally active  $\text{Co}_3\text{O}_4$  species. Furthermore, it was observed that calcinated films possess greater mechanical stability in the phosphate solutions when compared to the uncalcinated films.

A detailed structural investigation of the  $\text{Co}_3\text{O}_4$ –dielectric matrix nanocomposite films was performed before testing the optoelectrochemical properties. This is to ensure the presence of a crystalline  $\text{Co}_3\text{O}_4$  phase. Additional investigations revealed the properties of increased surface area of  $\text{Co}_3\text{O}_4$  nanoparticles and the greater mechanical stability of the  $\text{Co}_3\text{O}_4$ –dielectric matrix nanocomposite films. Different potentials were applied to the nanocomposite film to determine the potential at which maximum change in transmittance occurred. The transmittance values were reproducible as the potentials were applied and reversed. A reversible and reproducible electrochromism was observed in the  $\text{Co}_3\text{O}_4$ –dielectric matrix nanocomposite thin films. The reproducibility and reversibility confirm the stability of the nanocomposite films even under the application of potential. The nanocomposite film displayed the required electrochromic sensing property in  $\text{Na}_2\text{HPO}_4$  solutions of various concentrations. The potential at which the maximum change of transmittance occurred (0.8 V vs Ag/AgCl) was chosen for further studies. As the next step, the nanocomposite thin films were tested for the

applicability as phosphate ion sensors. Furthermore, a  $\text{Co}_3\text{O}_4$  standard film was also tested for the purpose of comparison. The change in transmittance ( $\Delta T$ ) at 0.8 V vs Ag/AgCl with respect to the transmittance at 0 V was measured at different  $\text{Na}_2\text{HPO}_4$  concentrations. The linear dependence of  $\Delta T$  on the logarithm of  $\text{Na}_2\text{HPO}_4$  concentration demonstrates the applicability of the  $\text{Co}_3\text{O}_4$ –dielectric matrix nanocomposite thin films as a phosphate ion sensor. Moreover, the value of absolute transmittance signal ( $\Delta T$ ) at a particular phosphate concentration was found higher for the nanocomposite when compared to the  $\text{Co}_3\text{O}_4$  standard film. The sensitivity ( $\sim 0.03$  Abs/dec) of  $\text{Co}_3\text{O}_4$ –dielectric matrix nanocomposite film presented in this work is less when compared to that of ( $\sim 2.5$  Abs/dec)  $\text{Co}_3\text{O}_4$  thin film sensor of Shimizu [24]. However, the results point to the potential of an improved sensor. A new phosphate sensor (nanocomposite thin film of  $\text{Co}_3\text{O}_4$  nanoparticles embedded in a dielectric matrix) is suggested based on the research in this work. The sensor is sensitive enough to detect environmental standard phosphate ion concentration ( $10^{-6}$  M).

The performance and functional applications of metal oxide–polymer nanocomposites were also reported by other groups [7, 27, 120]. Previous literature proposed that the change in the microstructure was the reason for the enhanced sensitivity. The microstructure can be controlled by embedding the nanoparticles in a matrix, by using carbon nano tubes, and by increasing the surface area. Some groups [27, 120] showed that the performance of the nanocomposite is better than that of the standard. The  $\text{Co}_3\text{O}_4$ –dielectric matrix nanocomposites developed can be used as a new type of functional nanocomposite for optoelectrochemical phosphate sensing. The size of the  $\text{Co}_3\text{O}_4$  nanoparticles, the nature of the matrix can be further adjusted and more improvements can be made to test these nanocomposites for other functional applications.

## 7 Outlook

Research in the field of novel metal/metal oxide – polymer nanocomposites is an expanding field of nanotechnology. Moreover, the use of plasma techniques to develop novel, functional nanocomposites is extensive due to the various advantages of the plasma process. The simple, cheap, and one-step process described in this dissertation can be used to develop new types of metal – polymer nanocomposites. The idea is applicable to other metallic targets such as copper, gold, silver. Additionally, various other monomers such as HMDSO, thiophene, polyaniline can be used. The applicability of different silver – polymer nanocomposites [29, 34, 135–138], copper – polymer nanocomposites [139–142], gold – polymer nanocomposites [143–146] has already been shown. Therefore, the hybrid PVD/PECVD procedure demonstrated in this thesis can be used to prepare other kinds of nanocomposites. Indeed, other types of cobalt/cobalt oxide – polymer nanocomposites can also be prepared which could be used for potential catalytic applications. Improved catalytic performance is observed when the surface area of the active species increases [147–150]. It is shown in this work that by embedding nanoparticles in a matrix, aggregation is prevented and surface area increases. Therefore, new types of nanocomposites with increased surface area can be prepared using the generalized method presented in this dissertation.

The conductive AFM images reflect the presence of surface conductivity. Many gas sensor applications require good surface conductivity [151] as the basic criterion. The variation of the surface conductivity of the nanocomposite is dependent on the composition and concentration of the gaseous environment. The Co – pp HMDSN nanocomposite with 34% metal filling factor prepared in this work demonstrated surface conductivity. Furthermore, detailed I-V characteristics at the nanometer scale can be studied using CAFM. Co – pp HMDSN nanocomposite with 34% metal filling factor indicates conductivity beyond percolation threshold. Also, the TEM micrograph displays a homogeneous distribution. Thus, it is indeed worthwhile to consider the applicability of Co – pp HMDSN nanocomposites as gas sensors [10, 13, 91]. As surface conductivity was observed in the nanocomposites, they may also possess a large potential for electrical

applications [29]. The use of cobalt–SiO<sub>2</sub> nanocomposites is particularly feasible in the field of heterogeneous catalysis [3] and hydrogenation/dehydrogenation catalytic reactions [152]. Co–ppHMDSN nanocomposites prepared in this work are suitable to be analysed to estimate their efficiency in heterogeneous catalytic reactions.

The possible application of Co<sub>3</sub>O<sub>4</sub>–dielectric matrix nanocomposites as phosphate ion sensors has been demonstrated in this work. Further investigations in this direction can be undertaken by varying the type of matrix. Some reports propose an increased gas sensitivity by the incorporation of gold particles in Co<sub>3</sub>O<sub>4</sub> thin films [153, 154]. Indeed, such a model can also be implemented in the Co<sub>3</sub>O<sub>4</sub>–dielectric matrix nanocomposites developed in this work. The variation of the sensor properties with different polymers and precursors would be an interesting attempt in extending the research of this thesis. Thus, the results presented here contribute to further exploit the potential of nanocomposites to improve various technological applications in terms of sensitivity and efficiency.



# List of Figures

2.1	<i>Schematic illustrating the energetic particle bombardment effects on surfaces and growing films [48]. . . . .</i>	15
2.2	<i>Simplified schematic description of DC and RF sputtering systems [48]. .</i>	16
2.3	<i>Simplified schematic description of a magnetron sputtering system [49]. .</i>	17
2.4	<i>Schematic of parallel plate electrode (RF diode) system used for simultaneous plasma polymerization and metal sputtering [61]. M - monomer, Ar - argon, S - substrate, SH - shutter, RF - to RF power supply, P - to pumps, C - to cooling, T - metal target. . . . .</i>	20
2.5	<i>Normalized X-ray absorption spectrum of cobalt metal as a function of X-ray energy. . . . .</i>	22
2.6	<i>Normalized X-ray absorption spectrum of <math>Co_3O_4</math> powder sample as a function of X-ray energy. The different regions in the X-ray absorption spectrum are depicted. . . . .</i>	23
2.7	<i>Schematic of a synchrotron radiation source . . . . .</i>	26
2.8	<i>Schematic illustration of the photoelectric effect. . . . .</i>	28
2.9	<i>Schematic illustration of the X-ray fluorescence effect [66]. . . . .</i>	28
2.10	<i>Schematic illustration of Auger effect [66]. . . . .</i>	29
2.11	<i>Schematic illustration of transmission and fluorescence modes of XAS [63].</i>	30
3.1	<i>Schematic of sputtering reactor used to prepare cobalt – plasma polymerized HMDSN nanocomposites. . . . .</i>	35
3.2	<i>Schematic of sputtering reactor used to prepare cobalt – plasma polymerized HMDSN nanocomposites. Various valves are also depicted. . . . .</i>	35
3.3	<i>Photograph of sputtering reactor used to prepare cobalt – plasma polymerized HMDSN nanocomposites. . . . .</i>	36
3.4	<i>Photograph of the active thermal probe used to measure the energy influx in the sputtering chamber [73]. . . . .</i>	38

---

3.5	<i>Variation of probe temperature and heating power depicting the working of the active thermal probe [73]. . . . .</i>	39
3.6	<i>a) Front and b) Back view positioning of active thermal probe in the reaction chamber. . . . .</i>	39
3.7	<i>Schematic of experimental set up for optoelectrochemical measurements. WE: Working electrode (<math>Co_3O_4</math> – dielectric matrix nanocomposite thin film). . . . .</i>	41
3.8	<i>Photograph of experimental setup for optoelectrochemical measurements. . . . .</i>	41
3.9	<i>Photograph depicting the placement of the working electrode (<math>Co_3O_4</math> – dielectric matrix nanocomposite thin film) in the three electrode cell. . . . .</i>	42
3.10	<i>Bragg’s law depicting the condition for constructive interference in X-ray diffraction. . . . .</i>	43
3.11	<i>Schematic diagram of grazing incidence X-ray diffractometry (GIXD) [75]. . . . .</i>	44
3.12	<i>Photograph showing the XPS machine used to analyse the Co – pp HDMSN nanocomposites. . . . .</i>	47
3.13	<i>Fundamental vibrational modes for a nonlinear <math>CH_2</math> group (+ indicates motion out of the plane of paper, - indicates motion into the plane of paper) [79]. . . . .</i>	49
3.14	<i>Principle of operation of attenuated total reflection technique [80]. . . . .</i>	49
3.15	<i>Schematic illustration of various signals produced when an electron beam interacts with a specimen [81]. . . . .</i>	51
3.16	<i>Schematic illustration of the construction of an SEM machine [82]. . . . .</i>	52
3.17	<i>Schematic illustration of layout and optics in TEM [83]. . . . .</i>	54
3.18	<i>Schematic illustration depicting operation of AFM [84]. . . . .</i>	56
3.19	<i>Different modes of AFM operation. . . . .</i>	56
3.20	<i>Schematic of experimental set-up for conductive atomic force microscopy (CAFM) to map surface conductivity of cobalt – plasma polymerized HMDSN nanocomposite thin films. . . . .</i>	58
3.21	<i>Schematic representation of a typical three electrode electrochemical cell. AE: Auxiliary electrode, WE: Working electrode, RE: Reference electrode [86]. . . . .</i>	58
3.22	<i>Top view of BESSY synchrotron radiation source in Berlin. . . . .</i>	60
4.1	<i>TEM micrographs of cobalt – plasma polymerized HMDSN nanocomposites with varying metal filling factors: a) 17%, b) 25%, c) 34%. . . . .</i>	63

---

---

4.2	<i>Histogram of size distribution of nanoparticles of cobalt-plasma polymerized HMDSN nanocomposite at 34% metal filling factor with a Gaussian fitting (line).</i>	64
4.3	<i>Grazing incidence XRD patterns (<math>\omega = 0.5^\circ</math>) of cobalt-plasma polymerized HMDSN nanocomposites at metal filling factors of a) 25%, b) 34%.</i>	64
4.4	<i>XPS survey spectra of cobalt-plasma polymerized HMDSN nanocomposites at various metal filling factors.</i>	65
4.5	<i>A typical highly resolved measured C 1s spectrum of cobalt-plasma polymerized HMDSN nanocomposites at two different metal filling factors: a) 4%, b) 34%.</i>	67
4.6	<i>Summary of percentage of bindings of: a) C 1s and b) O 1s highly resolved peaks of cobalt-plasma polymerized HMDSN nanocomposites at various metal filling factors.</i>	68
4.7	<i>Co <math>2p_{3/2}</math> hi res peaks of Co-pp HMDSN nanocomposite with 34% metal filling factor.</i>	69
4.8	<i>Column chart representation of bulk relative atomic concentrations of various elements of cobalt-plasma polymerized HMDSN nanocomposites at various metal filling factors analyzed by EDX</i>	69
4.9	<i>ATR-FTIR spectra of cobalt-plasma polymerized HMDSN nanocomposites at various metal filling factors and pure plasma polymerized (pp) HMDSN film. The spectra are offset by the same value for better clarity. The labels correspond to Table 4.3</i>	71
4.10	<i>3D a) topography and b) surface conductivity images of cobalt-plasma polymerized HMDSN nanocomposite at 34% metal filling factor. DC bias voltage applied = 4 V.</i>	74
4.11	<i>Steps involved in the analysis of X-ray absorption spectrum - example using a cobalt metal foil standard. The detailed description of the steps is explained previously in Section 2.3.1.5.</i>	76
4.12	<i>Normalized absorption spectra of cobalt standards.</i>	78
4.13	<i>Normalized XANES spectra of cobalt standards.</i>	78
4.14	<i>EXAFS function <math>\chi(k)</math> of the cobalt standards.</i>	79
4.15	<i>Radial distribution function (RDF) of cobalt standards.</i>	80
4.16	<i>Normalized absorption spectra of cobalt standards and Co-pp HMDSN nanocomposites at various metal filling factors (34%, 25% and 17%).</i>	81

---

---

4.17	<i>Normalized XANES spectra of cobalt standards and Co–pp HMDSN nanocomposites at various metal filling factors (34%, 25% and 17%). . . . .</i>	82
4.18	<i>EXAFS function <math>\chi(k)</math> of Co–pp HMDSN nanocomposites at various metal filling factors (34%, 25% and 17%). . . . .</i>	84
4.19	<i>RDF of cobalt standards and Co–pp HMDSN nanocomposites at various metal filling factors (34%, 25% and 17%). . . . .</i>	85
4.20	<i>Normalized absorption spectra of cobalt standards and Co–pp HMDSN nanocomposites a–d. . . . .</i>	86
4.21	<i>Normalized XANES spectra of cobalt standards and Co–pp HMDSN nanocomposites a–d. . . . .</i>	87
4.22	<i>EXAFS function <math>\chi(k)</math> of Co–pp HMDSN nanocomposites a–d. . . . .</i>	88
4.23	<i>RDF of cobalt standards and Co–pp HMDSN nanocomposites a–d. . . . .</i>	89
4.24	<i>Normalized absorption spectra of cobalt standards and Co–pp HMDSN nanocomposites e–g. . . . .</i>	91
4.25	<i>Normalized XANES spectra of cobalt standards and Co–pp HMDSN nanocomposites e–g. . . . .</i>	91
4.26	<i>EXAFS function <math>\chi(k)</math> of Co–pp HMDSN nanocomposites e–g. . . . .</i>	93
4.27	<i>RDF of cobalt standards and Co–pp HMDSN nanocomposites e–g. . . . .</i>	94
4.28	<i>Heating power and Power density in argon plasma measured by active thermal probe at a magnetron power of 100 W. . . . .</i>	95
4.29	<i>Energy influx and power density as a function of magnetron power in argon plasma measured by active thermal probe. . . . .</i>	97
4.30	<i>Heating power and power density in argon + HMDSN plasma measured by active thermal probe at a magnetron power of 100 W. . . . .</i>	97
4.31	<i>Heating power in argon + HMDSN plasma plasma measured by active thermal probe at a magnetron power of 100 W. Several sharp peaks are seen when the plasma is switched on and off. . . . .</i>	99
4.32	<i>Heating power in argon + HMDSN plasma plasma measured by active thermal probe at a magnetron power of 100 W. The influence of the variation of HMDSN and Ar is studied. . . . .</i>	99
5.1	<i>Grazing incidence XRD patterns (<math>\omega = 0.5^\circ</math>) of a) <math>\text{Co}_3\text{O}_4</math> standard, b) Calcinated Co–pp HMDSN nanocomposite thin films. Peak corresponding to the FTO substrate are denoted as S. . . . .</i>	105

---

---

5.2	<i>Optical absorption spectra of <math>Co_3O_4</math> standard and <math>Co_3O_4</math> –dielectric matrix nanocomposite thin films in air.</i> . . . . .	106
5.3	<i>ATR-FTIR spectrum of <math>Co_3O_4</math> –dielectric matrix nanocomposite.</i> . . . . .	107
5.4	<i>Zoomed in ATR-FTIR spectrum of <math>Co_3O_4</math> –dielectric matrix nanocomposite.</i>	107
5.5	<i>EDX estimation of elemental atomic percentage of <math>Co_3O_4</math> –dielectric matrix nanocomposite.</i> . . . . .	108
5.6	<i>SEM micrographs of <math>Co_3O_4</math> –dielectric matrix nanocomposite thin films. Scale is shown in the figure.</i> . . . . .	109
5.7	<i>Optical transmittance values of <math>Co_3O_4</math> –dielectric matrix nanocomposite thin film at different applied potentials in <math>10^{-3}</math> M <math>Na_2HPO_4</math> solution. The transmittance values are reversible and reproducible upon the application and removal of potential. ‘Forwards’ indicates increase and ‘Backwards’ indicates decrease in applied potential respectively.</i> . . . . .	111
5.8	<i>Transmittance spectra of <math>Co_3O_4</math> –dielectric matrix nanocomposite thin film at three different <math>Na_2HPO_4</math> concentrations at an applied potential of 0.8 V vs Ag/AgCl.</i> . . . . .	112
5.9	<i>Plot of <math>\Delta T</math> vs <math>Na_2HPO_4</math> concentration of <math>Co_3O_4</math> –dielectric matrix nanocomposite and <math>Co_3O_4</math> standard thin films together with the fits. <math>\Delta T = T_{0V} - T_{0.8V}</math></i> . . . . .	114



# List of Tables

4.1	<i>Elemental content of Co–pp HMDSN nanocomposites at various metal filling factors measured by XPS . . . . .</i>	66
4.2	<i>Binding energies used to fit the C 1s, Si 2p, and Co 2p<sub>3/2</sub> high res peaks . . . . .</i>	67
4.3	<i>Characteristic infrared absorption bonds of organosilicon compounds. The label numbers correspond to the peak numbers in Figure 4.9. . . . .</i>	70
4.4	<i>Edge energies and XANES peaks of cobalt standards . . . . .</i>	79
4.5	<i>Fourier transform (FT) peaks of cobalt standards . . . . .</i>	80
4.6	<i>Edge energies and XANES peaks of Co–pp HMDSN nanocomposites at various metal filling factors. . . . .</i>	82
4.7	<i>FT peaks of Co–pp HMDSN nanocomposites at various metal filling factors. . . . .</i>	84
4.8	<i>Co–pp HMDSN nanocomposites prepared at various plasma parameters. . . . .</i>	86
4.9	<i>Edge energies and XANES peaks of Co–pp HMDSN nanocomposites a–d. . . . .</i>	87
4.10	<i>FT peaks of Co–pp HMDSN nanocomposites a–d . . . . .</i>	89
4.11	<i>Edge energies and XANES peaks of Co–pp HMDSN nanocomposites e–g. . . . .</i>	90
4.12	<i>FT peaks of Co–pp HMDSN nanocomposites e–g. . . . .</i>	93





# Bibliography

- [1] F. Faupel, V. Zaporozhchenko, H. Greve, U. Schuermann, V. S. K. Chakravadhana, C. Hanisch, A. Kulkarni, A. Gerber, E. Quandt, and R. Podschun. Deposition of nanocomposites by plasmas. *Contributions to Plasma Physics*, 47(7):pp. 537–544, (2007). ISSN 08631042. doi:10.1002/ctpp.200710069.
- [2] C. Walter, V. Brueser, and K. D. Weltmann. Novel method to produce cobalt-polypyrrole catalysts for oxygen reduction reaction by dual plasma process. *Surface and Coatings Technology*, 205:pp. S258–S260, (2011). ISSN 02578972. doi:10.1016/j.surfcoat.2011.02.015.
- [3] Qiaohong Zhang, Chen Chen, Min Wang, Jiaying Cai, Jie Xu, and Chungu Xia. Facile preparation of highly-dispersed cobalt-silicon mixed oxide nanosphere and its catalytic application in cyclohexane selective oxidation. *Nanoscale research letters*, 6, (2011). ISSN 1931-7573. doi:10.1186/1556-276X-6-586.
- [4] Oleg Yeshchenko, Igor Dmitruk, Alexandr Alexeenko, Andriy Dmytruk, and Vitaliy Tinkov. Optical properties of sol-gel fabricated Co/SiO<sub>2</sub> nanocomposites. *Physica E: Low-dimensional Systems and Nanostructures*, 41(1):pp. 60 – 65, (2008). ISSN 1386-9477. doi:10.1016/j.physe.2008.06.003.
- [5] L.G. Jacobsohn, J.D. Thompson, R.M. Dickerson, and M. Nastasi. Magnetic properties of cobalt nanoparticles obtained by ion implantation into amorphous silica. *Nuclear Instruments and Methods in Physics Research Section B: Beam Interactions with Materials and Atoms*, 257(1-2):pp. 447 – 450, (2007). ISSN 0168-583X. doi:10.1016/j.nimb.2007.01.026.
- [6] Diandra L. Leslie-Pelecky, X. Q. Zhang, and Reuben D. Rieke. Self-stabilized magnetic colloids: Ultrafine cobalt particles in polymers. *Journal of Applied Physics*, 79(8):pp. 5312–5314, (1996). ISSN 00218979. doi:10.1063/1.361362.

- [7] C Cantalini, M Post, D Buso, M Guglielmi, and A Martucci. Gas sensing properties of nanocrystalline NiO and Co<sub>3</sub>O<sub>4</sub> in porous silica sol-gel films. *Sensors and Actuators B: Chemical*, 108(1-2):pp. 184–192, (2005). ISSN 0925-4005. doi:10.1016/j.snb.2004.11.073.
- [8] Serena Esposito, Antonio Setaro, Pasqualino Maddalena, Antonio Aronne, Pasquale Pernice, and Marco Laracca. Synthesis of cobalt doped silica thin film for low temperature optical gas sensor. *Journal of Sol-Gel Science and Technology*, 60:pp. 388–394, (2011). ISSN 0928-0707. doi:10.1007/s10971-011-2483-y.
- [9] Lidia Armelao, Davide Barreca, Silvia Gross, Alessandro Martucci, Manuela Tieto, and Eugenio Tondello. Cobalt oxide-based films: sol-gel synthesis and characterization. *Journal of Non-Crystalline Solids*, 293-295(0):pp. 477 – 482, (2001). ISSN 0022-3093. doi:10.1016/S0022-3093(01)00753-0.
- [10] A. Martucci, D. Buso, M. Guglielmi, L. Zbroniec, N. Koshizaki, and M. Post. Optical gas sensing properties of silica film doped with cobalt oxide nanocrystals. *Journal of Sol-Gel Science and Technology*, 32:pp. 243–246, (2004). ISSN 0928-0707. doi:10.1007/s10971-004-5795-3.
- [11] Marc Verelst, Teyeb Ould Ely, Catherine Amiens, Etienne Snoeck, Pierre Lecante, Alain Mosset, Marc Respaud, Jean Marc Broto, and Bruno Chaudret. Synthesis and characterization of CoO, Co<sub>3</sub>O<sub>4</sub>, and mixed Co/CoO nanoparticles. *Chemistry of Materials*, 11(10):pp. 2702–2708, (1999). doi:10.1021/cm991003h.
- [12] Alessandro Martucci, Mirko Pasquale, Massimo Guglielmi, Mike Post, and Jean Claude Pivin. Nanostructured silicon oxide-nickel oxide sol-gel films with enhanced optical carbon monoxide gas sensitivity. *Journal of the American Ceramic Society*, 86(9):pp. 1638–1640, (2003). ISSN 1551-2916. doi:10.1111/j.1151-2916.2003.tb03533.x.
- [13] Serena Esposito, Maria Turco, Gianguido Ramis, Giovanni Bagnasco, Pasquale Pernice, Concetta Pagliuca, Maria Bevilacqua, and Antonio Aronne. Cobalt-silicon mixed oxide nanocomposites by modified sol-gel method. *Journal of Solid State Chemistry*, 180(12):pp. 3341 – 3350, (2007). ISSN 0022-4596. doi:10.1016/j.jssc.2007.09.032.
- [14] C. de Julian Fernandez, G. Mattei, C. Sada, C. Battaglin, and P. Mazzoldi. Nanostructural and optical properties of cobalt and nickel-oxide/silica nanocomposites.

- 
- Materials Science and Engineering: C*, 26(5-7):pp. 987 – 991, (2006). ISSN 0928-4931. doi:10.1016/j.msec.2005.09.013.
- [15] S O Engblom. The phosphate sensor. *Biosensors and Bioelectronics*, 13(9):pp. 981–994, (1998). ISSN 0956-5663. doi:10.1016/S0956-5663(98)00001-3.
- [16] Brian Moss. *Ecology of fresh waters*. Blackwell Scientific, (1980).
- [17] N. Conrath, B. Gruendig, St. Huewel, and K. Cammann. A novel enzyme sensor for the determination of inorganic phosphate. *Analytica Chimica Acta*, 309(1-3):pp. 47 – 52, (1995). ISSN 0003-2670. doi:10.1016/0003-2670(95)00065-8.
- [18] Etsuo Watanabe, Hideaki Endo, and Kenzo Toyama. Determination of phosphate ions with an enzyme sensor system. *Biosensors*, 3(5):pp. 297 – 306, (1987-1988). ISSN 0265-928X. doi:10.1016/0265-928X(87)80002-0.
- [19] L Campanella, M Cordatore, F Mazzei, and M Tomassetti. Determination of inorganic phosphate in drug formulations and biological fluids using a plant tissue electrode. *Journal of Pharmaceutical and Biomedical Analysis*, 8(8-12):pp. 711–716, (1990). ISSN 0731-7085. doi:10.1016/0731-7085(90)80108-2.
- [20] Jin-Hwan Lee, Woo Hyoung Lee, Paul L Bishop, and Ian Papautsky. A cobalt-coated needle-type microelectrode array sensor for in situ monitoring of phosphate. *Journal of Micromechanics and Microengineering*, 19(2):pp. 025022, (2009). doi:10.1088/0960-1317/19/2/025022.
- [21] RK Meruva and ME Meyerhoff. Mixed potential response mechanism of cobalt electrodes toward inorganic phosphate. *ANALYTICAL CHEMISTRY*, 68(13):pp. 2022–2026, (1996). doi:10.1021/ac951086v.
- [22] Gwon-Shik Ihn, Charles F. Nash, and Richard P. Buck. Monohydrogenphosphate-sensing electrode formulations. *Analytica Chimica Acta*, 121(0):pp. 101 – 109, (1980). ISSN 0003-2670. doi:10.1016/S0003-2670(01)84404-4.
- [23] D MIDGLEY. Sulfate and phosphate ion-selective electrodes. *ION-SELECTIVE ELECTRODE REVIEWS*, 8(1):pp. 3–54, (1986). ISSN 0191-5371.
- [24] Youichi Shimizu and Yusuke Furuta. An opto-electrochemical phosphate-ion sensor using a cobalt-oxide thin-film electrode. *Solid State Ionics*, 113-115(0):pp. 241 – 245, (1998). ISSN 0167-2738. doi:10.1016/S0167-2738(98)00288-4.
-

- [25] M. Stefanescu, T. Dippong, M. Stoia, and O. Stefanescu. Study on the obtaining of cobalt oxides by thermal decomposition of some complex combinations, undispersed and dispersed in SiO<sub>2</sub> matrix. *Journal of Thermal Analysis and Calorimetry*, 94:pp. 389–393, (2008). ISSN 1388-6150. doi:10.1007/s10973-008-9111-2.
- [26] M Roy, J K Nelson, R K MacCrone, L S Schadler, C W Reed, R Keefe, and W Zenger. Polymer nanocomposite dielectrics - the role of the interface. *IEEE Transactions on Dielectrics and Electrical Insulation*, 12(6):pp. 1273–1273, (2005). ISSN 1070-9878. doi:10.1109/TDEI.2005.1511089.
- [27] Wang X., Sakai G., Shimanoe K., Miura N., and Yamazoe N. Spin-coated thin films of SiO<sub>2</sub>-WO<sub>3</sub> composites for detection of sub-ppm NO<sub>2</sub>. *Sensors and Actuators B: Chemical*, 45(2):pp. 141–146, (1997). ISSN 0925-4005. doi:10.1016/S0925-4005(97)00286-4.
- [28] A. Daniel, C. Le Pen, C. Archambeau, and F. Reniers. Use of a PECVD-PVD process for the deposition of copper containing organosilicon thin films on steel. *Applied Surface Science*, 256(3):pp. S82–S85, (2009). ISSN 0169-4332. doi:10.1016/j.apsusc.2009.04.195.
- [29] H Takele, A Kulkarni, S Jebril, V S K Chakravadhanula, C Hanisch, T Strunskus, V Zaporozhtchenko, and F Faupel. Plasmonic properties of vapour-deposited polymer composites containing Ag nanoparticles and their changes upon annealing. *Journal of Physics D: Applied Physics*, 41(12):pp. 125409, (2008). ISSN 00223727. doi:10.1088/0022-3727/41/12/125409.
- [30] Arava Leela Mohana Reddy, Natarajan Rajalakshmi, and Sundara Ramaprabhu. Cobalt-polypyrrole-multiwalled carbon nanotube catalysts for hydrogen and alcohol fuel cells. *Carbon*, 46(1):pp. 2 – 11, (2008). ISSN 0008-6223. doi:10.1016/j.carbon.2007.10.021.
- [31] D K Avasthi, Y K Mishra, D Kabiraj, N P Lalla, and J C Pivin. Synthesis of metal-polymer nanocomposite for optical applications. *Nanotechnology*, 18(12):pp. 125604, (2007). doi:10.1088/0957-4484/18/12/125604.
- [32] Jiongxin Lu, Kyoung-Sik Moon, Jianwen Xu, and C. P. Wong. Synthesis and dielectric properties of novel high-K polymer composites containing in-situ formed silver nanoparticles for embedded capacitor applications. *J. Mater. Chem.*, 16:pp. 1543–1548, (2006). ISSN 09599428. doi:10.1039/B514182F.

- [33] E. P. Rajiv, A. Iyer, and S. K. Seshadri. Corrosion Characteristics of Cobalt-Silicon Nitride Electro Composites in Various Corrosive Environments. *Materials Chemistry and Physics*, 40(3):pp. 189–196, (1995). ISSN 0254-0584. doi:10.1016/0254-0584(95)01479-9.
- [34] A. Biswas, O. C. Aktas, U. Schuermann, U. Saeed, V. Zaporojtchenko, F. Faupel, and T. Strunskus. Tunable multiple plasmon resonance wavelengths response from multicomponent polymer-metal nanocomposite systems. *Applied Physics Letters*, 84(14):pp. 2655–2657, (2004). ISSN 0003-6951. doi:10.1063/1.1697626.
- [35] H. Greve, C. Pochstein, H. Takele, V. Zaporojtchenko, F. Faupel, A. Gerber, M. Frommberger, and E. Quandt. Nanostructured magnetic Fe-Ni-Co/Teflon multilayers for high-frequency applications in the gigahertz range. *Applied Physics Letters*, 89(24):pp. 242501, (2006). ISSN 1077-3118. doi:10.1063/1.2402877.
- [36] E. Barrera, A. Avila, J. Mena, V. H. Lara, M. Ruiz, and J. Mendez-Vivar. Synthesis of cobalt-silicon oxide thin films. *Solar Energy Materials and Solar Cells*, 76(3): pp. 387–398, (2003). ISSN 0927-0248. doi:10.1016/S0927-0248(02)00290-8.
- [37] E. Cattaruzza, G. Battaglin, P. Canton, C. de Julian Fernandez, M. Ferroni, T. Finotto, C. Maurizio, and C. Sada. Structural and physical properties of cobalt nanocluster composite glasses. *Journal of Non-Crystalline Solids*, 336(2):pp. 148 – 152, (2004). ISSN 0022-3093. doi:10.1016/j.jnoncrysol.2004.01.003.
- [38] E. M. Logothetis, W. J. Kaiser, H. K. Plummer, and S. S. Shinozaki. Tandem deposition of small metal-particle composites. *Journal of Applied Physics*, 60(7): pp. 2548–2552, (1986). ISSN 0021-8979. doi:10.1063/1.337119.
- [39] O Cintora-Gonzalez, D Muller, C Estournes, M Richard-Plouet, R Poinsot, J.J Grob, and J Guille. Structure and magnetic properties of Co<sup>+</sup>-implanted silica. *Nuclear Instruments and Methods in Physics Research Section B: Beam Interactions with Materials and Atoms*, 178(1-4):pp. 144 – 147, (2001). ISSN 0168-583X. doi:10.1016/S0168-583X(01)00494-3.
- [40] C. Laurent and E. Kay. Electrical and magnetic properties of thin films containing metal clusters. *Zeitschrift für Physik D Atoms, Molecules and Clusters*, 12:pp. 465–467, (1989). ISSN 0178-7683. doi:10.1007/BF01426998.

- [41] S I Shah and K M Unruh. X-ray photoelectron spectroscopy of (Fe,Co,Ni)-SiO<sub>2</sub> granular films. *Applied Physics Letters*, 59:pp. 3485–3487, (1991). ISSN 00036951. doi:10.1063/1.105661.
- [42] S.I. Shah, B.A. Doele, I. Weerasekera, and K.M. Unruh. Fabrication and in situ x-ray photoelectron spectroscopy of granular metal thin films. *Thin Solid Films*, 206 (1-2):pp. 264 – 268, (1991). ISSN 0040-6090. doi:10.1016/0040-6090(91)90433-X.
- [43] Naoto Koshizaki, Katsuya Yasumoto, and Takeshi Sasaki. Mechanism of optical transmittance change by NO<sub>x</sub> in CoO/SiO<sub>2</sub> nanocomposites films. *Sensors and Actuators B: Chemical*, 66(1-3):pp. 122 – 124, (2000). ISSN 0925-4005. doi:10.1016/S0925-4005(00)00312-9.
- [44] A. Basumallick, K. Biswas, S. Mukherjee, and G.C. Das. Preparation of Co and Fe nanocomposites in SiO<sub>2</sub> matrices. *Materials Letters*, 30(5-6):pp. 363 – 368, (1997). ISSN 0167-577X. doi:10.1016/S0167-577X(96)00223-6.
- [45] S. R. Mishra, I. Dubenko, J. Losby, K. Marasinghe, M. Ali, and N. Ali. Magnetic properties of magnetically soft nanocomposite Co-SiO<sub>2</sub> prepared via mechanical milling. *Journal of Nanoscience and Nanotechnology*, 5(12):pp. 2082–2087, (2005). doi:10.1166/jnn.2005.188.
- [46] Young-Man Jeong, Jae-Keun Lee, Sam-Chul Ha, and Soo H. Kim. Fabrication of cobalt-organic composite thin film via plasma-enhanced chemical vapor deposition for antibacterial applications. *Thin Solid Films*, 517(9):pp. 2855 – 2858, (2009). ISSN 0040-6090. doi:10.1016/j.tsf.2008.10.063.
- [47] S.M. Rossnagel, J.J. Cuomo, and W.D Westwood. *Handbook of Plasma Processing Technology - Fundamentals, Etching, Deposition, and Surface Interactions*. Noyes, (1990).
- [48] Milton Ohring. Chapter 4 - Discharges, plasmas, and ion-surface interactions. In *Materials Science of Thin Films (Second Edition)*, pages 145 – 202. Academic Press, San Diego, Second edition, (2002). ISBN 978-0-12-524975-1. doi:10.1016/B978-012524975-1/50007-0.
- [49] Franz Gerhard. *Low Pressure Plasmas and Microstructuring Technology*. Springer, (2009).

- 
- [50] D.M Mattox. *Handbook of Physical Vapor Deposition (PVD) Processing*. Elsevier professional, (2007).
- [51] T.Belmonte, A. Daniel, and T. Duguet. PVD-PECVD Hybrid Processes: Synthesis of Composite Thin Films and Process Understanding. *Key Engineering Materials*, 373-374:pp. 93–99, (2008). ISSN 1013-9826. doi:10.4028/www.scientific.net/KEM.373-374.93.
- [52] J.P Celis, D Drees, M.Z Huq, P.Q Wu, and M De Bonte. Hybrid processes - a versatile technique to match process requirements and coating needs. *Surface and Coatings Technology*, 113(1-2):pp. 165 – 181, (1999). ISSN 0257-8972. doi:10.1016/S0257-8972(98)00836-6.
- [53] U Kreibig and M Vollmer. *Optical properties of metal clusters*. Springer, (1995).
- [54] Schmid G. *Clusters and colloids : from theory to applications*. VCH, (1994).
- [55] F. Caruso. Nanoengineering of particle surfaces. *Advanced Materials*, 13(1):pp. 11–22, (2001). ISSN 1521-4095. doi:10.1002/1521-4095(200101)13:1<11::AID-ADMA11>3.0.CO;2-N.
- [56] G. Schmid. Nanoclusters - building blocks for future nanoelectronic devices? *Advanced Engineering Materials*, 3(10):pp. 737–743, (2001). ISSN 1527-2648. doi:10.1002/1527-2648(200110)3:10<737::AID-ADEM737>3.0.CO;2-8.
- [57] Halit S. Göktürk, Thomas J. Fiske, and Dilhan M. Kalyon. Granular magnetic composites employing cobalt based amorphous alloys in a polymeric host. *Journal of Applied Physics*, 73(10):pp. 5598–5600, (1993). ISSN 0021-8979. doi:10.1063/1.353663.
- [58] Heilmann A. *Polymer films with embedded metal particles*. Springer, (2003).
- [59] Eric Kay, John Coburn, and Alan Dilks. Plasma chemistry of fluorocarbons as related to plasma etching and plasma polymerization. In Stanislav Veprek and Mundiayath Venugopalan, editors, *Plasma Chemistry III*, volume 94 of *Topics in Current Chemistry*, pages pp. 1–42. Springer Berlin / Heidelberg, (1980). ISBN 978-3-540-10166-6.
-

- [60] A. Daniel, T. Duguet, and T. Belmonte. Description of a hybrid PECVD-PVD process: Application to Zn-Si-O and Ti-Si-O composites thin films. *Applied Surface Science*, 253(24):pp. 9323 – 9329, (2007). ISSN 0169-4332. doi:10.1016/j.apsusc.2007.05.063.
- [61] H Biederman and Y Osada. Plasma chemistry of polymers. *Advances in Polymer Science*, 95:pp. 57–109, (1990). doi:10.1007/3-540-52159-3\_6.
- [62] Farideh Jalilvand. *Structure of hydrated ions and cyanide complexes by X-ray absorption spectroscopy*. PhD thesis, Royal Institute of Technology, Department of Chemistry, Stockholm, (2000).
- [63] Grant Bunker. *Introduction to XAFS: A Practical Guide to X-ray Absorption Fine Structure Spectroscopy*. Cambridge University Press, first edition, (2010).
- [64] D. C. Koningsberger, B. L. Mojet, G. E. van Dorssen, and D. E. Ramaker. Xafs spectroscopy; fundamental principles and data analysis. *Topics in Catalysis*, 10 (3-4):pp. 143–155, (2000). ISSN 10225528. doi:10.1023/A:1019105310221.
- [65] D.E. Sayers, E.A. Stern, and F.W. Lytle. New Technique for Investigating Noncrystalline Structures: Fourier Analysis of the Extended X-Ray Absorption Fine Structure. *Physical Review Letters*, 27:pp. 1204–1207, (1971). doi:10.1103/PhysRevLett.27.1204.
- [66] D.C Koningsberger. *X-ray absorption : principles, applications, techniques of EXAFS, SEXAFS and XANES*. Wiley, (1988).
- [67] Matthias Wolter, Marc Stahl, and Holger Kersten. Spatially resolved thermal probe measurement for the investigation of the energy influx in an rf-plasma. *Vacuum*, 83(4):pp. 768 – 772, (2008). ISSN 0042-207X. doi:10.1016/j.vacuum.2008.05.017.
- [68] John A. Thornton. Influence of apparatus geometry and deposition conditions on the structure and topography of thick sputtered coatings. *Journal of Vacuum Science and Technology*, 11(4):pp. 666–670, (1974). doi:10.1116/1.1312732.
- [69] I Hussla, K Enke, H Grunwald, G Lorenz, and H Stoll. In situ silicon-wafer temperature measurements during rf argon-ion plasma etching via fluoroptic thermometry. *Journal of Physics D: Applied Physics*, 20(7):pp. 889, (1987). doi:10.1088/0022-3727/20/7/010.



- 
- [70] H. Deutsch, H. Kersten, and A. Rutscher. Basic mechanisms in plasma etching. *Contributions to Plasma Physics*, 29(3):pp. 263–284, (1989). ISSN 1521-3986. doi:10.1002/ctpp.2150290304.
- [71] H. Deutsch, H. Kersten, S. Klagge, and A. Rutscher. On the temperature dependence of plasma polymerization. *Contributions to Plasma Physics*, 28(2):pp. 149–155, (1988). ISSN 1521-3986. doi:10.1002/ctpp.2150280206.
- [72] H. Kersten, H. Deutsch, H. Steffen, G.M.W. Kroesen, and R. Hippler. The energy balance at substrate surfaces during plasma processing. *Vacuum*, 63(3):pp. 385 – 431, (2001). ISSN 0042-207X. doi:10.1016/S0042-207X(01)00350-5.
- [73] Ruben Wiese, Holger Kersten, Georg Wiese, and Marko Haeckel. Aktive thermosonde zur messung des energieeinstromes. *Vakuum in Forschung und Praxis*, 23(3):pp. 20–23, (2011). ISSN 1522-2454. doi:10.1002/vipr.201100461.
- [74] Ulrich Schuermann, Whitney Hartung, Haile Takele, Vladimir Zaporozhchenko, and Franz Faupel. Controlled syntheses of Ag-polytetrafluoroethylene nanocomposite thin films by co-sputtering from two magnetron sources. *Nanotechnology*, 16(8):pp. 1078, (2005). doi:10.1088/0957-4484/16/8/014.
- [75] H. Wulff and H. Steffen. *Characterization of Thin Solid Films in "Low Temperature Plasmas"*, pages 329–362. Schoenbach VILEY-VCH), (2008).
- [76] Kai Siegbahn. *ESCA applied to free molecules*. North-Holland Publ. [u.a.], (1969).
- [77] John F. Moulder, William F. Stickle, Peter E. Sobol, and Kenneth D. Bomben. *Handbook of X Ray Photoelectron Spectroscopy*. (1995).
- [78] Peter R. Griffiths and James A. de Haseth. *Fourier Transform Infrared Spectrometry*. John Wiley and Sons, (1986).
- [79] Robert Milton Silverstein and Francis X. Webster. *Spectrometric Identification of Organic Compounds*. Wiley, (1998).
- [80] Milan Milosevic. *Internal reflection and ATR spectroscopy*. Wiley, (2012).
- [81] Robert Edward Lee. *Scanning electron microscopy and x-ray microanalysis*. Prentice Hall, (1993).
-

- [82] Ray F. Egerton. *Physical principles of electron microscopy : an introduction to TEM, SEM, and AEM*. Springer, third edition, (2008).
- [83] Brent Fultz and James M. Howe. *Transmission electron microscopy and diffraction of materials*. Springer, third edition, (2008).
- [84] Veeco Instruments DI CPII. Afm - user guide.
- [85] K. Vasu, M. Ghanashyam Krishna, and K.A. Padmanabhan. Conductive-atomic force microscopy study of local electron transport in nanostructured titanium nitride thin films. *Thin Solid Films*, 519(22):pp. 7702 – 7706, (2011). ISSN 0040-6090. doi:10.1016/j.tsf.2011.05.052.
- [86] Joseph Wang. *Analytical electrochemistry*. Wiley-VCH, (2006).
- [87] L. H. Wang and C. S. Wang. Co speciation in blue decorations of blue-and-white porcelains from Jingdezhen kiln by using XAFS spectroscopy. *Journal of Analytical Atomic Spectrometry*, 26(9):pp. 1796–1801, (2011). doi:10.1039/C0JA00240B.
- [88] www.bessy.de. Accessed December 30, 2011.
- [89] Bruce Ravel. *ATHENA - User guide*, (2007).
- [90] Ravel B and Newville M. ATHENA, ARTEMIS, HEPHAESTUS: data analysis for X-ray absorption spectroscopy using IFEFFIT. *Journal of Synchrotron Radiation*, (2007). ISSN 0909-0495. doi:10.1107/S0909049505012719.
- [91] K. Yasumoto and N. Koshizaki. X-ray photoelectron spectroscopy characterization of CoO/SiO<sub>2</sub> nanocomposites and their optical transmittance change by nitrogen oxide. *Journal of Materials Science Letters*, 16:pp. 215–217, (1997). ISSN 0261-8028. doi:10.1023/A:1018547606355.
- [92] M. Jamet, V. Dupuis, P. Mélinon, G. Guiraud, A. Pérez, W. Wernsdorfer, A. Traverse, and B. Baguenard. Structure and magnetism of well defined cobalt nanoparticles embedded in a niobium matrix. *Phys. Rev. B*, 62:pp. 493–499, (2000). doi:10.1103/PhysRevB.62.493.
- [93] E. Cattaruzza, G. Battaglin, P. Canton, C. de Julian Fernandez, M. Ferroni, F. Gonella, C. Maurizio, P. Riello, C. Sada, C. Sangregorio, and B.F. Scremin. Radiofrequency magnetron co-sputtering deposition synthesis of Co-based nanocom-

- 
- posite glasses for optical and magnetic applications. *Applied Surface Science*, 226 (1-3):pp. 62 – 67, (2004). ISSN 0169-4332. doi:10.1016/j.apsusc.2003.11.032.
- [94] H. Y. Kwong, Y. W. Wong, and K. H. Wong. Temperature dependence of magnetoresistivity of cobalt-polytetrafluoroethylene granular composite films. *Journal of Applied Physics*, 102(11):pp. 114303, (2007). ISSN 1089-7550. doi:10.1063/1.2821240.
- [95] Christian Walter, Volker Brueser, and Klaus-Dieter Weltmann. Novel method to produce cobalt-polypyrrole catalysts for oxygen reduction reaction by dual plasma process. *Surface and Coatings Technology*, 205, Supplement 2(0):pp. S258 – S260, (2011). ISSN 0257-8972. doi:10.1016/j.surfcoat.2011.02.015.
- [96] A. Kulkarni, V. S. K. Chakravadhanula, V. Duppel, D. Meyners, V. Zaporozhchenko, T. Strunskus, L. Kienle, E. Quandt, and F. Faupel. Morphological and magnetic properties of  $\text{TiO}_2/\text{Fe}_{50}\text{Co}_{50}$  composite films. *Journal of Materials Science*, 46(13):pp. 4638–4645, (2011). ISSN 00222461. doi:10.1007/s10853-011-5366-2.
- [97] Christian Walter, Volker Brueser, Antje Quade, and Klaus-Dieter Weltmann. Structural Investigations of Composites Produced from Copper and Polypyrrole with a Dual PVD/PE-CVD Process. *Plasma Processes and Polymers*, 6(12):pp. 803–812, (2009). ISSN 1612-8869. doi:10.1002/ppap.200900056.
- [98] E. Vassallo, A. Cremona, F. Ghezzi, F. Dellera, L. Laguardia, G. Ambrosone, and U. Coscia. Structural and optical properties of amorphous hydrogenated silicon carbonitride films produced by PECVD. *Applied Surface Science*, 252(22):pp. 7993–8000, (2006). ISSN 01694332. doi:10.1016/j.apsusc.2005.10.017.
- [99] G. Beamson and D. Briggs. *High-resolution XPS of Organic Polymers: The Scienta ESCA300 Database*. John Wiley and Sons, (1992).
- [100] B. S. Sahu, A. Kapoor, P. Srivastava, O. P. Agnihotri, and S. M. Shivaprasad. Study of thermally grown and photo-CVD deposited silicon oxide-silicon nitride stack layers. *Semiconductor Science and Technology*, 18(7):pp. 670–675, (2003). doi:10.1088/0268-1242/18/7/312.
- [101] D.-X. Ye, S. Pimanpang, C. Jezewski, F. Tang, J.J. Senkevich, G.-C. Wang, and T.-M. Lu. Low temperature chemical vapor deposition of Co thin films from
-

- $\text{Co}_2(\text{CO})_8$ . *Thin Solid Films*, 485(1-2):pp. 95 – 100, (2005). ISSN 0040-6090. doi:10.1016/j.tsf.2005.03.046.
- [102] M. T. Kim and J. Lee. Characterization of amorphous SiC:H films deposited from hexamethyldisilazane. *Thin Solid Films*, 303(1-2):pp. 173–179, (1997). ISSN 00406090. doi:10.1016/S0040-6090(97)00137-5.
- [103] B. Despax and P. Raynaud. Deposition of "polysiloxane" thin films containing silver particles by an RF asymmetrical discharge. *Plasma Processes and Polymers*, 4(2):pp. 127–134, (2007). ISSN 1612-8869. doi:10.1002/ppap.200600083.
- [104] F. Benitez, E. Martinez, and J. Esteve. Improvement of hardness in plasma polymerized hexamethyldisiloxane coatings by silica-like surface modification. *Thin Solid Films*, 377:pp. 109–114, (2000). ISSN 00406090. doi:10.1016/S0040-6090(00)01393-6.
- [105] Y Gao, J Wei, D.H Zhang, Z.Q Mo, P Hing, and X Shi. Effects of nitrogen fraction on the structure of amorphous silicon-carbon-nitrogen alloys. *Thin Solid Films*, 377-378(0):pp. 562 – 566, (2000). ISSN 0040-6090. doi:10.1016/S0040-6090(00)01292-X.
- [106] YURI M. RUMYANTSEV NADEZHDA I. FAINER and MARINA L. KOSINOVA. Functional nanocrystalline films of silicon carbonitride. *Chemistry for Sustainable Development*, 9:pp. 31 – 36, (2001).
- [107] T. Tharigen, G. Lippold, V. Riede, M. Lorenz, K. J. Koivusaari, D. Lorenz, S. Mosch, P. Grau, R. Hesse, P. Streubel, and R. Szargan. Hard amorphous  $\text{CSi}_x\text{N}_y$  thin films deposited by RF nitrogen plasma assisted pulsed laser ablation of mixed graphite/ $\text{Si}_3\text{N}_4$ -targets. *Thin Solid Films*, 348(1-2):pp. 103–113, (1999). ISSN 00406090. doi:10.1016/S0040-6090(99)00024-3.
- [108] W. F. A. Besling, A. Goossens, B. Meester, and J. Schoonman. Laser-induced chemical vapor deposition of nanostructured silicon carbonitride thin films. *Journal of Applied Physics*, 83(1):pp. 544–553, (1998). ISSN 1089-7550. doi:10.1063/1.366669.
- [109] MR Yang and SK Wu. DC plasma-polymerized hexamethyldisilazane coatings of an equiatomic TiNi shape memory alloy. *SURFACE & COATINGS TECH-*

- 
- NOLOGY*, 127(2-3):pp. 274–281, (2000). ISSN 0257-8972. doi:10.1016/S0257-8972(00)00567-3.
- [110] Bungmek W, Viravathana P, Prangsriaroon S, Chotiwan S, Deutschmann O, and Schulz H. XAS studies on promoted and un-promoted silica supported cobalt catalysts for Fischer-Tropsch synthesis. *2011 International Conference on Environment and Industrial Innovation IPCBEE*, 12:pp. 65–69, (2011).
- [111] Xue-Chao L, Zhi-Zhan C, Er-Wei S, Da-Qian L, and Ke-Jin Z. Room temperature anomalous Hall effect and magneto resistance in (Ga, Co) - undoped ZnO diluted magnetic semiconductor films. *Chin. Phys. B Vol. 20, No. 3*, 20(3):pp. 037501–037507, (2011).
- [112] J. P. Holgado, A. Caballero, J. P. Espinos, J. Morales, V. M. Jimenez, A. Justo, and A. R. Gonzalez-Elipe. Characterisation by X-ray absorption spectroscopy of oxide thin films prepared by ion beam-induced CVD. *Thin Solid Films*, 377:pp. 460–466, (2000). ISSN 0040-6090. doi:10.1016/S0040-6090(00)01436-X.
- [113] Girardon J, Lermontov A, Gengembre L, Chernavskii P, Griboval-Constant A, and Khodakov A. Effect of cobalt precursor and pretreatment conditions on the structure and catalytic performance of cobalt silica-supported Fischer-Tropsch catalysts. *Journal of Catalysis*, 230:pp. 339–352, (2005). ISSN 0021-9517. doi:10.1016/j.jcat.2004.12.014.
- [114] N. Watanabe, J. Morais, S. B. B. Accione, A. Morrone, J. E. Schmidt, and M. C. Martins Alves. Electronic, Structural, and Magnetic Properties of Cobalt Aggregates Embedded in Polypyrrole. *J. Phys. Chem. B*, 108:pp. 4013–4017, (2004). doi:10.1021/jp036940y.
- [115] C. Guyon, A. Barkallah, F. Rousseau, K. Giffard, D. Morvan, and M. Tatoulian. Deposition of cobalt oxide thin films by plasma-enhanced chemical vapour deposition (PECVD) for catalytic applications. *Surface and Coatings Technology*, 206(7):pp. 1673 – 1679, (2011). ISSN 0257-8972. doi:10.1016/j.surfcoat.2011.09.060.
- [116] Shijing Wang, Boping Zhang, Cuihua Zhao, Songjie Li, Meixia Zhang, and Liping Yan. Valence control of cobalt oxide thin films by annealing atmosphere. *Applied Surface Science*, 257(8):pp. 3358 – 3362, (2011). ISSN 0169-4332. doi:10.1016/j.apsusc.2010.11.024.
-

- [117] Arnold F Holleman, Egon Wiberg, and Nils Wiberg. *Lehrbuch der anorganischen Chemie*. de Gruyter, 102., stark umgearb. u. verb. Aufl. edition, (2007).
- [118] H Shim, V Shinde, H Kim, Y Sung, and W Kim. Porous cobalt oxide thin films from low temperature solution phase synthesis for electrochromic electrode. *Thin Solid Films*, 516(23):pp. 8573–8578, (2008). ISSN 00406090. doi:10.1016/j.tsf.2008.05.055.
- [119] Kwon-Il Choi, Hae-Ryong Kim, Kang-Min Kim, Dawei Liu, Guozhong Cao, and Jong-Heun Lee. C<sub>2</sub>H<sub>5</sub>OH sensing characteristics of various Co<sub>3</sub>O<sub>4</sub> nanostructures prepared by solvothermal reaction. *Sensors and Actuators B: Chemical*, 146(1): pp. 183 – 189, (2010). ISSN 0925-4005. doi:10.1016/j.snb.2010.02.050.
- [120] Wei Li, Hyuck Jung, Nguyen Duc Hoa, Dojin Kim, Soon-Ku Hong, and Hyojin Kim. Nanocomposite of cobalt oxide nanocrystals and single-walled carbon nanotubes for a gas sensor application. *Sensors and Actuators B: Chemical*, 150(1): pp. 160 – 166, (2010). ISSN 0925-4005. doi:10.1016/j.snb.2010.07.023.
- [121] An-Hui Lu, E. L. Salabas, and Ferdi Schueth. Magnetic nanoparticles: Synthesis, protection, functionalization, and application. *Angewandte Chemie International Edition*, 46(8):pp. 1222–1244, (2007). ISSN 1521-3773. doi:10.1002/anie.200602866.
- [122] Shubhda Srivastava, Kiran Jain, V N Singh, Sukhvir Singh, N Vijayan, Nita Dilawar, Govind Gupta, and T D Senguttuvan. Faster response of NO<sub>2</sub> sensing in graphene-WO<sub>3</sub> nanocomposites. *Nanotechnology*, 23(20):pp. 205501, (2012). doi:10.1088/0957-4484/23/20/205501.
- [123] S.G. Kandalkar, D.S. Dhawale, Chang-Koo Kim, and C.D. Lokhande. Chemical synthesis of cobalt oxide thin film electrode for supercapacitor application. *Synthetic Metals*, 160(11-12):pp. 1299 – 1302, (2010). ISSN 0379-6779. doi:10.1016/j.synthmet.2010.04.003.
- [124] Griselda A. Eimer, Liliana B. Pierella, Gustavo A. Monti, and Oscar A. Anunziata. Synthesis and Characterization of Al-MCM-41 and Al-MCM-48 Mesoporous Materials. *Catalysis Letters*, 78:pp. 65–75, (2002). ISSN 1011-372X. doi:10.1023/A:1014924332500.

- 
- [125] S. Hazra, A. Ghosh, and D. Chakravorty. Gel to glass conversion in the cobalt silicate system. *Journal of Materials Science Letters*, 13:pp. 589–591, (1994). ISSN 0261-8028. doi:10.1007/BF00592617.
- [126] K. Kato. Transformation of alkoxy-derived SiO<sub>2</sub> gels without catalysts to glasses. *Journal of Materials Science*, 26:pp. 6777–6781, (1991). ISSN 0022-2461. doi:10.1007/BF02402673.
- [127] Shrikant S. Bhoware and A.P. Singh. Characterization and catalytic activity of cobalt containing MCM-41 prepared by direct hydrothermal, grafting and immobilization methods. *Journal of Molecular Catalysis A: Chemical*, 266(1-2):pp. 118 – 130, (2007). ISSN 1381-1169. doi:10.1016/j.molcata.2006.09.031.
- [128] X.H. Xia, J.P. Tu, J. Zhang, X.L. Wang, W.K. Zhang, and H. Huang. Electrochromic properties of porous NiO thin films prepared by a chemical bath deposition. *Solar Energy Materials and Solar Cells*, 92(6):pp. 628 – 633, (2008). ISSN 0927-0248. doi:10.1016/j.solmat.2008.01.009.
- [129] L. Zbroniec, A. Martucci, T. Sasaki, and N. Koshizaki. Optical CO gas sensing using nanostructured NiO and NiO/SiO nanocomposites fabricated by PLD and sol-gel methods. *Applied Physics A: Materials Science and Processing*, 79:pp. 1303–1305, (2004). ISSN 0947-8396. doi:10.1007/s00339-004-2757-0.
- [130] Mao-Sung Wu and Chung-Hsien Yang. Electrochromic properties of intercrossing nickel oxide nanoflakes synthesized by electrochemically anodic deposition. *Applied Physics Letters*, 91(3):pp. 033109, (2007). ISSN 0003-6951. doi:10.1063/1.2759270.
- [131] X.H. Xia, J.P. Tu, J. Zhang, X.H. Huang, X.L. Wang, W.K. Zhang, and H. Huang. Enhanced electrochromics of nanoporous cobalt oxide thin film prepared by a facile chemical bath deposition. *Electrochemistry Communications*, 10(11):pp. 1815 – 1818, (2008). ISSN 1388-2481. doi:10.1016/j.elecom.2008.09.025.
- [132] P.M.S. Monk, R.J. Mortimer, and D.R. Rosseinsky. *Electrochromism: Fundamentals and Applications*. VCH, (1995).
- [133] Y Shimizu and M Shiotsuka. Optoelectrochemical hydrogen-phosphate ion sensor based on electrochromism of spinel-type oxide thin-film electrode. *JAPANESE JOURNAL OF APPLIED PHYSICS PART 1-REGULAR PAPERS SHORT NOTES & REVIEW PAPERS*, 41(10):6243–6246, OCT (2002).
-

- [134] SY PARK, N KIM, UY KIM, SI HONG, and H SASABE. PLASMA POLYMERIZATION OF HEXAMETHYLDISILAZANE. *POLYMER JOURNAL*, 22(3):pp. 242–249, (1990). ISSN 0032-3896.
- [135] T. Peter, M. Wegner, V. Zaporojtchenko, T. Strunskus, S. Bornholdt, H. Kersten, and F. Faupel. Metal/polymer nanocomposite thin films prepared by plasma polymerization and high pressure magnetron sputtering. *Surface and Coatings Technology*, 205, Supplement 2(0):pp. S38 – S41, (2011). ISSN 0257-8972. doi:10.1016/j.surfcoat.2010.12.045.
- [136] Vesna Vodnik, Jasna Vukovic, and Jovan Nedeljkovic. Synthesis and characterization of silver-poly(methylmethacrylate) nanocomposites. *Colloid and Polymer Science*, 287:pp. 847–851, (2009). ISSN 0303-402X. doi:10.1007/s00396-009-2039-7.
- [137] T Hasell, S Yoda, SM Howdle, and PD Brown. Microstructural characterisation of silver/polymer nanocomposites prepared using supercritical carbon dioxide. *Journal of Physics: Conference Series*, 26(1):pp. 276, (2006). doi:10.1088/1742-6596/26/1/066.
- [138] Haoyan Wei and Hergen Eilers. Electrical conductivity of thin-film composites containing silver nanoparticles embedded in a dielectric fluoropolymer matrix. *Thin Solid Films*, 517(2):pp. 575 – 581, (2008). ISSN 0040-6090. doi:10.1016/j.tsf.2008.06.093.
- [139] V.V. Uglov, A.K. Kuleshov, M.V. Astashynskaya, V.M. Anishchik, S.N. Dub, F. Thiery, and Y. Pauleau. Mechanical properties of copper/carbon nanocomposite films formed by microwave plasma assisted deposition techniques from argon-methane and argon-acetylene gas mixtures. *Composites Science and Technology*, 65 (5):pp. 785 – 791, (2005). ISSN 0266-3538. doi:10.1016/j.compscitech.2004.10.011.
- [140] Y Pauleau and F Thiery. Nanostructured copper-carbon composite thin films produced by sputter deposition/microwave plasma-enhanced chemical vapor deposition dual process. *Materials Letters*, 56(6):pp. 1053 – 1058, (2002). ISSN 0167-577X. doi:10.1016/S0167-577X(02)00676-6.
- [141] Y. Pauleau, F. Thiery, J. Pelletier, V. V. Uglov, A. K. Kuleshov, S. N. Dub, and M. P. Samtsov. Structure and mechanical properties of nanostructured metal-carbon films. In Y. G. Gogotsi and Irina V. Uvarova, editors, *Nanostructured*



---

*Materials and Coatings for Biomedical and Sensor Applications*, pages pp. 175–180. (2003). ISBN 978-94-010-0157-1.

- [142] Chun-Chin Chen and Franklin Chau-Nan Hong. Structure and properties of diamond-like carbon nanocomposite films containing copper nanoparticles. *Applied Surface Science*, 242(3-4):pp. 261 – 269, (2005). ISSN 0169-4332. doi:10.1016/j.apsusc.2004.08.036.
- [143] F. Spano, A. Massaro, R. Cingolani, and A. Athanassiou. Optical enhancement by means of concentration tuning of gold precursors in polymer nanocomposite materials. *Microelectronic Engineering*, 88(8):pp. 2763 – 2766, (2011). ISSN 0167-9317. doi:10.1016/j.mee.2011.01.044.
- [144] Andrei Choukourov, Ivan Gordeev, Dmitry Arzhakov, Anna Artemenko, Ondrej Kylian, Jaroslav Kousal, Oleksandr Polonskyi, Josef Pesicka, Danka Slavinska, and Hynek Biederman. Nanocomposite gold/poly(ethylene oxide)-like plasma polymers prepared by plasma-assisted vacuum evaporation and magnetron sputtering. *Surface and Coatings Technology*, 205(8-9):pp. 2830 – 2837, (2011). ISSN 0257-8972. doi:10.1016/j.surfcoat.2010.10.055.
- [145] C. de Julian Fernandez, M.G. Manera, J. Spadavecchia, G. Maggioni, A. Quaranta, G. Mattei, M. Bazzan, E. Cattaruzza, M. Bonafini, E. Negro, A. Vomiero, S. Carturan, C. Scian, G. Della Mea, R. Rella, L. Vasanelli, and P. Mazzoldi. Study of the gas optical sensing properties of Au-polyimide nanocomposite films prepared by ion implantation. *Sensors and Actuators B: Chemical*, 111-112(0):pp. 225 – 229, (2005). ISSN 0925-4005. doi:10.1016/j.snb.2005.07.042.
- [146] F. Vitale, L. Mirengi, E. Piscopiello, G. Pellegrini, E. Trave, G. Mattei, I. Fratoddi, M.V. Russo, L. Tapfer, and P. Mazzoldi. Gold nanoclusters-organometallic polymer nanocomposites: Synthesis and characterization. *Materials Science and Engineering: C*, 27(5-8):pp. 1300 – 1304, (2007). ISSN 0928-4931. doi:10.1016/j.msec.2006.06.041.
- [147] Jamileh Taghavimoghaddam, Gregory P. Knowles, and Alan L. Chaffee. Preparation and characterization of mesoporous silica supported cobalt oxide as a catalyst for the oxidation of cyclohexanol. *Journal of Molecular Catalysis A: Chemical*, 358(0):pp. 79 – 88, (2012). ISSN 1381-1169. doi:10.1016/j.molcata.2012.02.014.

- [148] Abolanle S. Adekunle, Jeseelan Pillay, and Kenneth I. Ozoemena. Probing the electrochemical behaviour of SWCNT-cobalt nanoparticles and their electrocatalytic activities towards the detection of nitrite at acidic and physiological pH conditions. *Electrochimica Acta*, 55(14):pp. 4319 – 4327, (2010). ISSN 0013-4686. doi:10.1016/j.electacta.2009.02.102.
- [149] Chen-Bin Wang, Chih-Wei Tang, Hsin-Chi Tsai, and Shu-Hua Chien. Characterization and catalytic oxidation of carbon monoxide over supported cobalt catalysts. *Catalysis Letters*, 107:pp. 223–230, (2006). ISSN 1011-372X. doi:10.1007/s10562-005-0002-x.
- [150] Feng Jiao and Heinz Frei. Nanostructured cobalt oxide clusters in mesoporous silica as efficient oxygen-evolving catalysts. *Angewandte Chemie International Edition*, 48(10):pp. 1841–1844, (2009). ISSN 1521-3773. doi:10.1002/anie.200805534.
- [151] I. Hotovy, J. Huran, P. Siciliano, S. Capone, L. Spiess, and V. Rehacek. The influences of preparation parameters on NiO thin film properties for gas-sensing application. *Sensors and Actuators B: Chemical*, 78(1-3):pp. 126 – 132, (2001). ISSN 0925-4005. doi:10.1016/S0925-4005(01)00802-4.
- [152] Agnes Szegedi, Margarita Popova, Vesselina Mavrodinova, and Christo Minchev. Cobalt-containing mesoporous silicas—Preparation, characterization and catalytic activity in toluene hydrogenation. *Applied Catalysis A: General*, 338(1–2):pp. 44 – 51, (2008). ISSN 0926-860X. doi:10.1016/j.apcata.2007.12.017.
- [153] Masanori Ando, Tetsuhiko Kobayashi, Sumio Iijima, and Masatake Haruta. Optical recognition of CO and H<sub>2</sub> by use of gas-sensitive Au-Co<sub>3</sub>O<sub>4</sub> composite films. *J. Mater. Chem.*, 7:pp. 1779–1783, (1997). doi:10.1039/A700125H.
- [154] Masanori Ando, Tetsuhiko Kobayashi, and Masatake Haruta. Combined effects of small gold particles on the optical gas sensing by transition metal oxide films. *Catalysis Today*, 36(1):pp. 135 – 141, (1997). ISSN 0920-5861. doi:10.1016/S0920-5861(96)00206-4.

# Acknowledgments

I express my deep gratitude to my PhD supervisor **Prof. Dr. Franz Faupel**, Head of the Chair for Multicomponent Materials, CAU Kiel for accepting me as his PhD student. I am immensely thankful to him for the fruitful scientific discussions showing me the right direction, his constant guidance, and motivation. I greatly admire his sympathetic nature in understanding my problems and supporting me.

I express my sincere thanks to **Dr. Volker Brueser**, Head of Plasma Process Technology (Materials Division), Leibniz Institute for Plasma Science and Technology (INP) Greifswald for providing me the opportunity to perform research in his group. I would like to thank him for his kind heartedness, for the many scientific discussions and support throughout my PhD. The work done in this thesis was carried out at INP under the main supervision of Dr. Volker Brueser.

I am very thankful to **Dr. Thomas Strunskus**, CAU Kiel for his constant advice and helpful discussions throughout my research. I greatly appreciate his patience to answer my questions. I profusely thank **Dr. Vladimir Zaporajtchenko**, CAU Kiel for the various scientific discussions we had and the encouragement he gave me.

I am grateful to **Prof. Dr. Klaus-Dieter Weltmann**, Director of INP, Greifswald for providing me the opportunity to work in the institute and also for the discussions during the PhD seminars.

I would like to particularly thank the synchrotron radiation center **BESSY** in Berlin for providing the opportunity to perform XAS experiments. Special thanks to **Dr. Nicolae L. Aldea**, National Institute for Research and Development for Isotopic and Molecular Technologies, Cluj-Napoca, Romania for accompanying and helping me at BESSY. I am grateful to him for painstakingly teaching me the XAS theory and analysis in depth.

I am grateful for the financial support from Bundesministerium fuer Bildung und Forschung (**BMBF**) for our project **03F0481C** ('CaliPSo') at the INP.

I would like to profusely thank **Dr. Rabea Schlueter**, Institute of Microbiology, University of Greifswald who was very kind to perform several TEM experiments. I appreciate

her great help for my PhD thesis. A big thanks to **Dr. Simone Venz**, University of Greifswald for introducing me to Dr. Schlueter.

I would like to thank **Dr. Harm Wulff**, Institute for Physics, University of Greifswald for the XRD characterization of my samples. I express my sincere thanks to **Dr. Angela Kruth**, INP for the help and discussion on optoelectrochemical measurements. I would like to thank **Dr. Antje Quade**, INP for the XPS measurements. A special thanks to **Dr. Abhijit Majumdar**, University of Greifswald for introducing me to Dr. Brueser. Thanks to **Dipl.- Phys. Christian Walter**, INP for the EDX/SEM measurements and the initial help at BESSY. Thanks to **Dr. Jan Schaefer**, INP for the EDX/SEM measurements.

I would like to thank **Dr. Ruben Wiese**, **Dipl.- Phys. Georg Wiese**, INP for the active thermal probe experiments. Special thanks to **Ms. Kirsten Anklam**, INP not just for the optoelectrochemical experiments, but also for motivating me throughout. I wish to thank **Dipl.- Phys. Steffen Müller** and **Dipl.- Phys. Stephan Hamann**, INP for the help with  $\text{\LaTeX}$  and also for the various discussions we had. Thanks to **Dr. Natalie Savastenko**, INP for teaching me how to operate the AFM. Thanks to our technician **Mr. Karl-Heinz Schmidt**, INP for helping me with the reactor problems. I would like to thank **Ms. Cornelia Krcka**, INP for the helpful comments on grammar and English in my thesis.

My special thanks goes to **Prof. Dr. Uwe Voelker**, Director of Functional Genomics Lab, University of Greifswald for giving me my first job in Germany and letting me to go into research of my interest and make my PhD possible.

My heartfelt thanks to my teacher **Dr. Petra Kock** for teaching me German which helped me in my everyday life. Many thanks to her husband **Dr. Holger Kock** for his comments on my scientific English. I wish to thank them for the various weekly meetings we had and for being a big moral support to me.

I would like to thank all my colleagues and friends in Greifswald and Kiel who have helped me in completing my PhD thesis. Special thanks to my friend **Selvi** who supported me.

Thanks to **my parents** and **my brother** for their unconditional love.

Thanks to my husband, **Kumar**, for being with me through thick and thin.

# Curriculum Vitae

## Personal details

Name: Karthika Lakshmi Kolipaka  
Permanent address: Plot No: 21, Prashanth Hills,  
Khajaguda Cross Road, Old Bombay  
High Way, Hyderabad, India - 500008  
Date of birth: 13 May, 1984  
Marital status: Married  
Nationality: India

## Education

1998 - 1999: Secondary School Certificate, Hyderabad, India  
1999 - 2001: Intermediate, Hyderabad, India  
2001 - 2005: Bachelor of Engineering,  
(Electronics and Communication Engineering),  
Osmania University, Hyderabad, India  
2005 - 2007: Master of Technology,  
(Integrated Circuit Technology),  
University of Hyderabad, Hyderabad, India  
2009 - 2012: PhD student in Plasma Process Technology  
department (Materials Division)  
at INP, Greifswald, Germany

## Work experience

July 2008 - Dec 2008: Programmer, Functional Genomics Lab,  
University of Greifswald, Germany  
Jan 2009 - Aug 2012: PhD Student, INP, Greifswald, Germany

### List of publications

1. **K. L. Kolipaka**, V. Brueser, R. Schlueter, A. Quade, J. Schaefer, H. Wulff, T. Strunskus, F. Faupel, *Simple method of hybrid PVD/PECVD to prepare well-dispersed cobalt - plasma polymerized hexamethyldisilazane nanocomposites*, In press, Accepted, Surface and Coatings Technology (2012), doi: 10.1016/j.surfcoat.2012.07.073 (Full paper).
2. N. Aldea, **K. L. Kolipaka**, V. Rednic, F. Matei, *XAS a new computer package program for X-ray absorption spectroscopy data analysis*, Published, Journal of Optoelectronics and Advanced Materials, Vol. 13, No. 11-12, November - December 2011, p. 1581 - 1585 (Full paper).
3. **K. L. Kolipaka**, N. Aldea, V. Brueser, V. Rednic, A. Quade, J. Schaefer, H. Wulff, Z. Zhang, T. Strunskus, F. Faupel, *Structural investigations of  $Co_3O_4$  - amorphous-Si-O:C nanocomposites using XRD, XAS, and XPS methods*, Ready to submit (Full paper).
4. **K. L. Kolipaka**, A. Kruth, V. Brueser, C. Walter, H. Wulff, T. Strunskus, F. Faupel,  *$Co_3O_4$  - amorphous-Si-O:C nanocomposite thin films as opto electrochemical phosphate ion sensors*, In preparation (Full paper).
5. **K. L. Kolipaka**, V. Brueser, A. Quade, H. Wulff, and F. Faupel, *Deposition and analysis of Co - a: SiCN nanocomposites*, NANO2010 Abstract booklet (Abstract).
6. **Karthika Lakshmi Kolipaka**, Volker Brueser, Antje Quade, Harm Wulff, and Franz Faupel, *Hybrid PVD/ PECVD fabrication and structural investigations of Cobalt-amorphous SiCNH nanocomposites*, DPG Spring Meeting Kiel, 2011 Abstract booklet (Abstract).

### Oral and poster presentations

1. NANO 2010 International Conference, Rome, Italy (9/13/2010 - 9/17/2010), *Deposition and analysis of Co- a: SiCN nanocomposites*, **K. L. Kolipaka**, V. Brueser, A. Quade, H. Wulff, and F. Faupel (Oral presentation).

2. ISPC20 International Symposium on Plasma Chemistry, Philadelphia, USA (7/24/2011 - 7/29/2011), *Structural and optical characterization of spinel type cobalt oxide nanoparticles embedded in amorphous silicon oxide matrix prepared by a hybrid PVD/ PECVD process*, **Karthika Lakshmi Kolipaka**, Volker Brueser, Antje Quade, Jan Schaefer, Harm Wulff, Franz Faupel (Oral presentation).
3. PIM2011 Processes in isotopes and molecules, international conference, Cluj-Napoca, Romania, (29/9/2011 - 1/10/2011), *An XAS study on Co - plasma polymerized HMDSN and  $Co_3O_4$ -SiOx nanocomposites*, **Karthika Lakshmi Kolipaka**, Volker Brueser, Vasile Rednic, Nicolae. L. Aldea (Oral presentation).
4. DPG Spring Meeting, Kiel, Germany (28/3/2011 - 31/3/2011). *Hybrid PVD/PECVD fabrication and structural investigations of Cobalt - amorphous SiCNH nanocomposites*, **Karthika Lakshmi Kolipaka**, Volker Brueser, Antje Quade, Harm Wulff, and Franz Faupel (Poster presentation).
5. ISPC20 International Symposium on Plasma Chemistry, Philadelphia, USA (7/24/2011 - 7/29/2011), *Plasma Engineering of Nanoparticulate Photocatalytic Systems for Water Splitting: Preparation and Surface Sensitization of TiO<sub>2</sub> Photocatalysts*, Angela Kruth, **Karthika Lakshmi Kolipaka**, Antje Quade, Uwe Lindemann, Urte Kellner, Torsten Beweries, Sven Hansen, Volker Brueser and Klaus-Dieter Weltmann (Poster presentation).

Greifswald 27.08.2012